MEASURING AND MODELING MEAN FLOW, TURBULENCE, AND HYDRAULIC RESIDENCE TIME IN SHALLOW SURFACE WATER SYSTEMS OCCUPIED BY SUBMERGED AND EMERGENT AQUATIC VEGETATION

A Dissertation

Presented to the Faculty of the Graduate School

of Cornell University

in Partial Fulfillment of the Requirements for the Degree of

Doctor of Philosophy

by

Alexandra King

May 2011

MEASURING AND MODELING MEAN FLOW, TURBULENCE, AND HYDRAULIC RESIDENCE TIME IN SHALLOW SURFACE WATER SYSTEMS OCCUPIED BY SUBMERGED AND EMERGENT AQUATIC VEGETATION

Alexandra King, Ph.D.

Cornell University 2011

Predicting mixing and transport of pollutants and nutrients in natural surface waters requires consideration of many different scales, from the smallest scales of turbulence dissipated in the wakes of aquatic vegetation to the scales of transit through an entire aquatic system such as a lake, river, or wetland. Here we address two topics pertaining to the general problem of mixing and transport: the first is modeling of vertical mixing by turbulence in systems that may be occupied by aquatic plants, and the second is tracer-based measurement of hydraulic residence time (HRT), a bulk quantity defined as the time water remains in an aquatic system.

We develop a numerical model that predicts vertical turbulent eddy viscosity in flow through aquatic vegetation, employing a k–ε approach. The model is unique in its treatment of turbulent dissipation in plant wakes, outperforming existing models in predicting experimental results from emergent and submerged rigid cylinders (model vegetation) in two laboratory studies. The model is applicable to real vegetation, but validation in real vegetation is pending as ongoing experiments are completed. The model can be readily incorporated into larger two- or three-dimensional hydrodynamic solvers that predict momentum and scalar transport in natural systems.

Focusing on the system scale, we develop new methods for measuring mean HRT. A standard technique is the passive tracer pulse release, in which a known mass of neu-

trally buoyant tracer is released all at once into a system, and its flux out of the system is monitored. The first temporal moment of tracer flux equals the mean HRT. We propose new methods for extrapolating flux in a way that is consistent with conservation of mass, correcting for photolytic decay of fluorescent water tracing dyes (commonly used tracers), and estimating uncertainty in mean HRT measurements. We review the literature on sorption of Rhodamine WT (a popular tracer), exposing knowledge gaps that must be filled before sorption can be predicted in field studies. We evaluate the advantage of carefully measuring velocity profiles across an outlet (vs. point measurement) and suggest techniques for measuring concentration over long times in particle-laden systems.

BIOGRAPHICAL SKETCH

Alexandra (Allie) King was born in 1979 in Seattle, Washington. She moved with her parents to Princeton, New Jersey in 1983 and to Boca Raton, Florida in 1989. She attended Atlantic Community High School in nearby Delray Beach, graduating from the International Baccalaureate program there in 1998. She then attended Rice University in Houston, Texas, and in 2002 received a Bachelor of Science degree in Civil Engineering from Rice with a concentration in Environmental Engineering. In the summer of 2001, between her Junior and Senior years, she worked for Professor Edwin (Todd) Cowen at Cornell University in Ithaca, New York as an intern, conducting fieldwork in coastal embayments along the southern and eastern shores of Lake Ontario. This experience peaked her interest in environmental fluid mechanics as well as her interest in living in Ithaca, inspiring her to apply to graduate school at Cornell. With Professor Cowen as her advisor, she earned a Masters of Science degree from Cornell in 2006 and continued to work towards completion of this doctoral dissertation.

This dissertation is dedicated to my parents, Benjamin and Celeste King, who always encouraged me to pursue my interests, whether my interest of the moment was science, art, or teaching the dog to do circus tricks, and to Eric Ryan, my husband, who makes everything in life seem better, even thesis writing.

ACKNOWLEDGEMENTS

Thanks to Francisco Zarama and Rafael Tinoco for conducting the laboratory experiments discussed in this work. Thanks also to a long list of participants in the Lake Ontario Biocomplexity Project including Francisco Rueda, Peter Rusello, Evan Variano, Aaron Blake, Kristi Kull, Rebecca Doyle-Morin, Kristin Arend, Virginia Pasour, Gail Steinhart and many others, for help in the field, for many conversations about the topics in this thesis, and for great company through the years.

Special thanks to Rafael Tinoco and Francisco Rueda for long insightful conversations about residence time and flow through aquatic vegetation, to Peter Rusello for tremendous and outstanding help in the field, and to William Philpot for generous advice regarding light transmission through water.

Finally, thanks to my dissertation committee: to Lance Collins, whose thoughtful comments in the early stages of my studies led to fruitful new topics of research, to Nelson Hairston, for being willing to embark on our experiment of collaboration between physical and biological limnologists, and for extensive advice pertaining to the dissertation itself, and to Edwin (Todd) Cowen, my advisor, for support, insight, and patience as my path to a Ph.D. led down many unexpected roads.

This material is based upon work supported by the National Science Foundation under grant CBET-0083625. Initial support for the author's graduate career was provided by the National Science Foundation Graduate Research Fellowship Program. Any opinions, findings, and conclusions or recommendations expressed in this material are those of the authors and do not necessarily reflect the views of the National Science Foundation.

TABLE OF CONTENTS

CHAPTER 1

INTRODUCTION

The motivation of this work can be traced to the Lake Ontario Biocomplexity Project[1], a multidisciplinary project involving nine principal investigators at three institutions[2] investigating the interaction of physics, chemistry, ecology, and society in the context of six freshwater embayments along the southern and eastern coasts of Lake Ontario. The organizing hypothesis of the project was that

> "the average time water takes to move through an aquatic system is a key variable defining the extent that ecosystems are self-organized or dominated by outside influences."

A critical component of the Biocomplexity project was characterization of this average transit time in the six embayments, and the motivation for this dissertation was the process of characterizing transit time in a single embayment: Sterling Pond (SP), a natural basin having a 0.38 km^2 surface area and an average depth of 1.5 m, draining a 210 km^2 watershed, largely through Sterling Creek (SC), a stream of 40 m width, into Lake Ontario (LO) through a long and narrow (17 m wide, 2.5 m deep 140 m long) manmade channel. From late spring through early fall, SP is populated by diverse species of aquatic vegetation.

In order to characterize the transport time scales in SP, we conducted two passive tracer release studies, releasing a fluorescent dye at the mouth of SC and continuously monitoring its flux out of SP into LO. The first moment of the appropriately normalized

[1] Biocomplexity: Physical, Biological, and Human Interactions Shaping the Ecosystems of Freshwater Bays and Lagoons, NSF award number OCE-0083625, 2001-2005

[2] Cornell University, Syracuse University, and SUNY College of Environmental Science & Forestry

dye flux curve is equal to the mean hydraulic residence time, i.e., the average amount of time water remains in the system, for the water parcel containing the dye (Monsen et al., 2002). These two dye studies were the subject of King (2006). We sought to conduct the studies in the context of different dominant physical forcing conditions to capture somewhat the variability of the residence time for water entering SP from its watershed. The first study, lasting less than one day, was conducted in May of 2002 and took place after a spring snowmelt event resulting in high watershed flow. At this time seiching in LO was relatively mild, and aquatic vegetation was sparse and mostly submerged. The dominant species was *Ceratophyllum demersum*. The second tracer release study, lasting over two weeks, was conducted in September of 2003 during a period of low-to-moderate watershed flow and strong barotropic forcing from LO due to seiches having time scales from 1.7 to 5 hrs (Hamblin, 1982). During this study, aquatic vegetation was quite dense and reached the water surface throughout SP; *Myriophyllum spicatum* (Eurasian watermilfoil, an invasive species prevalent across North America) and *Nitellopsis obtusa* (an invasive native to Japan and rare in North American lakes but surprisingly successful in SP) competed for dominance.

The dye study results were intended for calibration of a three-dimensional (3D) hydrodynamic model for SP that could be used to explore the effect of different physical forcing regimes (seiching of LO, upwelling in LO, strong watershed flows) on the transport timescales of SP, in a similar manner to Rueda and Cowen (2005b). Several existing 3D solvers for the shallow water equations, incorporating the hydrostatic pressure assumption and Boussinesq approximation for buoyancy would be appropriate for modeling transport of nutrients, pollutants, or fluorescent water tracing dye in SP. Examples include the Princeton Ocean Model (Blumberg and Mellor, 1987; Mellor, 1996), the Regional Ocean Mixing Model (Warner et al., 2005) and Si3D (Rueda and Schladow, 2002).

These types of models typically parameterize vertical turbulent diffusivity using an eddy viscosity and one or more submodels of varying complexity to solve for eddy viscosity (e.g., constant eddy viscosity, mixing length, two-equation models such as k–ε or Mellor-Yamada, Reynolds stress).

Modeling Flow Through Aquatic Vegetaiton (Chapter 2): Our first step in the numerical modeling program was to incorporate a turbulence submodel that was appropriate for flow through aquatic vegetation. Reasoning that mixing length could be difficult to predict in flow through real vegetation, which can exhibit multiple scales of vertical shear, we settled on a second order model, beginning with the k–ε approach, so that turbulent length scales could adjust naturally to vertical shear resulting from gradients in canopy drag. Testing existing $k-\varepsilon$ models for flow through aquatic vegetation against laboratory data from beds of live Eurasian watermilfoil (Tinoco, 2008), it became clear that they were not sufficient to capture the dominant mixing processes in the vegetation found in SP. While existing second order models for flow through vegetation accounted for production of turbulence both by vertical shear (at the scale of vertical variation in the plant frontal area profile) and by work of the mean flow against drag on plant stems (at the scale of the plant stems), none allowed proper scaling of dissipation with both plant stems and the vertical gradients. This resulted in poor predictions of turbulent kinetic energy and dissipation in the laboratory milfoil canopy. In Chapter 2, we present a new $k-\varepsilon$ model that includes production and dissipation at both of these scales. The model is calibrated and validated against laboratory measurements in beds of emergent and submerged cylinders and outperforms existing models. It can be easily incorporated into any larger model that employs a vertical eddy viscosity. It transitions naturally between the regimes of no plants, submerged plants, and plants that reach the water surface, and is in

theory appropriate for (though as yet untested) and in practice ready for application to real vegetation having an arbitrary frontal area profile.

Measuring Mean Hydraulic Residence Time (Chapter 3): Analyzing the dye study results and estimating the mean hydraulic residence time from the two dye studies also proved more difficult than we expected. 3D numerical simulations of the 2002 dye study, using Si3D without the plant model (reasonable because plants were sparse in 2002), led us to suspect that we had over-estimated the flow rate out of the channel connecting SP to LO. This led to an investigation of the horizontal variation of the velocity across the channel. Concern about photolytic decay of the dye used in the tracer release studies (rhodamine WT) led us to develop a method for converting a dye flux curve for a photolytic tracer into a dye flux curve for a hypothetical conservative tracer that can be used in hydraulic residence time measurements and for benchmarking of numerical models. Difficulty extrapolating the dye flux curve to account for missing dye mass led us to develop a new method of extrapolating dye flux curves that is robust in the case of highly oscillatory reversing flow. Finally, efforts to estimate uncertainty in our estimates of hydraulic residence time led us to apply an approach that is appropriate for propagating uncertainty that is correlated over finite but nonzero timescales and for propagating uncertainty through the implicit equations required for our photolysis correction. We also propose an approach for estimating uncertainty due to possible sorption of dye onto sediment, plants, and detritus. These new methods for analyzing passive tracer release data are presented and evaluated in Chapter 3.

The project of modeling residence time under different forcing scenarios in SP is still underway. The vertical turbulent mixing model developed in Chapter 2 can be incorporated into a larger hydrodynamic solver that can be calibrated against the results of

the dye studies and analysis described in Chapter 3. But beyond the motivating problem of characterizing residence time scales of SP, the new model for flow through aquatic vegetation and the new methods for measurement of mean hydraulic residence time are applicable in a wide variety of natural surface water systems including as lakes, rivers, wetlands, and estuaries.

CHAPTER 2

A K–ε MODEL FOR FLOW THROUGH AQUATIC VEGETATION

2.1 Introduction

Aquatic vegetation influences flow and transport in wetlands, rivers, lakes, estuaries, and the coastal ocean. Flow through aquatic vegetation, often called 'canopy flow', is characterized by several distinct length scales. Scales that are easily identified include the water depth, H, and a range of stem diameters, d. A less obvious length scale is the inverse of the plant frontal area per unit volume, a^{-1}. If there are N plants in volume V, where V includes both fluid and plants, and plant i has area A_i perpendicular to the mean flow, then the frontal area per unit volume, or frontal area density, is defined as

$$a \equiv \frac{1}{V} \sum_{i=1}^{N} A_i. \tag{2.1}$$

An illustration of a is provided in figure 2.1 for rigid cylinders (often used to model aquatic vegetation in a laboratory setting). For many real plants, a varies strongly in the vertical direction. Thus, another important set of length scales in canopy flow is the range of scales over which $a(z)$ varies, where z is the elevation above the bed.

Investigations into flow through aquatic vegetation have tended to focus either on dense emergent vegetation, for which mean vertical shear is negligible and turbulence in plant wakes is the primary mechanism of mixing (e.g., Tanino and Nepf, 2008b), or on deeply submerged dense vegetation, in which the drag discontinuity at the top of the plant canopy leads to the formation of a mixing layer, producing turbulence at the scale of the plant height that is destroyed in plant wakes (e.g., Ghisalberti and Nepf, 2004). This division into emergent and submerged cases can work nicely for plants that

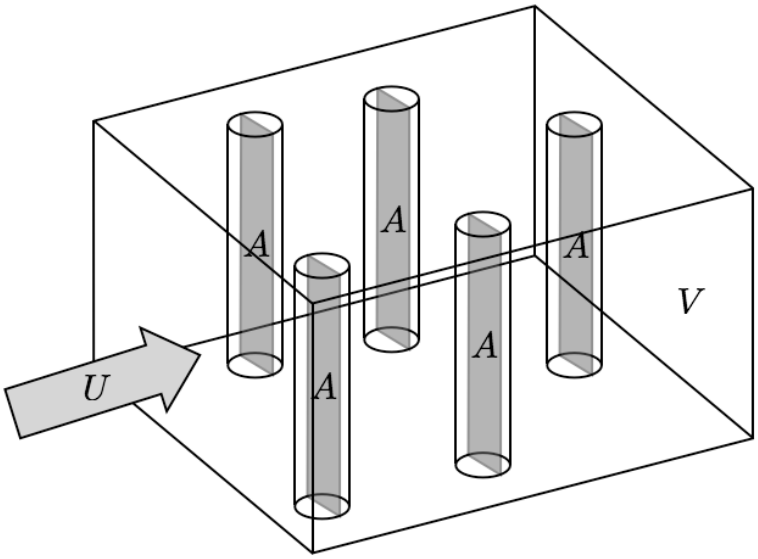

Figure 2.1: Illustration of $N = 5$ cylinders within a volume, V, showing the cylinder frontal areas, A, which are in the plane perpendicular to the mean velocity, U. In this case, $a = NA/V$.

resemble tall cylinders, such as reeds or sea grasses, but many leafy emergent plants have sufficiently non-uniform frontal area profiles that turbulence generated by vertical shear can be significant as well as wake turbulence.

The motivation for this work was our effort to predict velocities, turbulent diffusivities, and dispersion in Eurasian water milfoil (*Myriophyllum spicatum*), a freshwater plant that is native to Eurasia and Africa but rapidly spreading across North America as an invasive species. Milfoil is characterized by a highly non-uniform frontal area density profile, as shown in figure 2.2. Working with an emergent canopy of milfoil in a laboratory flume, Tinoco (2008) measured vertical profiles of velocity, turbulent kinetic energy (TKE), Reynolds stress, and dissipation using particle image velocimetry techniques.

Using the milfoil data, Tinoco (2008) tested a simple model developed by Lightbody and Nepf (2006), who were able to predict velocity profiles and longitudinal dispersion

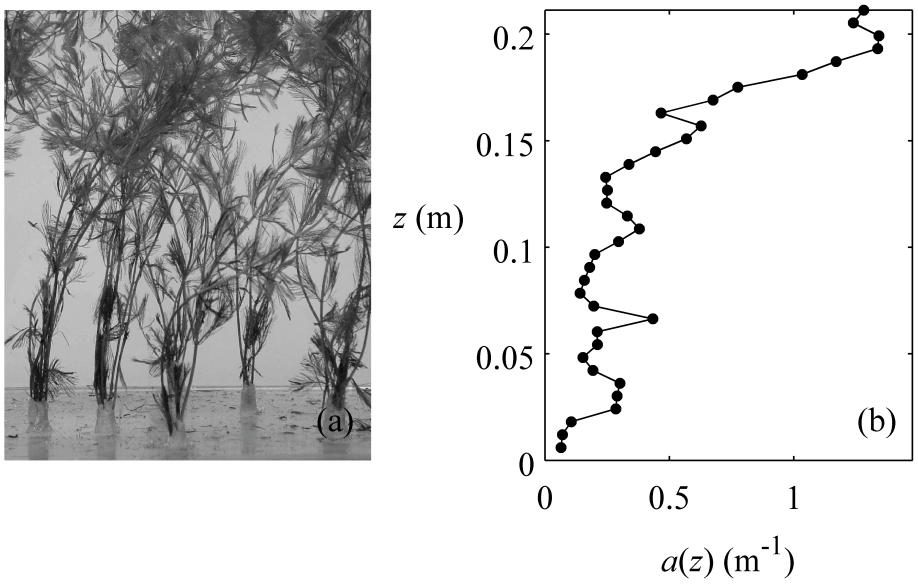

Figure 2.2: (*a*) Photograph of Eurasian water milfoil (*Myriophyllum spicatum*) in a laboratory flume, and (*b*) vertical profile of frontal area density, $a(z)$, for the milfoil canopy at a stem density of $n = 50$ m^{-2}, where z is elevation above the bed.

in a *Spartina alterniflora* wetland from a balance between drag and pressure gradients alone, i.e., neglecting vertical shear. In the case of milfoil, however, vertical shear was too significant to ignore, and the Lightbody and Nepf (2006) model performed poorly. We concluded that a model that predicts velocity profiles in a wide variety of real vegetation must include a parameterization for vertical shear. Given the scales of natural aquatic systems, a Reynolds-averaged Navier–Stokes (RANS) approach is appropriate, but because in real vegetation, $a = a(z)$, and thus vertical shear may vary over multiple, ill-defined length scales, a mixing length type model would be limited in applicability. Hence, a two-equation model such as k–ε, in which the turbulent length scale can adapt naturally to $a(z)$, is our simplest choice.

We originally hoped that the k–ε model of López and García (2001) could be adapted for use in real vegetation. López and García (2001) modified the standard k–ε model for

application in aquatic plant canopies by adding an extra production term in the TKE and dissipation equations to account for the extra TKE produced in the plant wakes. To accommodate the moderate Reynolds numbers that milfoil experiences in nature, we modified the López and García (2001) model to account separately for viscous and pressure drag as described in King et al. (2009), and while with enough tuning, we were able to obtain decent fits to the mean velocity profiles measured in the laboratory milfoil canopies, we were not able to predict TKE or dissipation with an acceptable level of accuracy. Measurements revealed that dissipation scaled to a large degree with the effective stem diameter of the plants, defined as $d(z) = n/a(z)$, where n is the number of stems per unit horizontal area; and dissipation scaled to a lesser degree with the multiple scales of the mean shear (R. O. Tinoco, personal communication). This led us to notice that the López and García (2001) model and other existing k–ε models for flow through plant canopies (aquatic or terrestrial) do not anywhere incorporate stem diameter. Furthermore, we noticed that nearly all experiments used to calibrate such models for use in aquatic canopies have been conducted in beds of rigid cylinders having diameter $d = 6.4$ mm ($1/4$ in). In the well-studied case of emergent rigid cylinders in a laboratory setting, where turbulence is known to scale with d, these existing k–ε models break down entirely.

To enable prediction of flow and transport in vegetated lakes, rivers, wetlands, and coastal areas, there is clearly a need for a two-equation model that incorporates the wake scale as well as the scale of the vertical shear. Such a model would be appropriate in vegetation with highly non-uniform $a(z)$ as well as reed-like vegetation, and would transition smoothly between emergent and submerged vegetation, such as in tidal flows. We develop such a model in the following sections.

After a discussion of the governing equations in Section 2.2 and an overview of the basic physical processes present in flow through aquatic vegetation in Section 2.3, we in-

troduce the new k–ε model in Section 2.4. While the model was developed with real plant canopies in mind, it is here calibrated against new laboratory data from flow through two arrays of rigid cylinders, one with cylinders of diameter $d = 3.2$ mm, and the other with cylinders of diameter $d = 25.4$ mm; each array is subjected to both emergent and submerged conditions. The model is validated against existing laboratory data from beds of submerged rigid cylinders having diameter $d = 6.4$ mm. The experiments are discussed in Section 2.5, the calibration in Section 2.6, and the validation in Section 2.7. Model performance is compared to the performance of two existing k–ε models for flow through vegetation: those of López and García (2001) and of Katul et al. (2004). The new model outperforms both, not only in emergent cylinders where the other models break down entirely but also in submerged cylinders where the inclusion of stem-scale turbulence leads to better predictions of velocity profiles and dramatically better predictions of TKE.

The success of the new model provides insight into the physics of flow through aquatic vegetation, in particular the pathways of TKE generation and transfer between different wavenumbers. At this point, the model operates under the assumption of fully developed steady flow, but it would be simple to add terms for unsteadiness and advection. It is typical for 1D vertical mixing models, such as this one, to be incorporated into larger three-dimensional hydrodynamic models, such as Si3D (Smith, 2006; Rueda and Schladow, 2002), POM (Blumberg and Mellor, 1987), or ROMS (Song and Haidvogel, 1994) and into coastal wave models such as COBRAS (Lin and Liu, 1998). Other possible applications extend to air flow through terrestrial canopies and urban landscapes, hydraulic flow around offshore structures, and industrial flows.

2.2 Governing Equations

If the system of interest is a wetland, lake, river, estuary, or the coastal ocean (or in the case of air flow, a forest, field, or city), it is not computationally practical to resolve the flow field at the scale of individual plant stems. Hence, the approach of RANS modelers since Wilson and Shaw (1977) has been to horizontally average the governing equations over a scale large enough to smooth over heterogeneity due to the plant canopy structure. Raupach and Shaw (1982), building on the work of Wilson and Shaw (1977), formalized two alternative spatial averaging procedures that are now widely known as schemes I and II. These two schemes were refined by Finnigan (1985) and by Raupach et al. (1986), who replaced the original horizontal average with a more general volume average. In scheme I, the equations are averaged over thin horizontal slabs large enough to smooth over heterogeneity due to turbulence as well as canopy structure but thin enough to preserve vertical gradients. In scheme II, a time average is employed to smooth over variations due to turbulence so that the spatial averaging volume need be extensive enough only to smooth over heterogeneity due to the canopy. Wilson and Shaw (1977) asserted that schemes I and II were essentially the same, but Raupach and Shaw (1982) later showed that they lead to different sets of averaged equations. Because it is rarely possible in laboratory or field settings to average over a large enough horizontal slab to smooth over heterogeneity due to turbulence, the equations developed under scheme II are more appropriate for comparison with experimental measurements.

The governing equations we review here are based on scheme II, in which a scalar field ψ (such as the streamwise velocity component, pressure, etc.) is decomposed into a time average, indicated by an overbar, and a fluctation from that time average, indicated

by a single prime:

$$\psi = \overline{\psi} + \psi'. \tag{2.2}$$

The time average is further decomposed into a spatial average, indicated by angle brackets, and the deviation from that spatial average, indicated by double primes:

$$\overline{\psi} = \langle \overline{\psi} \rangle + \overline{\psi}''. \tag{2.3}$$

The angle brackets indicate averaging over the fluid domain (i.e., excluding plant parts) within a thin horizontal slab large enough to smooth over heterogeneity due to the plant canopy but thin enough to preserve vertical gradients. For simplicity, let us consider steady, uniform, open-channel flow where x is the downstream coordinate and z is the elevation above the bed. Let u and w represent the instantaneous downstream and vertical velocity components, respectively.

2.2.1 Momentum Equation

Averaging the x-momentum equation for steady, uniform, open-channel flow under scheme II results in

$$0 = gS + \frac{\partial \tau_{xz}}{\partial z} - f \tag{2.4}$$

where g is the acceleration of gravity, S is the bed slope (equal to the surface slope), f is the drag force per unit fluid mass, and the mean shear stress, τ_{xz}, defined by

$$\tau_{xz} \equiv \nu \frac{\partial \langle \overline{u} \rangle}{\partial z} - \langle \overline{u'w'} \rangle - \langle \overline{u}'' \overline{w}'' \rangle \,, \tag{2.5}$$

is the sum of the viscous stress, $\nu \partial \langle \overline{u} \rangle / \partial z$ (where ν is the kinematic viscosity), the familiar Reynolds stress, $-\langle \overline{u'w'} \rangle$, and a dispersive stress, $-\langle \overline{u}'' \overline{w}'' \rangle$, that arises due to heterogeneity of the time-averaged velocity within the plant canopy. The drag term is composed of two

components, $f = f_p + f_\nu$ where the form (or pressure) drag force per unit fluid mass, f_p, is given by

$$f_p \equiv \frac{1}{\rho} \left\langle \frac{\partial \overline{p}''}{\partial x} \right\rangle \tag{2.6}$$

where ρ is the fluid density and p is pressure; and the viscous drag force per unit fluid mass, f_ν, is given by

$$f_\nu \equiv -\nu \left\langle \nabla^2 \overline{u}'' \right\rangle . \tag{2.7}$$

Since Raupach and Shaw (1982), models have been based on the assumption that the dispersive stress, $-\langle \overline{u}''\overline{w}'' \rangle$, is negligibly small compared to the Reynolds stress, $-\langle \overline{u'w'} \rangle$. There is plenty of experimental evidence that the dispersive stress is negligible above the plant canopy (e.g., Raupach et al., 1986; Poggi et al., 2004a), but within the plant canopy, Poggi et al. (2004a) and also Bohm et al. (2000) measured large dispersive stresses. Comparing a range of canopy densities at Reynolds numbers over $100,000$ (based on the depth average velocity and the water depth), Poggi et al. (2004a) found that for canopies of density $ah > 0.1$, where h is the canopy height, the dispersive stress is everywhere less than 10% of the Reynolds stress, but for sparse canopies, the dispersive stress can be on the order of the Reynolds stress. This observation is consistent with measurements by Raupach et al. (1986) and Bohm et al. (2000). In this paper, we assume that the dispersive stress is negligible in dense canopies (where 'dense' is defined as $ah > 0.1$) at slightly lower Reynolds number than Poggi et al. (2004a), but this should be verified in the future.

2.2.2 Kinetic Energy Equations

The total kinetic energy, $1/2\langle\overline{u_i u_i}\rangle$, may be decomposed into mean kinetic energy (MKE), dispersive kinetic energy (DKE), and turbulent kinetic energy (TKE) as follows:

$$\tfrac{1}{2}\langle\overline{u_i u_i}\rangle = \underbrace{\tfrac{1}{2}\langle\overline{u}_i\rangle\langle\overline{u}_i\rangle}_{\text{MKE}} + \underbrace{\tfrac{1}{2}\langle\overline{u}_i''\overline{u}_i''\rangle}_{\text{DKE}} + \underbrace{\tfrac{1}{2}\langle\overline{u_i' u_i'}\rangle}_{\text{TKE}}. \tag{2.8}$$

Turbulent Kinetic Energy (TKE)

The governing equation for TKE in steady, uniform, open channel flow is

$$\frac{\partial T_z}{\partial z} = P_s + P_w - \varepsilon. \tag{2.9}$$

where T_z is the transport term, P_s and P_w are production terms, and ε is the dissipation term. In flow through plant canopies, there are two mechanisms that produce TKE, represented by the two production terms. As in open water, TKE is produced by work of the Reynolds stress against the mean velocity gradient at rate P_s, defined by

$$P_s \equiv -\left\langle\overline{u'w'}\right\rangle \frac{\partial\left\langle\overline{u}\right\rangle}{\partial z}. \tag{2.10}$$

Additionally, TKE is produced in the wakes of plant stems at rate P_w, defined by

$$P_w \equiv -\left\langle\overline{u_i' u_j'}''\frac{\partial\overline{u}_i''}{\partial x_j}\right\rangle. \tag{2.11}$$

Historically, P_s has been called 'shear production' and P_w has been called 'wake production', and we adopt this nomenclature for consistency with previous work, although it is somewhat misleading because both 'wake' and 'shear' production involve shear. The turbulent transport, T_z, is defined by

$$T_z \equiv \tfrac{1}{2}\left\langle\overline{u_i' u_i' w'}\right\rangle + \frac{1}{\rho}\left\langle\overline{p'w'}\right\rangle - \nu\left\langle\overline{u_i'\left(\frac{\partial u_i'}{\partial z} + \frac{\partial w'}{\partial x_i}\right)}\right\rangle + \tfrac{1}{2}\left\langle\overline{u_i' u_i'}''\overline{w}''\right\rangle \tag{2.12}$$

and is identical to the turbulent transport in open water with the exception of the final term, a dispersive transport term.

Just as in the open water equations, the rate of dissipation of TKE to heat, or 'dissipation' for short, is defined by

$$\varepsilon \equiv \nu \left\langle \overline{\frac{\partial u_i'}{\partial x_j}\left(\frac{\partial u_i'}{\partial x_j}+\frac{\partial u_j'}{\partial x_i}\right)} \right\rangle . \tag{2.13}$$

Note that we have separated the viscous transport from the dissipation of TKE to heat whereas Raupach and Shaw (1982) and others lump these terms together.

Dispersive Kinetic Energy (DKE)

The governing equation for DKE in steady, uniform flow is

$$\frac{\partial \tilde{T}_z}{\partial z} = \tilde{P}_s + \tilde{P}_p - \tilde{\varepsilon} - P_w \tag{2.14}$$

where $\tilde{P}_s$, defined as

$$\tilde{P}_s \equiv -\left\langle \overline{u}''\overline{w}'' \right\rangle \frac{\partial \left\langle \overline{u} \right\rangle}{\partial z}, \tag{2.15}$$

is production of DKE through work of the dispersive flux against the mean velocity gradient; $\tilde{P}_p$, defined as

$$\tilde{P}_p \equiv \left\langle \overline{u} \right\rangle \frac{1}{\rho}\left\langle \frac{\partial \overline{p}''}{\partial x} \right\rangle = \left\langle \overline{u} \right\rangle f_p, \tag{2.16}$$

is production of DKE through work of the mean velocity against the form drag; $\tilde{T}_z$, defined as

$$\tilde{T}_z \equiv \tfrac{1}{2}\left\langle \overline{u}_i''\overline{u}_i''\overline{w}'' \right\rangle + \frac{1}{\rho}\left\langle \overline{p}''\overline{w}'' \right\rangle - \nu \left\langle \overline{u}_i''\left(\frac{\partial \overline{u}_i''}{\partial z}+\frac{\partial \overline{w}''}{\partial x_i}\right) \right\rangle + \tfrac{1}{2}\left\langle \overline{u}_i''\overline{u_i'w'}'' \right\rangle, \tag{2.17}$$

is the transport of DKE; and $\tilde{\varepsilon}$, defined as

$$\tilde{\varepsilon} \equiv \nu \left\langle \frac{\partial \overline{u}_i''}{\partial x_j}\left(\frac{\partial \overline{u}_i''}{\partial x_j}+\frac{\partial \overline{u}_j''}{\partial x_i}\right) \right\rangle, \tag{2.18}$$

is the rate of dissipation of DKE to heat. Notice in equation 2.14 that dissipation to heat is not the only sink for DKE; DKE is also converted into TKE through the wake production term, P_w, which was defined in equation 2.11. Also notice that viscous drag does not contribute to production of DKE – this is not an assumption but a result of the derivation of equation 2.14.

In Section 2.2.1, we discuss evidence that the dispersive momentum flux, $\langle \overline{u}''\overline{w}'' \rangle$, is small throughout and above dense canopies (canopies having $ah > 0.1$). Raupach and Shaw (1982) further assumed that all dispersive fluxes are small. Under this assumption, the governing equation for DKE equation 2.14 simplifies to

$$\tilde{P}_p = \tilde{\varepsilon} + P_w. \tag{2.19}$$

López and García (2001) point out that there are two limiting cases for the DKE budget based on the relative scale of the plant stems (d) and the Kolmogorov microscale (η). Note that these limiting cases apply only when the dispersive fluxes are, indeed, negligible:

1. When $d >> \eta$, dissipation of DKE is negligible, i.e., $\tilde{\varepsilon} \approx 0$, and the DKE budget simplifies to

$$P_w \approx \tilde{P}_p = \langle \overline{u} \rangle f_p. \tag{2.20}$$

2. When $d < \eta$, DKE produced by the work of the mean flow against plant stems is immediately dissipated to heat, i.e., $\tilde{P}_p \approx \tilde{\varepsilon}$, and thus the DKE budget simplifies to

$$P_w \approx 0. \tag{2.21}$$

The relative scale of d and η is determined by the stem Reynolds number, $Re_d \equiv Ud/\nu$. At high Re_d, $d >> \eta$, and at small Re_d, $d < \eta$. In either of these limiting cases, we obtain a simple closure for wake production, P_w, which appears in the governing equation for

TKE, equation 2.9. If dispersive fluxes cannot be neglected, which appears to be the case in sparse canopies (i.e., canopies for which $ah < 0.1$), the closure of the TKE equation is not so simple. Our model, like existing RANS models for flow through vegetation, is based on the assumptions that dispersive fluxes are negligible and that $d >> \eta$ so that equation 2.20 holds.

2.3 Physical Processes

We have developed our k–ε model for applications in real aquatic vegetation, which is often characterized by a frontal area density profile, $a(z)$, that varies strongly in the vertical direction. However, the structure of the model is motivated by the physical processes observed in two very simple laboratory canopies. The simplest case for which $a(z)$ varies in the vertical direction is a model canopy of submerged rigid cylinders, illustrated in figure 2.3(*a*). In submerged cylinders, $a(z)$ is a step function, equal to a constant, a_0, within the canopy and zero above the canopy, as illustrated in figure 2.3(*b*). There is an easily identifiable length scale over which $a(z)$ varies – the height of the cylinders, h. Thus, in submerged cylinders, there are four relevant length scales: the cylinder height, h, the water depth, H, the cylinder diameter, d, and the inverse frontal area density, a_0^{-1}.

An even simpler case is a model canopy of emergent cylinders, illustrated in figure 2.3(*c*). In this case, the cylinders reach (or protrude above) the water surface, so there are only three relevant length scales: H, d, and a_0^{-1}. Provided that the cylinder array is not too sparse, canopy drag dominates vertical shear and there are no vertical gradients, so we may neglect H, leaving only two relevant length scales: d and a_0^{-1}. In this section, we first consider the physics of flow through dense canopies of emergent cylinders before moving

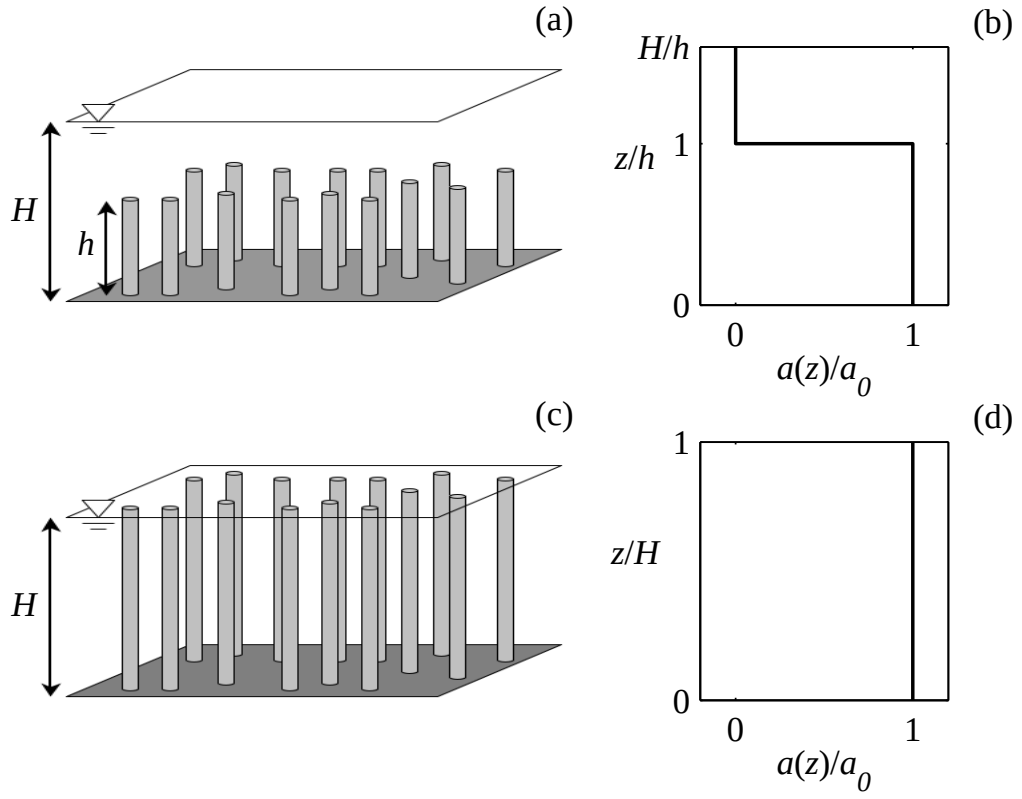

Figure 2.3: Illustrations of submerged (*a*) and emergent (*c*) cylinders, and plots of the frontal area density profile for submerged (*b*) and emergent (*d*) cylinders.

on to consider the additional processes present in flow through submerged cylinders. The processes that enhance mixing in submerged cylinders are the same processes that enhance mixing in real plants that have more interesting frontal area profiles.

2.3.1 Emergent Cylinders

In canopies of sufficiently dense emergent cylinders, it has been observed that there are no vertical gradients, i.e., $\partial/\partial z = 0$, except very close to the bed, and drag at the bed is negligibly small compared to drag on the cylinders. Thus, the momentum equation

(equation 2.4) in the bulk fluid simplifies to:

$$0 = gS - f. \tag{2.22}$$

It is not clear exactly where the transition between 'sparse' and 'dense' occurs for emergent cylinders, but extrapolating from the work of Luhar et al. (2008) in submerged vegetation, we may estimate that vertical shear is negligible in emergent vegetation for $C_D aH/(1-\phi) \gtrsim 0.1$ where C_D is the drag coefficient and ϕ is the volume fraction occupied by the cylinders.

The drag force per unit fluid mass follows the quadratic drag law

$$f = \frac{1}{1-\phi}\tfrac{1}{2}C_D a|U|U \tag{2.23}$$

where we have introduced the shorthand $U \equiv \langle \overline{u} \rangle$ for the mean velocity. It is possible to solve equation 2.22 and equation 2.23 analytically for the mean velocity, yielding

$$U = \pm\sqrt{\frac{2gS(1-\phi)}{C_D a}}. \tag{2.24}$$

In the absence of vertical gradients, the TKE equation 2.9 simplifies to

$$P_w = \varepsilon. \tag{2.25}$$

Tanino and Nepf (2008b) argue that in the wakes of emergent plants, dissipation scales with TKE and with plant diameter as follows:

$$\varepsilon \sim \frac{k^{3/2}}{d} \tag{2.26}$$

provided that the inter-stem spacing is at least twice the stem diameter. Assuming that $\eta << d$, we argued in Section 2.2.2 that $P_w \approx U f_p$. Following Tanino and Nepf (2008b),

for convenience, we may write separate quadratic drag laws for the pressure drag and the viscous drag, as follows:

$$f_p = \frac{1}{1-\phi}\tfrac{1}{2}C_{Dp}a|U|U \tag{2.27}$$

$$f_\nu = \frac{1}{1-\phi}\tfrac{1}{2}C_{D\nu}a|U|U. \tag{2.28}$$

where we have decomposed the drag coefficient $C_D = C_{Dp} + C_{D\nu}$ into pressure and viscous contributions, respectively. Combining equations 2.20 and 2.27, and allowing for some inefficiency in conversion of DKE to TKE, we arrive at

$$P_w \sim \frac{1}{1-\phi}\tfrac{1}{2}C_{Dp}a|U|^3. \tag{2.29}$$

Solving equations 2.25, 2.26, and 2.29 for TKE, Tanino and Nepf (2008b) found that in emergent vegetation,

$$k = \gamma U^2 \left(\frac{1}{1-\phi}\tfrac{1}{2}C_{Dp}ad\right)^{2/3} \tag{2.30}$$

where we have introduced the shorthand $k \equiv \frac{1}{2}\langle\overline{u_i'u_i'}\rangle$ for TKE and γ is an empirical constant. Tanino and Nepf (2008b) measured $\gamma = 1.21$ in rigid, emergent cylinders. In general (even in plants with more complicated geometries), we expect γ to be order one provided that we can identify a characteristic diameter for the dissipation scaling.

In summary, in steady, fully developed, open channel flow through emergent cylinders, at high Reynolds number (greater than around $100,000$, based on U and H) and with a high enough cylinder density, i.e., $C_DaH/(1-\phi) \gtrsim 0.1$, there are no vertical gradients, and we have the analytical solutions for the mean velocity and TKE, given in equations 2.24 and 2.30, respectively. These solutions are based on the free surface slope, the canopy drag coefficient, the frontal area density, and the cylinder diameter. Provided that the cylinders are sufficiently dense, there is only one identifiable dimensionless independent variable for the emergent problem: $C_{Dp}ad/(1-\phi)$. This parameter is related to the volume fraction occupied by the cylinders (for cylinders, the volume fraction is $\phi = \pi/4\,ad$).

2.3.2 Submerged Cylinders

In submerged cylinders, vertical gradients are very important. Provided that dispersive fluxes and the viscous stress are small, the momentum equation (2.4) simplifies to

$$0 = gS - \frac{\partial \langle \overline{u'w'} \rangle}{\partial z} - f. \tag{2.31}$$

The relative magnitude of the momentum transport and the drag force determines the qualitative nature of the flow. Arguing that the momentum transport scales as $\partial \langle \overline{u'w'} \rangle / \partial z \propto U^2/h$, and employing the quadratic drag law (equation 2.23) with a small plant volume fraction ($\phi \approx 0$), Luhar et al. (2008) identify the dimensionless parameter $C_D a h$, which is the ratio of drag to momentum transport. They observe that in sparse canopies (where $C_D a h \lesssim 0.04$), momentum transport dominates, and flow resembles a rough boundary layer, while in dense canopies (where $C_D a h \gtrsim 0.1$), drag dominates, and a mixing layer forms with the inflection point in mean velocity just below the top of the canopy. For non-negligible values of ϕ, the dimensionless parameter representing the ratio of drag to momentum transport is $C_D a h/(1-\phi)$.

The TKE budget in a submerged canopy is governed by the full equation 2.9. There are two distinct mechanisms of TKE production, represented by the terms P_s and P_w, and it is significant that the TKE produced by these two mechanisms has different characteristic length scales as this alters the pathways of dissipation. Vertical shear, and the turbulence generated by classic shear production, P_s, scales with the distance(s) over which $a(z)$ varies (in the case of rigid cylinders, this scale is h). TKE generated in the wakes of plant stems at rate P_w, on the other hand, scales with the characteristic diameter of the plant stems, d. These distinct scales are clearly visible in the energy spectra of both terrestrial and aquatic vegetation, e.g., see figure 2.8 of this paper and figure 5 of Poggi et al. (2004b). Shaw and Seginer (1985) coined the terms 'shear kinetic energy' (or SKE) and 'wake ki-

netic energy' (or WKE) for the components of TKE produced by mean vertical shear and in the wakes of plant stems, respectively.

There is an additional important mechanism that is not explicit in the governing equation for TKE (2.9): energy is converted from SKE to WKE in the wakes of plant stems. Just as the mean flow does work against the mean plant drag to produce WKE and heat, large scale turbulent eddies do work against the fluctuating plant drag, converting SKE to WKE and heat. Assuming that DKE is negligible, that $d >> \eta$, and that the instantaneous plant drag may be parameterized by a quadratic law similarly to the mean drag, Finnigan (2000) writes that the rate (per unit mass) at which TKE is converted to WKE and heat in the wakes of plants is

$$W = \frac{1}{1-\phi}\tfrac{1}{2}C_{Dp}a|\langle|\vec{u}|u_i u_i\rangle - U^3| \tag{2.32}$$

Note that we have added the factor $(1-\phi)^{-1}$ to Finnigan's expression to allow for canopies of significant volume fraction. W is the work done by the instantaneous flow field against the instantaneous drag minus the work done by the mean flow field against the mean drag, which is the work done by the turbulence. Using a binomial expansion to approximate equation 2.32 to second order results in

$$W \approx \frac{1}{1-\phi}\tfrac{3}{4}C_{Dp}a|U|\tfrac{1}{2}\langle\overline{u_i' u_i'}\rangle. \tag{2.33}$$

Let us call W the 'spectral shortcut' since it diverts SKE (at the scale of vertical shear) to WKE (at the smaller scale of the plant wakes).

Both SKE and WKE are dissipated via the turbulent eddy cascade as some of the SKE is diverted to WKE via the spectral shortcut. We may partition the total dissipation ε into the components ε_s and ε_w, representing the dissipation of SKE and WKE, respectively, through the energy cascade. A flow chart illustrating the energy pathways in submerged vegetation is given in figure 2.4. A similar flow chart was first published in Shaw and

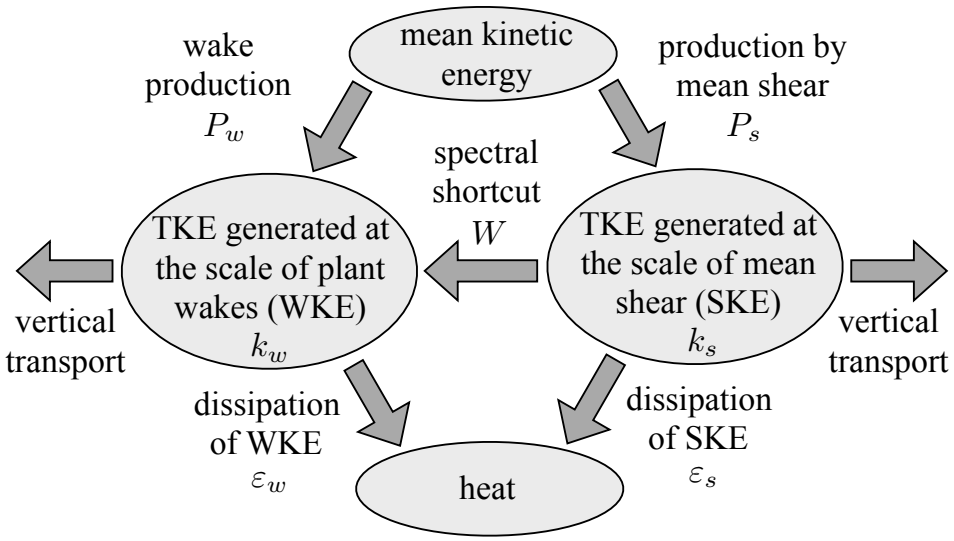

Figure 2.4: Energy flow chart for steady uniform open-channel flow through submerged vegetation or through emergent vegetation having a non-uniform frontal area profile. A small amount of mean kinetic energy is also dissipated to heat (not illustrated).

Seginer (1985). Note that Wilson (1988) referred to this chart, and developed a Reynolds stress type model consistent with the energy pathways it illustrates, but fell short of including k_w in his model equations.

In summary, in submerged vegetation, there are three identifiable dimensionless parameters governing the shape of the velocity, TKE, and Reynolds stress profiles. The submergence ratio, H/h, governs the transition between deeply submerged and fully emergent vegetation. The parameter $C_D ah/(1-\phi)$, identified by Luhar et al. (2008) as the ratio of drag force and vertical momentum transport, influences the shape of the velocity profile, in particular determining whether it is analogous to a rough boundary layer or a mixing layer. Finally, the parameter $C_{Dp} ad/(1-\phi)$, which is related to the plant volume fraction and governs the turbulence intensity in emergent vegetation, also has some influence in submerged vegetation through the scaling of WKE dissipation with d.

2.4 Proposed Model

In this section, we propose a k–ε model that naturally transitions from deeply submerged to emergent vegetation and is predictive over a wide range of all three dimensionless parameters: H/h, $C_D ah/(1-\phi)$, and $C_{Dp} ad/(1-\phi)$. Existing k–ε models for flow through aquatic vegetation do not include stem diameter, and thus miss the effects of $C_{Dp} ad/(1-\phi)$. Inclusion of $C_{Dp} ad/(1-\phi)$ is the main distinguishing feature of the new model. Our approach is to break TKE into its two components: SKE and WKE, and to treat dissipation of these two components separately. At this point, the model is for fully developed steady flow, and is appropriate for dense canopies (having $ah > 0.1$) and sufficiently high Reynolds number that dispersive fluxes and the viscous stress are negligible and that $d >> \eta$.

2.4.1 Momentum Equation

Our model momentum equation is identical to the momentum equation for existing k–ε models such as those discussed in López and García (2001), Katul et al. (2004), and others. Assuming that dispersive fluxes and the viscous stress are negligible, the governing equation for momentum is given by equation 2.31. As in the standard model (Launder and Spalding, 1974), we adopt the gradient diffusion hypothesis to model the Reynolds stress as follows:

$$\langle \overline{u'w'} \rangle = -\nu_T \frac{\partial U}{\partial z} \tag{2.34}$$

where ν_T is the eddy viscosity, and arrive at the following model momentum equation:

$$0 = gS + \frac{\partial}{\partial z}\left(\nu_T \frac{\partial U}{\partial z}\right) - f \tag{2.35}$$

The quadratic drag law, given in equation 2.23, is used to parameterize the drag, f. We discuss the parameterization of eddy viscosity in Section 2.4.3.

2.4.2 TKE and Dissipation

We split TKE into two components, SKE (denoted k_s) and WKE (denoted k_w), so that total TKE is given by

$$k = k_s + k_w. \tag{2.36}$$

We also split dissipation into two components: dissipation of SKE through the energy cascade (denoted by ε_s) and dissipation of WKE (denoted by ε_w) so that total dissipation (ε) is given by

$$\varepsilon = \varepsilon_s + \varepsilon_w. \tag{2.37}$$

The model equation for SKE is

$$0 = \frac{\partial}{\partial z}\left(\frac{\nu_T}{\sigma_k}\frac{\partial k_s}{\partial z}\right) + P_s - W - \varepsilon_s, \tag{2.38}$$

and the model equation for WKE is

$$0 = \frac{\partial}{\partial z}\left(\frac{\nu_T}{\sigma_k}\frac{\partial k_w}{\partial z}\right) + P_w + W - \varepsilon_w. \tag{2.39}$$

The standard model constant $\sigma_k = 1.0$ (Launder and Spalding, 1974) is used in both equations. Shear production is modeled as

$$P_s = \nu_T\left(\frac{\partial U}{\partial z}\right)^2 \tag{2.40}$$

just as in the standard model. Wake production is modeled as

$$P_w = \beta_p \frac{1}{1-\phi}\tfrac{1}{2}C_{Dp}a|U|^3, \tag{2.41}$$

and the spectral shortcut is modeled as

$$W = \beta_d \frac{1}{1-\phi} \tfrac{1}{2} C_{Dp} a |U| k_s \tag{2.42}$$

where β_p and β_d are new model constants. P_w has been modeled as discussed in Section 2.2.2, assuming that the stem scale, $d >> \eta$. W is calculated using SKE alone, instead of the total TKE found in equation 2.33, so that W goes to zero in the absence of SKE.

The model equation for dissipation of SKE through the energy cascade is

$$0 = \frac{\partial}{\partial z}\left(\frac{\nu_T}{\sigma_\varepsilon}\frac{\partial \varepsilon_s}{\partial z}\right) + \frac{\varepsilon_s}{k_s}\left(C_{\varepsilon 1} P_s - C_{\varepsilon 2}\varepsilon_s - C_{\varepsilon 5} W\right) \tag{2.43}$$

where $\sigma_\varepsilon = 1.3$, $C_{\varepsilon 1} = 1.44$, and $C_{\varepsilon 2} = 1.92$ are standard model constants (Launder and Spalding, 1974). The SKE-dissipation equation differs from the standard model equation for dissipation only in its inclusion of W and the new model constant $C_{\varepsilon 5}$. We have included W but not P_w or ε_w in this dissipation equation under the assumption that dissipation of SKE will be largely unaffected by the rate of production or dissipation of the smaller scale WKE.

Following Tanino and Nepf (2008b), we use the following algebraic equation to model dissipation of WKE:

$$\varepsilon_w = C_{\varepsilon D} \frac{k_w^{3/2}}{d} \tag{2.44}$$

where $C_{\varepsilon D}$ is a new model constant.

2.4.3 Eddy Viscosity

The eddy viscosity is parameterized by

$$\nu_T = C_\mu \frac{k_s^2}{\varepsilon_s} + C_\lambda \frac{k_w^2}{\varepsilon_w} \tag{2.45}$$

where $C_\mu = 0.09$ is a standard model constant (Launder and Spalding, 1974) and C_λ is a new model constant. Here we have assumed that SKE and WKE contribute to momentum diffusion in an additive way (analogous to turbulent and molecular diffusion of scalars). In fact, we expect SKE and WKE to interact once they are generated, but it seems reasonable to assume that these contributions to momentum diffusion are additive to first order, and making this assumption ensures that in the absence of vegetation, where k_w goes to zero, the eddy viscosity collapses to the standard parameterization. Since the standard constant C_μ is tuned for mixing layers, plane jets, and boundary layers, we have introduced a different constant, C_λ, for momentum transport via wake turbulence.

2.4.4 Limiting Cases

In the limiting case of no plants, all TKE is SKE, $W = 0$, and the model equations collapse to the standard model equations. In the limiting case of dense emergent vegetation, where vertical gradients are small, the momentum equation collapses to $gS = f$, yielding the solution for mean velocity given in equation 2.24, and production, P_s, is negligible, so no SKE is ever generated, and the model equation for WKE becomes $P_w = \varepsilon_w$, in agreement with equation 2.25. For consistency with the solution for TKE given in equation 2.30, the model constants $C_{\varepsilon D}$ and β_p must be related by

$$C_{\varepsilon D} = \beta_p \gamma^{-3/2}. \tag{2.46}$$

We use $\gamma = 1.21$ as found by Tanino and Nepf (2008b).

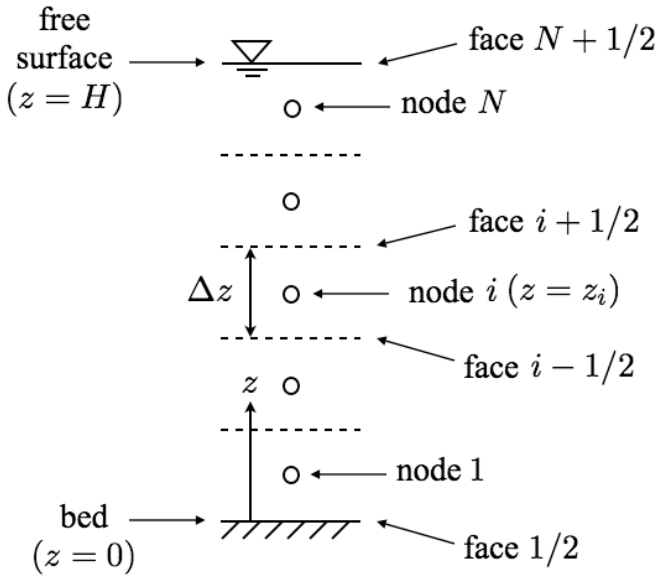

Figure 2.5: Illustration of the numerical mesh.

2.4.5 Numerical Implementation

Our numerical algorithm employs a finite volume spatial discretization, illustrated in figure 2.5, and a Crank-Nicolson time iteration method (we add a time derivative and allow the equations to relax to steady state). U is evaluated at the nodes, and TKE and dissipation are evaluated at the faces so that ν_T may easily be evaluated at the faces. The convergence criterion is that the larger of the source or sink terms comes within 0.1% of the smaller of the source or sink terms plus the transport term for all four of the transport equations (momentum, SKE, WKE, and dissipation of SKE).

2.4.6 Boundary Conditions

Our boundary conditions are consistent with the open water boundary conditions described in Burchard and Peterson (1999). We have chosen open water boundary conditions because in dense vegetation, the numerical solution is not sensitive to boundary conditions (i.e., we can get away with it), and the open water boundary conditions provide for a smooth transition between flow through vegetated canopies and open water flows, e.g., in the context of three-dimensional hydrodynamic models used in field applications where vegetation may not cover the entire bed.

For the momentum boundary condition at the bed, the shear stress is specified as follows:

$$\nu_T \frac{\partial U}{\partial z} = u_{*,b}^2 \text{ at } z = 0. \tag{2.47}$$

The friction velocity, $u_{*,b}$, is estimated from the mean velocity at node 1, U_1, using the quadratic drag law

$$u_{*,b}^2 = C_{D,b} U_1^2 \tag{2.48}$$

where $C_{D,b}$ is a drag coefficient. Assuming a logarithmic velocity profile near the bed, we may calculate $C_{D,b}$ from the roughness height, $z_{0,b}$, as follows:

$$C_{D,b} = \left(\frac{1}{\kappa} \ln \frac{z_1}{z_{0,b}} \right)^{-2} \tag{2.49}$$

where $\kappa = 0.41$ is the von Kármán constant and z_1 is the elevation of node 1.

For the momentum boundary condition at the free surface, the shear stress is specified as follows:

$$\nu_T \frac{\partial U}{\partial z} = u_{*,s}^2 \text{ at } z = H. \tag{2.50}$$

The friction velocity, $u_{*,s}$, is estimated from the wind speed U_{10}, measured at a standard

10 m above the water surface, using the quadratic drag law

$$u_{*,s}^2 = C_{D,s} U_{10}^2. \tag{2.51}$$

For laboratory flows, we have set $U_{10} = 0$. Wüest and Lorke (2003) provide a nice overview of estimates for $C_{D,s}$ in the field.

For SKE, we use the following Dirichlet boundary condition at the bed:

$$k_s = \frac{u_{*,b}^2}{\sqrt{C_\mu}} \text{ at } z = 0 \tag{2.52}$$

and a zero stress boundary condition near the free surface:

$$\frac{\nu_T}{\sigma_k} \frac{\partial k_s}{\partial z} = 0 \text{ at } z = z_N. \tag{2.53}$$

For WKE, we use zero stress boundary conditions near the bed and near the free surface:

$$\frac{\nu_T}{\sigma_k} \frac{\partial k_w}{\partial z} = 0 \text{ at } z = z_1 \text{ and } z = z_N. \tag{2.54}$$

For dissipation of SKE, we use the following Dirichlet condition at the bed:

$$\varepsilon_s = C_\mu^{3/4} \frac{k_s^{3/2}}{\kappa(z_1 + z_{0,b})} \text{ at } z = 0 \tag{2.55}$$

and the following Neumann condition near the free surface:

$$\frac{\nu_T}{\sigma_\varepsilon} \frac{\partial \varepsilon_s}{\partial z} = \frac{C_\mu}{\sigma_\varepsilon} \frac{k_s^2}{(H - z_N) + z_{0,s}} \text{ at } z = z_N \tag{2.56}$$

where the surface roughness, $z_{0,s}$, is zero in the case of no wind stress.

There is no need for a boundary condition for dissipation of WKE because ε_w is an algebraic function of k_w.

2.5 Experiments

For model calibration, four experiments were conducted in an open channel flume in the DeFrees Hydraulics Laboratory at Cornell University. For model validation, we used twelve experiments described in Dunn et al. (1996) that were conducted in the Hydrosystems Laboratory at the University of Illinois at Urbana-Champaign. Both sets of experiments were conducted in canopies of rigid cylinders. The experimental methods and results are described in this section.

2.5.1 Cornell University Experiments

Methods

A diagram of the experimental setup is provided in figure 2.6. The 4.50 m long, 0.600 m wide recirculating type open channel flume at Cornell was fitted with 3.60 m long, 0.600 m wide arrays of randomly located, rigid, vertically mounted acrylic cylinders. The random cylinder locations were chosen from a uniform distribution of possible locations constrained by the criteria that the center of cylinders must be a minimum of two diameters apart and that the surface of all cylinders must be located at minimum 3.2 mm ($1/8$ in) from the edge of a plate. The cylinders were inserted into holes CNC machined into 6.4 mm ($1/4$ in) thick PVC 0.600 m wide base plates with lengths of 1.20 m (4.00 ft). The random array pattern is periodic in the longitudinal direction with periodic length scale the array plate length, i.e., 1.20 m.

Two acrylic cylinder arrays were used, comprised of 0.200 m long cylinders, one with cylinders of 3.2 mm ($1/8$ in) diameter and the other with cylinders of 25.4 mm (1 in) di-

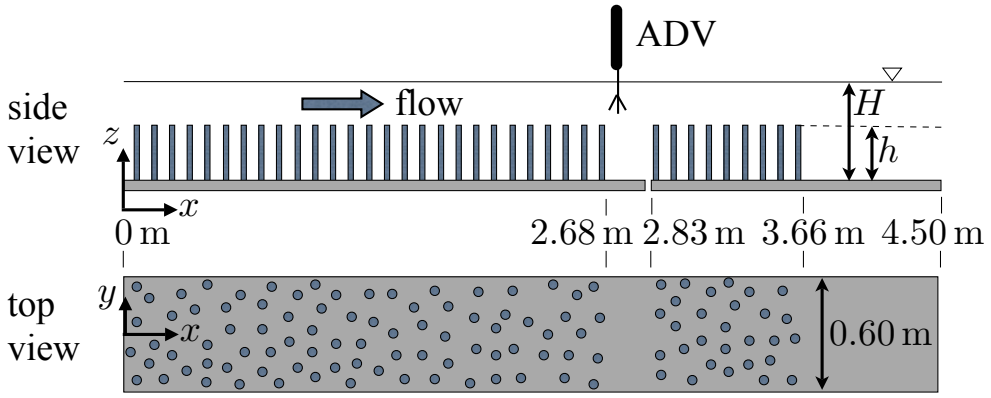

Figure 2.6: Diagram of the flume, cylinders, instrumentation, and coordinate system used in the Cornell University experiments. The number of cylinders and the locations of the individual cylinders are not accurately illustrated, nor are the cylinders drawn to scale. The locations of the cylinder array edges are illustrated accurately.

ameter, each populated to a frontal area density of $a = 4.00\,\mathrm{m}^{-1}$ (1260 cylinders/m^2 and 158 cylinders/m^2, respectively). Cylinders were removed from a 150 mm long gap that begins 2.80 m from the upstream end of the random array plates in order to allow for instrument access. For the experiments discussed here, measurements were taken at the upstream edge of the gap with two Nortek Vectrino acoustic Doppler velocimeters (ADVs) configured with the Vectrino+ firmware allowing sample rates to 200 Hz. Dye visualizations and ADV measurements confirmed that the gap was sufficiently narrow to have no discernible impact on the flow. Steady fully developed flow was established and verified, in the emergent case, by the absence of longitudinal gradients in mid-depth ADV measurements along the length of the cylinder array, and, in the submerged case, by measurements of a fully developed linear Reynolds stress profile above the canopy.

For each of the two cylinder diameters, experiments were conducted under emergent ($H/h < 1$) and submerged ($H/h = 1.5$) conditions. To account for high lateral variabil-

ity in the flow due to the cylinder wakes, measurements were taken at seven transverse coordinates, $y = \{90, 160, 230, 300, 370, 440, 510\}$ mm, where y is the distance from the left wall of the flume, looking downstream. At each transverse coordinate, measurements were taken at six depths for the emergent cases and twelve or thirteen depths for the submerged cases. The ADV was oriented to look either downward or upstream depending on the measurement location (the upstream-looking orientation was necessary to obtain measurements within 50 mm of the free surface). Records were collected with ADVs sampling at 200 Hz for 10 min at each measurement location.

To obtain estimates of U, $\langle\overline{u'w'}\rangle$, and $k \equiv 1/2\langle\overline{u_i'u_i'}\rangle$, traditional Reynolds decomposition (in time) and averaging were performed first, then spatial averages were taken over the seven lateral measurement locations at a given elevation. Because measurements were taken in a gap that was free of cylinders, measured mean longitudinal velocities and Reynolds stresses were multiplied by $(1-\phi)^{-1}$ to correct for the expansion of flow into the gap. In order to estimate the uncertainty due to lateral flow variability not captured by the seven measurement locations, a bootstrap sampling technique was applied (Efron and Tibshirani, 1993): seven time-averaged statistics were sampled with replacement 1000 times from the original seven measured statistics, the mean was calculated for each sample of seven, and histograms of the means were used to obtain the upper and lower bounds of the 95% confidence interval. To compute power spectra, each 200 Hz velocity time series was time-averaged down to a sampling frequency of 50 Hz, then spectra were computed using ten sub-windows and averaged across the seven lateral sampling locations.

The pressure drag coefficient, C_{Dp}, was evaluated by fitting measurements of k and U to equation 2.30 in the emergent cases using $\gamma = 1.21$ from Tanino and Nepf (2008b). Tanino and Nepf (2008a) found that C_{Dp} is independent of Reynolds number, varying

only with the cylinder volume fraction ϕ, so we assume that C_{Dp} in each submerged case is equivalent to C_{Dp} in the emergent case with the corresponding ϕ. The viscous drag coefficient, $C_{D\nu}$ was evaluated from the standard curve of drag coefficient vs. Reynolds number for a single cylinder, found in any introductory fluids text (e.g., Finnemore and Franzini, 2002, p. 383), with one subtracted to account for the pressure drag on a single cylinder. We assume that the viscous drag is independent of ϕ.

The water surface slope, S, was estimated from the velocity statistics. For the emergent cylinder experiments, S was estimated using the depth-average velocity, the total drag coefficient, and equation 2.24. For the submerged cylinder experiments, S was estimated from the balance of the momentum flux and the gravitational force in the open water region, $gS = \partial\langle\overline{u'w'}\rangle/\partial z$, as follows. First, the Reynolds stress at the top of the canopy, $\langle\overline{u'w'}\rangle_h$ was estimated from a linear least squares fit to the Reynolds stress data above the canopy, assuming that $\langle\overline{u'w'}\rangle = 0$ at $z = H$. Then, $\langle\overline{u'w'}\rangle_h$ was used to calculate the friction velocity scale $u_* \equiv |\langle\overline{u'w'}\rangle_h|^{1/2}$. Finally, the slope was estimated as $S = u_*^2/g\,(H-h)^{-1}$.

Geometric parameters, velocity scales, drag coefficients, and Reynolds numbers for the Cornell University experiments are reported in table 2.1, and the dimensionless parameters governing the flow are reported in table 2.2.

Results

Power spectra are plotted in figure 2.7 for the emergent cylinder experiments (E1 and E2) and in figure 2.8 for the submerged cylinder experiments (S1 and S2). In 1941, Kolmogorov hypothesized that in any turbulent flow at sufficiently high Reynolds number, turbulent eddies having length scale well below the energy-producing scale and well above the viscous length scale would be isotropic and independent of viscosity, result-

Experiment	E1	E2	S1	S2
d (cm)	0.32	2.54	0.32	2.54
a (cm^{-1})	0.0400	0.0400	0.0400	0.0400
ϕ	0.010	0.010	0.080	0.080
H (cm)	16.5	16.0	29.6	29.6
h (cm)	–	–	19.7	19.3
U_Q ($\mathrm{cm\,s}^{-1}$)	5.58	6.38	13.5	15.6
U_0 ($\mathrm{cm\,s}^{-1}$)	5.58	6.38	6.46	7.10
U_h ($\mathrm{cm\,s}^{-1}$)	–	–	17.5	18.1
u_* ($\mathrm{cm\,s}^{-1}$)	–	–	3.26	3.14
Re_H	$9,210$	$10,200$	$40,000$	$46,300$
Re_d	177	$1,621$	205	$1,803$
C_{Dp}	1.48	1.08	1.48	1.08
$C_{D\nu}$	0.40	0.00	0.31	0.00
C_D	1.88	1.08	1.79	1.08

Table 2.1: Geometric parameters, velocities, Reynolds numbers, and drag coefficients for the Cornell University expierments. U_Q is the laterally- and depth-averaged mean velocity; $U_0 = U_Q$ for the emergent cylinder experiments (E1 and E2) and U_0 is the average of the three laterally-averaged mean velocities measured nearest the bed for the submerged cylinder experiments (S1 and S2); U_h is the laterally-averaged mean velocity at the top of the cylinders; $Re_H \equiv U_Q H/\nu$; and $Re_d \equiv U_0 d/\nu$.

Experiment	H/h	$C_D ah/(1-\phi)$	$C_{Dp} ad/(1-\phi)$
E1	≤ 1	1.26	0.019
E2	≤ 1	0.75	0.119
S1	1.50	1.43	0.019
S2	1.53	0.90	0.119

Table 2.2: Dimensionless parameters for the Cornell University experiments. Note that $C_D aH/(1-\phi)$ is reported in place of $C_D ah/(1-\phi)$ for the emergent cylinder experiments (E1 and E2).

ing in a power spectrum having a $-5/3$ slope (e.g., Pope, 2000). In fact, the region of $-5/3$ slope, called the 'inertial subrange' is often observed even when the assumptions behind Kolmogorov's theory are violated. Observation of the $-5/3$ region in a particular flow is taken as strong evidence of turbulence, and the length scale representing the beginning of the $-5/3$ region is taken to be the same order of magnitude as the scale at which energy is injected into the flow. While vegetated flows violate the assumption of isotropic turbulence, and our Reynolds numbers are not so high that viscous effects are negligible in the momentum equation, we do observe the $-5/3$ region in all of our flows, confirming the presence of turbulence and providing insight into the scale(s) at which it is generated. In the emergent cases, a $-5/3$ slope is observed at frequencies higher than the Strouhal frequency, $0.2U_0/d$, indicating that TKE is generated at a single length scale in the wakes of the cylinders. For experiment S1 (the submerged case with $d = 0.32$ cm and $h = 29.6$ cm), a $-5/3$ slope is observed at frequencies higher than $0.4U_h/h$, suggesting that energy is injected into the flow through the shear instability that forms at the canopy top. Additionally, a bump above the $-5/3$ slope is visible at the cylinder Strouhal frequency within the canopy, indicating that both SKE and WKE make important contributions to TKE. For experiment S2 (the submerged case with $d = 2.54$ cm and $h = 29.6$ cm), the

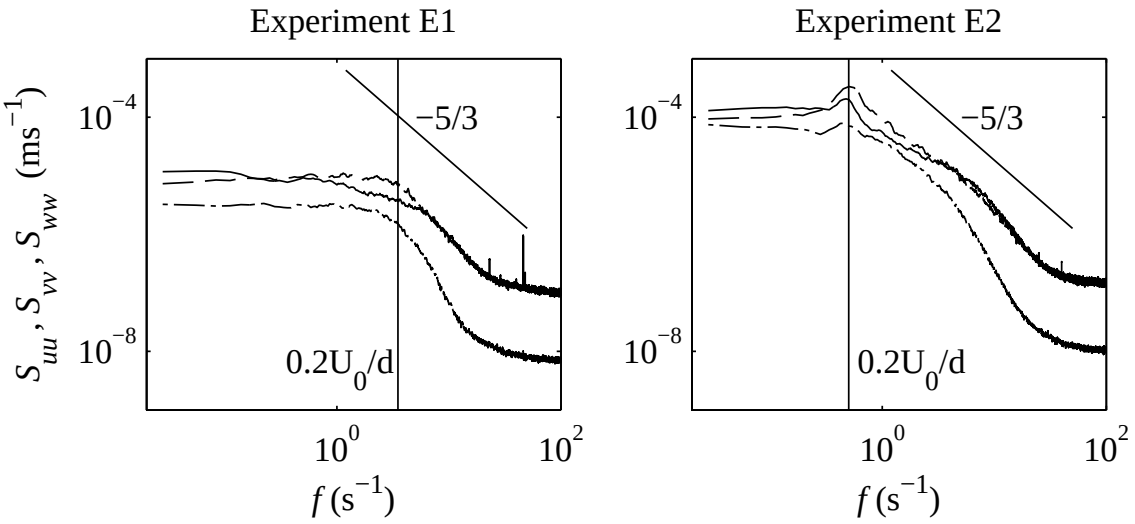

Figure 2.7: Power spectra for the emergent canopy experiments, E1 and E2: S_{uu} (solid line), S_{vv} (dashed line), and S_{ww} (dash/dotted line). These spectra are computed from measurements taken at $z/H = 0.48$. A line having $-5/3$ slope and a vertical line at the cylinder Strouhal frequency, $0.2U_0/d$, are plotted as well.

cylinder height and cylinder diameter are close enough in scale that it is not possible to distinguish a distinct bump at the Strouhal frequency, though this does not exclude the possibility that TKE is generated in the cylinder wakes as well as the shear layer.

Vertical profiles of mean velocity, Reynolds stress, and TKE are plotted in figures 2.9 and 2.10 for the emergent and submerged cases, respectively. In the emergent cases, vertical gradients and Reynolds stress are negligible, as predicted for dense emergent canopies (note that $C_D aH/(1-\phi) > 0.1$ for both E1 and E2), and the profiles of $k/U_0^2(1-\phi)^{2/3}(1/2C_{Dp}ad)^{-2/3}$ collapse to a constant, in agreement with equation 2.30. In the submerged cases, we find very similar velocity and Reynolds stress profiles for S1 and S2, but the TKE level differs by an order of magnitude between S1 and S2 within the canopy.

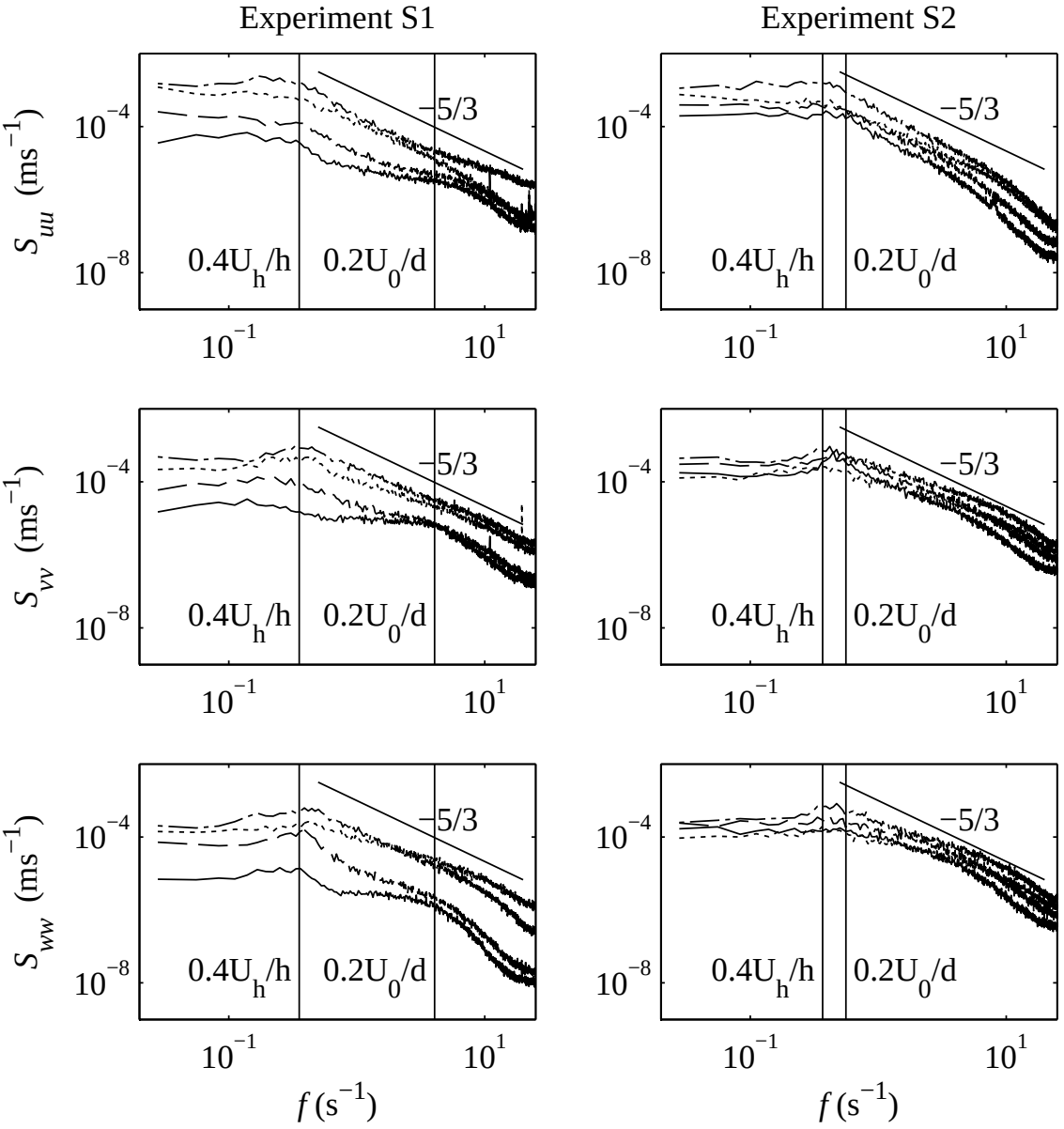

Figure 2.8: Power spectra for the submerged canopy experiments. For experiment S1, spectra are plotted at elevations $z/h = 0.25$ (solid line), $z/h = 0.61$ (dashed line), $z/h = 1.02$ (dash/dotted line), and $z/h = 1.37$ (dotted line). For experiment S2, spectra are plotted at elevations $z/h = 0.20$ (solid line), $z/h = 0.61$ (dashed line), $z/h = 1.02$ (dash/dotted line), and $z/h = 1.37$ (dotted line). A line having $-5/3$ slope and vertical lines at the cylinder Strouhal frequency, $0.2U_0/d$, and at the frequency $0.4U_h/h$ are plotted as well.

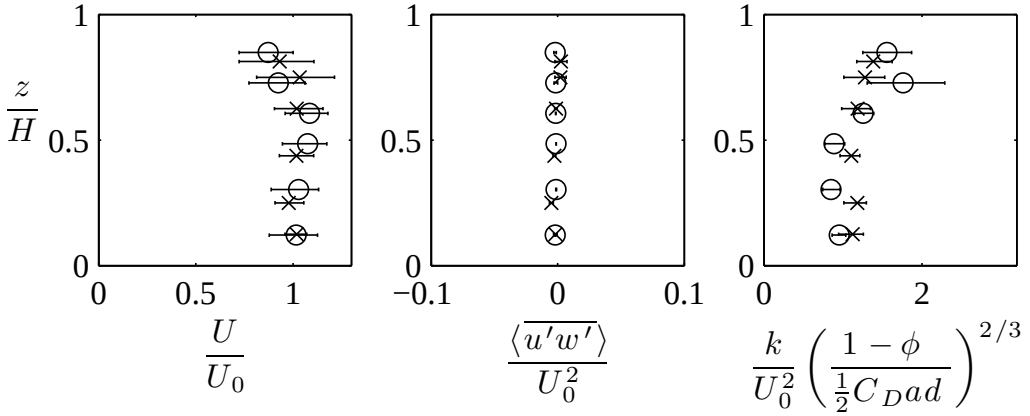

Figure 2.9: Vertical profiles of mean velocity, Reynolds stress, and TKE measured in the emergent canopy experiments E1 (∘) and E2 (×). Error bars indicate 95% confidence intervals obtained from the bootstrap mean of measurements from 7 lateral locations. In some cases, error bars are smaller than the diameter of the symbol for the corresponding data point.

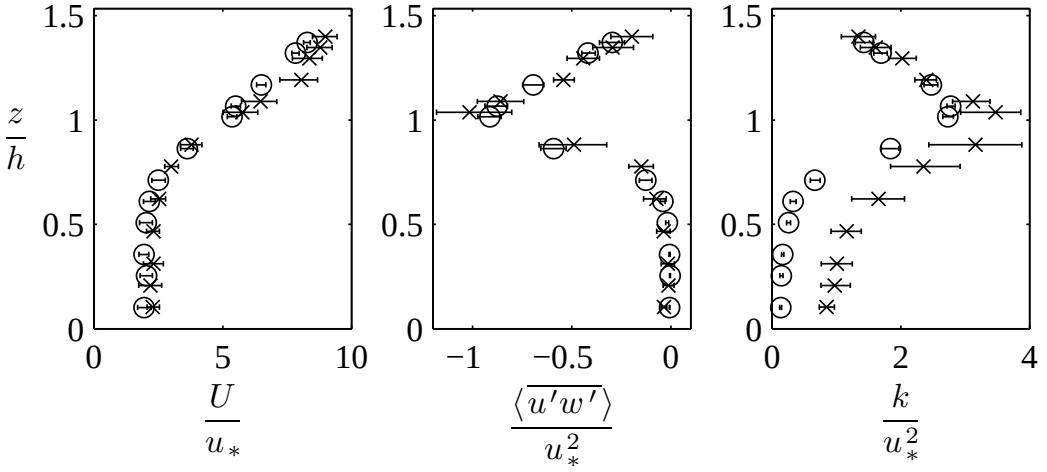

Figure 2.10: Vertical profiles of mean velocity, Reynolds stress, and TKE measured in the submerged canopy experiments S1 (∘) and S2 (×). Error bars indicate 95% confidence intervals obtained from the bootstrap mean of measurements from 7 lateral locations. In some cases, error bars are smaller than the diameter of the symbol for the corresponding data point.

2.5.2 University of Illinois Experiments

A complete description of the University of Illinois experiments may be found in Dunn et al. (1996). These experiments were carried out in a tilting flume that was 19.5 m long, 0.91 m wide, and 0.61 m deep. Plants were modeled using rigid wooden dowels having diameter $d = 0.635$ cm ($1/4$ in). The tops of the cylinders were at height $h = 11.8$ cm above the bed. Cylinders were not randomly distributed but arranged in the staggered patterns illustrated in figure 4.3 of Dunn et al. (1996). In all cases, the cylinders were submerged. The experiments were conducted under steady uniform flow conditions at very high Reynolds number (based on the depth average velocity and the cylinder diameter, above $55,000$ for all experiments). Velocity profiles were measured using an ADV in a downward-looking orientation. For each experiment, velocity profiles were measured at four points in the horizontal plane chosen to capture the variability in the flow field due to the presence of the cylinders. Bed slope was measured directly, but where Reynolds stress measurements above the canopy top are available, we used estimates of S based on a linear least squares fit to the Reynolds stress profile as described in Section 2.5.1 for the Cornell University submerged experiments. Following López and García (2001), we used a drag coefficient of $C_D = 1.13$ for all the experiments. Since the experiments were conducted at high Reynolds number, we assume that $C_{D\nu} = 0$ and $C_{Dp} = C_D$.

The dimensionless parameters governing the flow in the Illinois experiments are reported in table 2.3. Reynolds number and bed slope are reported in table 5.3 of Dunn et al. (1996). Profiles of U, $\langle\overline{u'w'}\rangle$, and the velocity variances $\langle\overline{u'^2}\rangle$, $\langle\overline{v'^2}\rangle$, and $\langle\overline{w'^2}\rangle$ that make up the TKE $k = 1/2(\langle\overline{u'^2}\rangle + \langle\overline{v'^2}\rangle + \langle\overline{w'^2}\rangle)$ were obtained from Appendix B of Dunn et al. (1996).

Experiment	H/h	$C_D ah/(1-\phi)$	$C_{Dp} ad/(1-\phi)$
1	2.85	0.146	0.0079
2	1.95	0.146	0.0079
3	1.40	0.146	0.0079
4	2.35	0.146	0.0079
5	1.73	0.146	0.0079
6	2.27	0.036	0.0020
7	1.56	0.036	0.0020
8	3.33	0.331	0.0179
9	1.82	0.331	0.0179
10	2.26	0.331	0.0179
11	2.65	0.082	0.0044
12	1.98	0.082	0.0044

Table 2.3: Dimensionless parameters for the University of Illinois (Dunn et al., 1996) experiments.

2.6 Model Calibration

The new model we introduced in Section 2.4 includes five empirical coefficients (in addition to the standard k–ε model coefficients): β_p, β_d, $C_{\varepsilon 5}$, $C_{\varepsilon D}$, and C_λ. Scaling arguments suggest that β_p, β_d, and $C_{\varepsilon 5}$ are order one, and β_p cannot exceed 1 because it is an energy conversion efficiency. $C_{\varepsilon D}$ is determined by β_p and γ according to equation 2.46, so there are four degrees of freedom in our calibration. We use the directly measured value $\gamma = 1.21$ from Tanino and Nepf (2008b).

We calibrated the model using the two submerged Cornell University experiments (S1 and S2). The model was executed for each experiment with coefficient β_p varied between

β_p	β_d	$C_{\varepsilon 5}$	$C_{\varepsilon D}$	C_λ
0.2	0.8	0.0	0.15	0.014

Table 2.4: Model parameters that yield the best fit (in the least square sense) to the Cornell University data.

0 and 1 with a resolution of 0.1, coefficients β_d and $C_{\varepsilon 5}$ varied between 0 and 3 with a resolution of 0.1, and the coefficient C_λ varied between 0 and 0.3 with a resolution of 0.001 to obtain a best fit in the least square sense. Mean square error (model vs. data) was equally weighted for experiments S1 and S2 and for U, $\langle\overline{u'w'}\rangle$ and k. The mean square error for each vertical profile was normalized by the variance of the data to capture the fraction of the variability explained by the model.

The coefficients giving the best fit to the Cornell University data are reported in table 2.4. β_p, β_d, and $C_{\varepsilon D}$ are all within an order of magnitude of one, confirming the scaling arguments inherent in the model. C_λ is an order of magnitude smaller than C_μ, suggesting that wake-scale turbulence contributes less to vertical mixing than turbulence generated by vertical shear. Surprisingly, $C_{\varepsilon 5} = 0$, suggesting that the rate at which shear-scale turbulence is dissipated through the energy cascade is independent of the rate at which it is lost to wake-scale turbulence via form drag.

A sensitivity analysis was performed in which β_p, β_d, $C_{\varepsilon 5}$ and C_λ were varied one at a time about their optimal values, and the resulting mean square errors (normalized by the data variance) are plotted in figure 2.11.

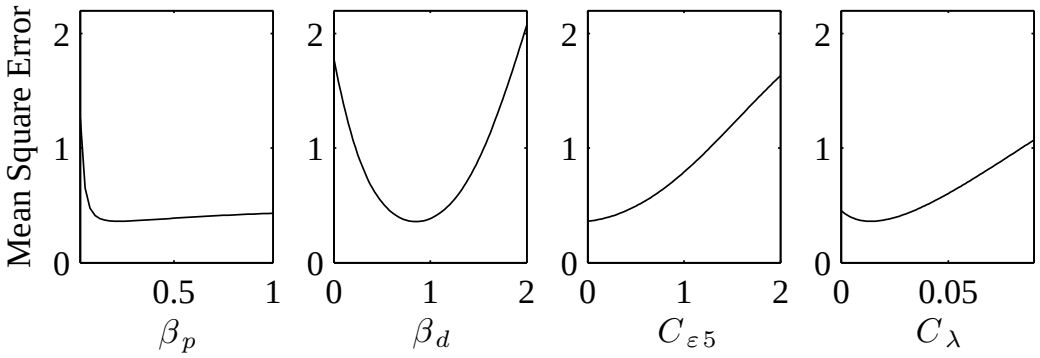

Figure 2.11: Sensitivity of the mean square error (model vs. data from S1 and S2) to the model coefficients.

2.7 Model Performance and Validation

The performance of the new model was compared to the performance of the k–ε models described in López and García (2001), which we will call the 'López–García model', and in Katul et al. (2004), which we will call the 'Katul model'. Both of these models include only one length scale of TKE and dissipation. The López–García model may be obtained from our model by summing the SKE and WKE equations, neglecting the effects of WKE on eddy viscosity, and neglecting the effects of W on dissipation, although the López–García model coefficients are different from ours. The Katul model is based on the assumption that WKE is quickly dissipated and thus negligible. Under this assumption, the model includes the conversion of SKE to WKE, W, as a sink of TKE. However, the Katul model also includes production of WKE, P_w, as a source of TKE, which seems to violate the assumption that WKE is negligible. These two models are discussed in further detail in Appendices A.1 and A.2. Identical discretizations, boundary conditions, and convergence criteria were used for all three models.

The advantages of the new model are most striking for the emergent cylinder experi-

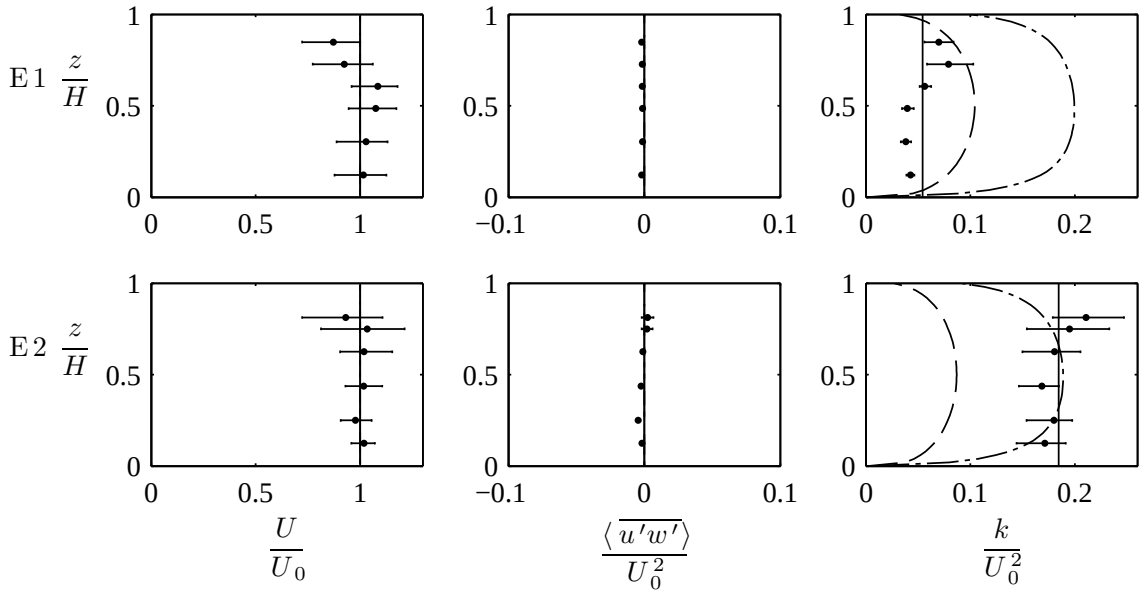

Figure 2.12: Model predictions compared to the Cornell University emergent cylinder data. Experimental data (•) are plotted with error bars representing the 95% confidence interval. Results from the new model are plotted with a solid line, results from the López–García model are plotted with a dashed line, and results from the Katul model are plotted with a dashed/dotted line. For U/U_0 and $\langle \overline{u'w'} \rangle / U_0^2$, all three models give identical results, so only the solid line is visible

ments (E1 and E2). The results for the three models are plotted along with the experimental data in figure 2.12, and the mean square errors are reported in table 2.5. While all three models accurately predict U and $\langle \overline{u'w'} \rangle$, only the new model predicts the dependence of k on $C_D a d/(1-\phi)$. The López–García and Katul models predict vertical gradients in k while the new model correctly predicts uniform k across the water depth. Note that the López–García model results are dependent on the convergence criterion, i.e., the model fails to converge in the emergent case (the López–García model has no convergence problems in the submerged case, for which it was developed).

As in the emergent cases, the advantages of the new model are most clear for k in the

submerged cylinder experiments (S1 and S2). The results for the three models are plotted along with the experimental data in figure 2.13, and the mean square errors are reported in table 2.5. Again, the absence of the parameter $C_D ad/(1-\phi)$ from the López–García and Katul models results in their inability to predict the dependence of k on the cylinder diameter as it is varied between experiments S1 and S2; the new model, in contrast, captures the k profiles quite accurately. The new model is comparable to the López–García model and superior to the Katul model in capturing the U and $\langle\overline{u'w'}\rangle$ profiles.

The new model, along with the coefficients found by calibration against the Cornell University experiments, was validated against the twelve submerged cylinder experiments reported in Dunn et al. (1996). The López–García and Katul models were tested against this same data for comparsion. The results are plotted in figures 2.14 and 2.15, and mean square errors (model vs. data) are reported in tables 2.6 and 2.7. The new model is clearly superior to the other two models, especially in prediction of k, but also in prediction of U. The López–García model makes slightly better predictions of $\langle\overline{u'w'}\rangle$, but all three models predict this quantity quite well. Note that in the few cases where the new model underperforms (Experiments 2, 8, 12), there is either evidence that the flow was not fully developed (see the concave $\langle\overline{u'w'}\rangle$ profile in experiments 2 and 8) or no data above the plant canopy, and thus grounds for suspicion that the flow may not have been fully developed (Experiment 12).

2.8 Conclusions

We have developed the first model for flow through vegetation (aquatic or terrestrial) to handle all of the energy pathways laid out by Shaw and Seginer (1985) as illustrated in

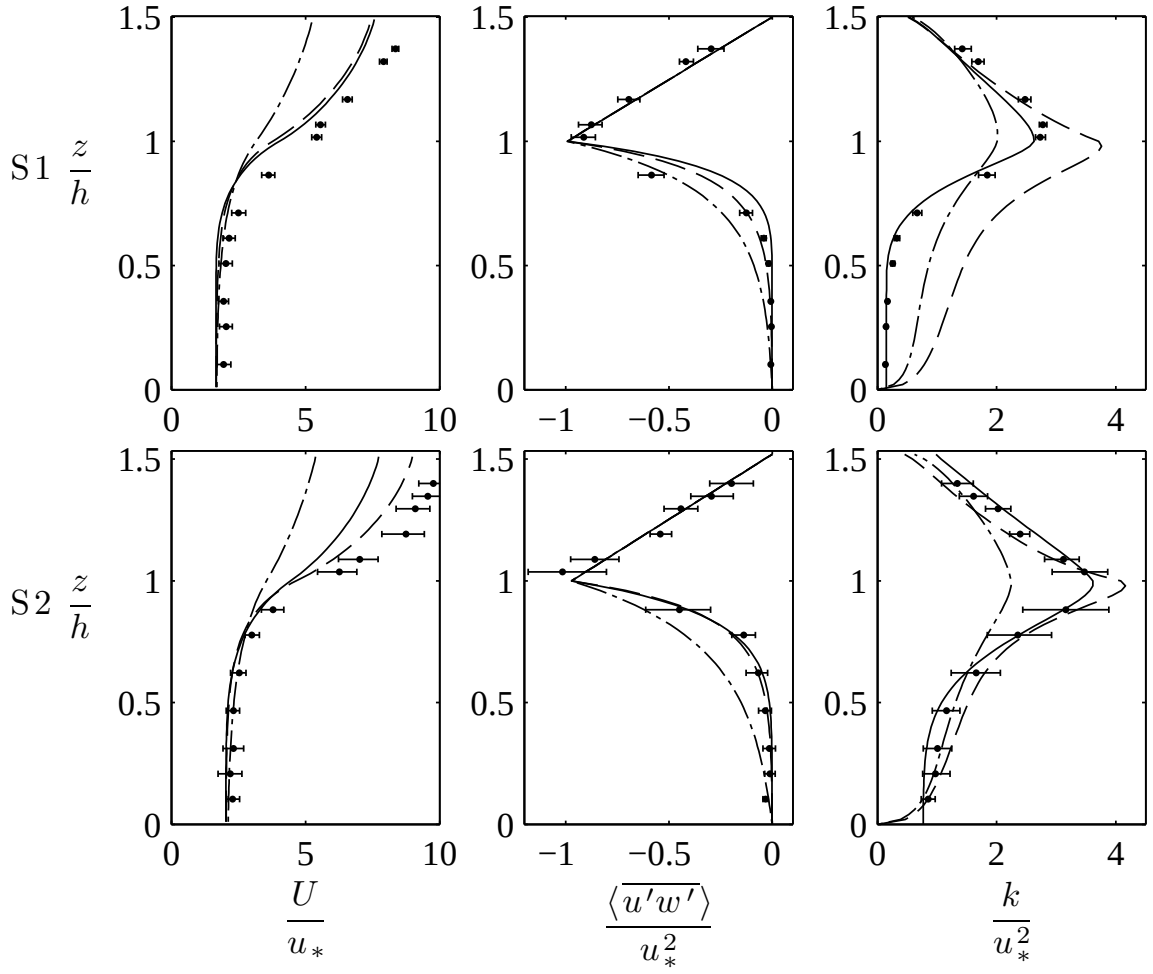

Figure 2.13: Model predictions compared to the Cornell University submerged cylinder data. Experimental data (•) are plotted with error bars representing the 95% confidence interval. Results from the new model are plotted with a solid line, results from the López–García model are plotted with a dashed line, and results from the Katul model are plotted with a dashed/dotted line.

Experiment	quantity	López–García model	Katul model	new model
E1	U	0.04	0.04	0.04
	$\langle\overline{u'w'}\rangle$	–	–	–
	k	7.88	37.13	0.50
E2	U	0.01	0.01	0.01
	$\langle\overline{u'w'}\rangle$	–	–	–
	k	2.05	0.08	0.04
S1	U	0.13	0.57	0.10
	$\langle\overline{u'w'}\rangle$	0.05	0.04	0.09
	k	0.78	0.29	0.04
S2	U	0.08	0.80	0.23
	$\langle\overline{u'w'}\rangle$	0.02	0.13	0.02
	k	0.06	0.46	0.03
Average (E1&E2)	U	0.02	0.02	0.02
	$\langle\overline{u'w'}\rangle$	–	–	–
	k	4.97	18.60	0.27
Average (S1&S2)	U	0.10	0.68	0.16
	$\langle\overline{u'w'}\rangle$	0.03	0.08	0.06
	k	0.42	0.37	0.03

Table 2.5: Mean square errors (model vs. measured data) for the Cornell University experiments. For the emergent experiments (E1 and E2), each mean square error is normalized by the squared mean of the measured vertical profile; for the submerged experiments (S1 and S2), each mean square error is normalized by the variance of the measured vertical profile.

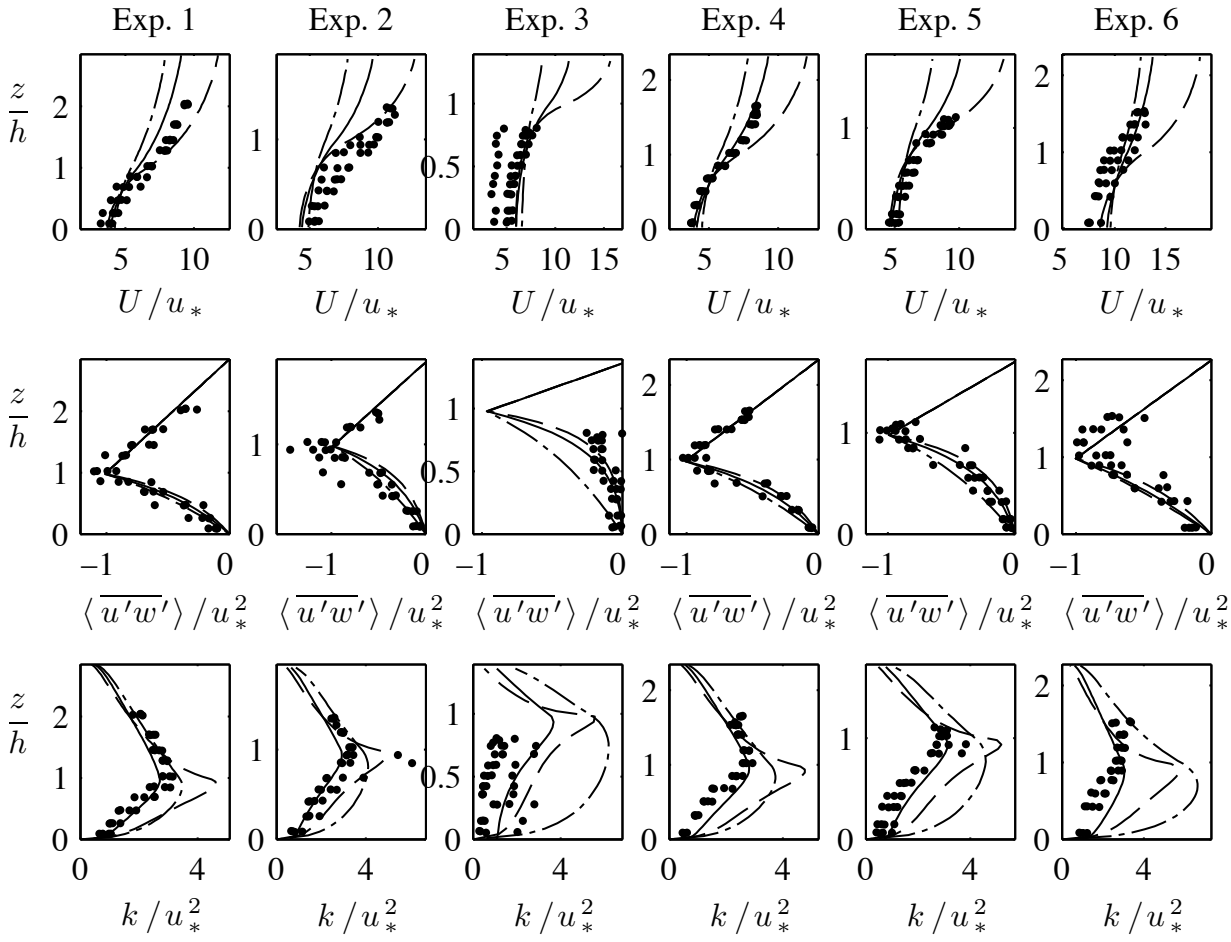

Figure 2.14: Model predictions compared to the University of Illinois experiments $1-6$. Experimental data (•) are plotted at all four lateral measurement locations at each elevation. Results from the new model are plotted with a solid line, results from the López–García model are plotted with a dashed line, and results from the Katul model are plotted with a dashed/dotted line.

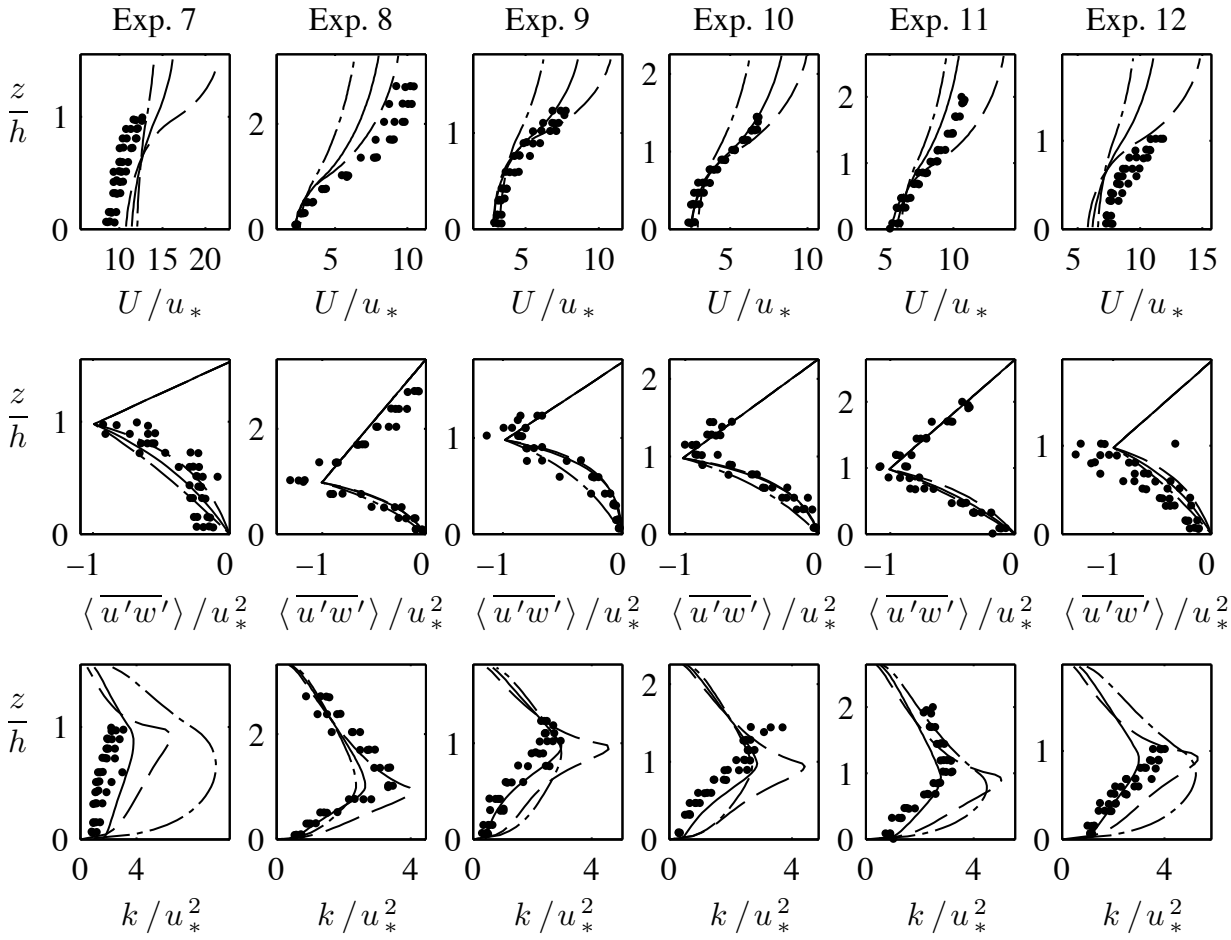

Figure 2.15: Model predictions compared to the University of Illinois experiments $7 - 12$. Experimental data (•) are plotted at all four lateral measurement locations at each elevation. Results from the new model are plotted with a solid line, results from the López–García model are plotted with a dashed line, and results from the Katul model are plotted with a dashed/dotted line.

Experiment	quantity	López–García model	Katul model	new model
1	U	0.11	0.51	0.19
	$\langle\overline{u'w'}\rangle$	0.16	0.10	0.12
	k	2.31	1.24	0.22
2	U	0.50	1.65	0.98
	$\langle\overline{u'w'}\rangle$	0.45	0.23	0.33
	k	0.76	1.20	0.49
3	U	1.42	2.05	1.63
	$\langle\overline{u'w'}\rangle$	1.77	8.57	2.91
	k	7.16	36.48	2.98
4	U	0.43	0.35	0.04
	$\langle\overline{u'w'}\rangle$	0.09	0.08	0.06
	k	3.31	2.74	0.38
5	U	0.15	0.74	0.25
	$\langle\overline{u'w'}\rangle$	0.10	0.11	0.07
	k	2.18	4.43	0.23
6	U	2.33	0.48	0.46
	$\langle\overline{u'w'}\rangle$	0.25	0.32	0.29
	k	8.38	20.07	1.00
7	U	4.90	4.07	4.03
	$\langle\overline{u'w'}\rangle$	0.37	0.86	0.55
	k	26.02	123.69	5.76

Table 2.6: Mean square errors (model vs. measured data) for the University of Illinois experiments $1-7$, each normalized by the variance of the measured vertical profile.

Experiment	quantity	López–García model	Katul model	new model
8	U	0.17	0.94	0.41
	$\langle\overline{u'w'}\rangle$	0.18	0.14	0.17
	k	0.66	0.39	0.23
9	U	0.16	0.59	0.12
	$\langle\overline{u'w'}\rangle$	0.12	0.10	0.10
	k	1.81	1.15	0.19
10	U	0.10	0.41	0.02
	$\langle\overline{u'w'}\rangle$	0.07	0.13	0.07
	k	2.41	0.83	0.40
11	U	0.38	0.49	0.19
	$\langle\overline{u'w'}\rangle$	0.20	0.09	0.11
	k	3.62	4.42	0.41
12	U	1.55	2.23	1.84
	$\langle\overline{u'w'}\rangle$	0.76	0.40	0.53
	k	1.74	5.19	0.23
Average	U	1.02	1.21	0.92
	$\langle\overline{u'w'}\rangle$	0.38	0.93	0.66
	k	5.03	16.82	1.02

Table 2.7: Mean square errors (model vs. measured data) for the University of Illinois experiments $8-12$, each normalized by the variance of the measured vertical profile. In the final row is the average normalized mean square error for experiments $1-12$.

figure 2.4. The model is of the k–ε type, predicting vertical mixing, and may be easily incorporated into larger two-dimensional or three-dimensional hydrodynamic codes.

Previously developed RANS models have accounted for turbulence production at the scale of vertical shear and at the scale of plant stems, but have not allowed for different pathways of dissipation for these two scales of turbulence, such that d is not featured anywhere in these models. This results in complete failure in the case of emergent vegetation, where stem-scale turbulence dominates, and in a failure to predict the strong dependence of TKE on d observed in the laboratory in the submerged case.

Our model was designed to collapse properly to the algebraic solutions for U, $\langle\overline{u'w'}\rangle$ and k in the well-studied case of dense emergent rigid cylinders and calibrated to predict the dependence of k on d observed in the laboratory, which it does quite well. Our model also outperforms the López–García and Katul models, which do not include the d scale, in predicting U and k in laboratory data from submerged cylinders published by Dunn et al. (1996).

The two major advantages of our model are its ability to transition smoothly between emergent and submerged cases, essential in flows driven by tides or seiches (e.g., Rueda and Cowen, 2005a,b), and its applicability in the case of leafy emergent aquatic vegetation, in which turbulence generated by vertical shear and turbulence generated in the wakes of plant stems can be equally important. The model's superior performance in the case of submerged cylinder canopies suggests that inclusion of stem-scale turbulent dissipation may improve predictions of velocity and TKE profiles even in deeply submerged or terrestrial canopies (of plants or of buildings).

Real aquatic plants exhibit high vertical heterogeneity in $a(z)$ (see, for example, figure 2.2), and in many cases their stems bend and their leaves fold with increasing flow rates

such that a is reduced and drag coefficients may change. It is straightforward to incorporate vertical variations in a and Reynolds number dependence of $a(z)$, C_{Dp}, and $C_{D\nu}$ into our model. However, careful characterization of the Reynolds number dependence of $a(z)$, C_{Dp}, and $C_{D\nu}$ must first be performed in a laboratory (or possibly field) setting. Future work will focus on testing of the new model against data from live canopies of Eurasian watermilfoil.

CHAPTER 3

MEASURING RESIDENCE TIME IN NON-IDEAL SURFACE WATER SYSTEMS

3.1 Introduction

Mean hydraulic residence time (HRT), the average amount of time that a water parcel remains in an aquatic system, is a key variable determining ecosystem dynamics in estuaries, lakes, and wetlands. Chemical engineers pioneered the concept of residence time, and in many standard chemical engineering text books (e.g., Levenspiel, 1999; Folger, 1992), one will find along with the definition of HRT, methods of measuring HRT and simple models to predict HRT in chemical reactors. A standard method for measuring HRT is the passive tracer pulse release study, in which a known mass of neutrally buoyant tracer (often a fluorescent dye) is released all at once into the system, and the flux of that tracer out of the system is continuously monitored at all outlets, ideally until all of the tracer mass has exited the system. The first moment of this dye flux curve, normalized by the initial tracer mass, is the mean HRT. This pulse release method was first proposed by Danckwertz (1953) for application to chemical reactors.

Since natural aquatic systems such as lakes and rivers can be thought of as chemical reactors, the field of environmental fluid mechanics adopted the tools developed by chemical engineers to characterize HRT, and have pioneered techniques for estimating HRT in circumstances unique to natural aquatic systems. Kadlec (1994) reviewed the concepts of residence time and the pulse release method in the context of natural surface water systems, and Werner and Kadlec (1996) developed a method for comparing dye flux curves measured under nonsteady flow conditions common in natural systems. In this chapter, we present some methods that are useful in dye pulse release studies aimed

at measuring HRT in surface water systems. These methods are based on our experience conducting two such studies in an embayment called Sterling Pond (SP).

3.1.1 Study Site

Sterling Pond (SP) is a small and shallow freshwater embayment located in Fair Haven, New York, a small town on the southern shore of Lake Ontario (LO). SP drains Sterling Creek (SC), its bordering wetlands, and a large watershed ($210\,\mathrm{km}^2$) into LO through a long, narrow, and shallow manmade channel ($100\,\mathrm{m} \times 17\,\mathrm{m} \times 3\,\mathrm{m}$) – a bathymetric map of SP is provided in figure 3.1. From late spring through early fall, SP is home to diverse populations of submerged aquatic vegetation, which undergo one or more periods of dense growth. In order to characterize the residence time scales of SP, we conducted two dye release studies.

3.1.2 Methods Overview

The first challenge we address is accurately measuring the tracer flux out of the system. The two components of tracer flux are concentration and flow rate. We recommend methods for keeping a flow-through fluorometer well-calibrated throughout a long dye study, and we present an approach for post-calibrating the fluorometer when particulate matter has built up inside the flow cell. We compare methods of measuring flow rate through a narrow and shallow channel in which the mean flow is not quasi-steady and both horizontal and vertical boundary layers are significant, examining the sensitivity of outflow measurements and mean HRT to the details of the horizontal and vertical boundary lay-

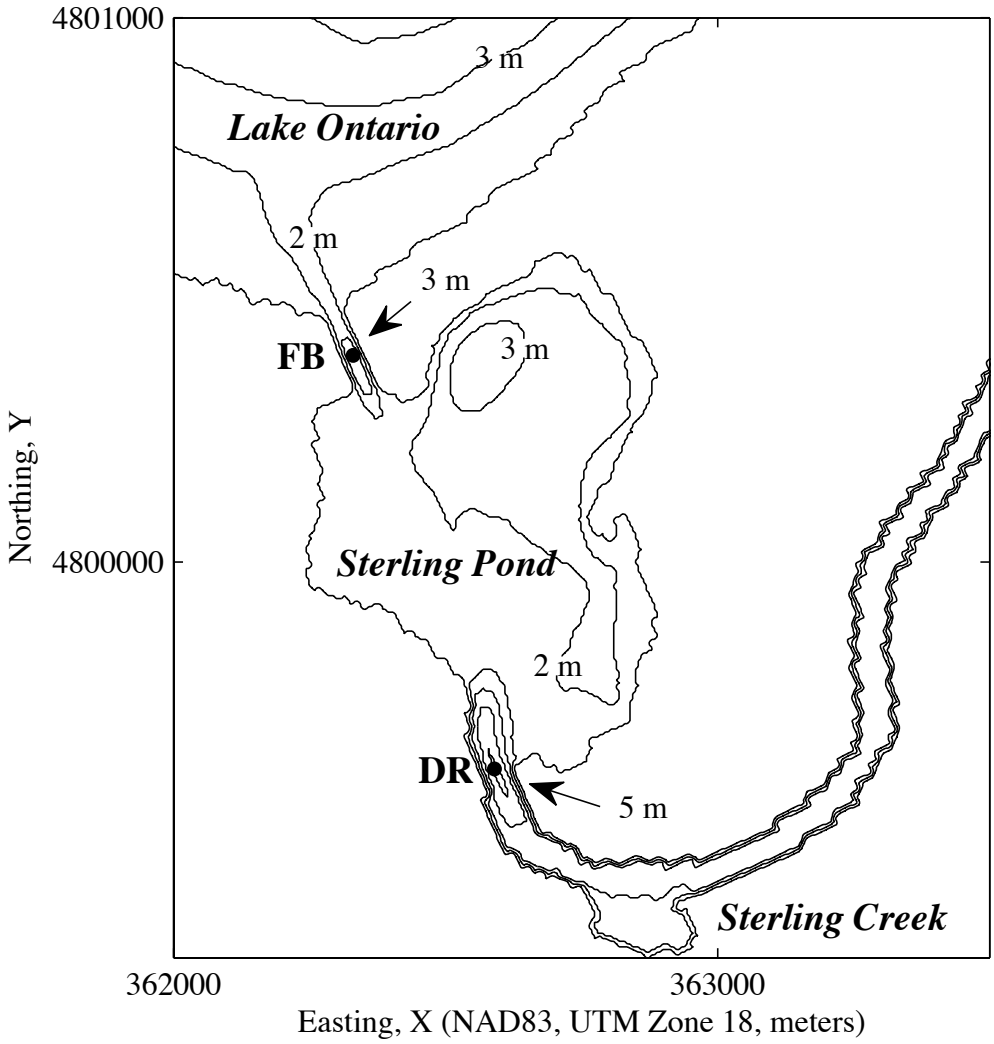

Figure 3.1: Bathymetry of Sterling Pond and equipment locations.

ers in the outlet channel.

Since one of our two tracer studies was long enough in duration that decay of the tracer with sunlight was significant, as is often the case in tracer studies employing fluorescent dyes, it was necessary to correct for photolytic decay. We propose a method for estimating the flux and mean HRT of a hypothetical conservative tracer from the mea-

sured flux of a photolytic tracer. Sorption of the tracer onto sediments, plants, and detritus is another pathway of potential loss. Sorption properties vary widely across tracers and sediment types. We review the literature on sorption of one particular fluorescent water tracing dye, Rhodamine WT (RWT), in surface and groundwater systems, and conclude that further study is needed in this area, especially in regard to sorption kinetics, before the extent of RWT sorption can be estimated for a field study.

It is rare in tracer release studies that all of the tracer is observed leaving the system. To some extent, this may be due to tracer decay or sorption, but time limitations or equipment failure often cut an experiment short, and in this case the tracer flux curve must be extrapolated, either by analytical or numerical methods, to obtain an estimate of the mean HRT. Often, the system is assumed to behave as a continuously stirred tank reactor (CSTR) towards the end of the study, and the tracer flux is extrapolated with an exponential tail. However, the CSTR model is not appropriate when the system is not fully-mixed. Even when the CSTR model is appropriate, if flow oscillates and/or changes direction over time (e.g., because of surface seiching, an upwelling event, or transitory watershed flow), then fitting an exponential tail is difficult and it is unclear how to implement the standard method of extrapolation. Whatever the extrapolation method, care must be taken that the extrapolated tracer flux curve does not violate conservation of mass. We present two new simple analytical methods of extrapolation, both based on fitting a model to the running first moment of the tracer flux curve, both satisfying the conservation of mass condition, and both robust under unsteady flow conditions. The two methods are based on a CSTR model and a simple transient storage model (TSM), respectively.

Estimation of measurement uncertainty is discussed throughout. All values of uncertainty reported herein represent the 95% confidence interval (equal to 1.96 times the

standard error for a Gaussian error distribution). It is not straightforward to propagate uncertainties from flow rate measurements, concentration measurements, measurements of photolytic decay, and possible sorptive losses to uncertainty in mean HRT. We propose a Monte Carlo approach, which is appropriate for the implicit equations involved in photolysis calculations and for errors that are correlated over finite but nonzero time scales, which often arise in field studies.

3.1.3 Residence Time – Definition and Measurement

For unsteady, inhomogeneous systems, HRT is a function of both time and space (Monsen et al., 2002). Even in a statistically steady and homogeneous turbulent system, the HRT is a stochastic variable – within a water parcel beginning at a given time and location, the individual water molecules will have different residence times, comprising the residence time distribution (RTD). The RTD is a probability distribution having mean, standard deviation, and higher order statistics. Mean HRT tends to be set by the time scales of physical processes driving exchange between a system and its surroundings and the time scales of mixing within the system itself (Rueda and Cowen, 2005b).

Provided that there is no return flow into the system, the RTD at time t and location $\vec{x}$ may be measured directly by releasing an instantaneous pulse of a passive (specific gravity 1), conservative tracer at t and $\vec{x}$ and monitoring the tracer flux out of the system (Danckwertz, 1953; Kadlec, 1994; Hilton et al., 1998). If the system has only one outlet, and if the tracer is well-mixed across that outlet, then the RTD is equal to the normalized flux out of the system, $r(t)$, defined as

$$r(t) \equiv \frac{Q(t)C(t)}{M_0} \tag{3.1}$$

where $Q(t)$ is volumetric flow rate out of the system, $C(t)$ is the concentration of the tracer at the outlet (defined in terms of mass per unit volume), and M_0 is the initial mass of tracer in the system.

If the tracer leaves and then re-enters the system, then $r(t)$ will be negative for some times and will not represent the RTD; however, the first moment of $r(t)$ is equal to the average residence time even when there is return flow (Hilton et al., 1998). The time integral of $r(t)$, defined as

$$R(t) \equiv \int_0^t r(\tau) d\tau \tag{3.2}$$

is the fraction of tracer which no longer remains in the system at time t. In the case of zero return flow, $R(t)$ is equal to the cumulative residence time distribution (CRTD). Note that for a conservative tracer in a system with a single outlet, conservation of mass requires that

$$\lim_{t \to \infty} R(t) = 1 \tag{3.3}$$

unless a portion of the tracer mass remains for all time within the system. For a truly conservative tracer in a system having any sort of outflow (even intermittent) to a much larger system, where the tracer is diluted, we may expect equation 3.3 to hold, provided that we have accurately measured tracer flux through all outlets.

We may also define the running first moment of the RTD,

$$\Theta(t) \equiv \int_0^t r(\tau) \tau d\tau \tag{3.4}$$

such that the mean residence time, T_R, is given by

$$T_R = \lim_{t \to \infty} \Theta(t). \tag{3.5}$$

3.1.4 Properties of Rhodamine WT

Rhodamine WT (RWT) is popular in surface water dye tracing because its emission spectrum overlaps very little with background fluorescence in freshwater systems, its fluorescence is insensitive to pH (above a pH of 5) and varies predictably with temperature, it is relatively non-toxic, and has a low detection limit (Smart and Laidlaw, 1977). RWT is relatively conservative compared to other popular water tracing dyes (e.g., fluorescein), but it does decay slowly with sunlight exposure (over time scales of a week or more), and it is adsorbed to some degree by sediment, detritus, and possibly plants. In this section we review what is known about the non-conservative behavior of RWT.

Suijlen and Buyse (1994) investigated photolysis of RWT in detail, and we summarize their work here. The decay of RWT with sunlight is a first order reaction, following

$$\frac{dM}{dt} = -M(t) \int \epsilon(\lambda)\Phi(\lambda)\frac{dE(\lambda,t)}{d\lambda}d\lambda \tag{3.6}$$

where M is the total mass of RWT, t is time, λ is light wavelength, ϵ is the molar absorptivity (also called the molar extinction coefficient), Φ is the reaction quantum yield, and E is scalar irradiance. The molar absorptivity is the amount of light at a given wavelength absorbed by a solution per unit concentration of the absorbing species and per unit path length of the light. The quantum yield is the number of moles of the reactant (in this case, RWT) disappearing per einstein of light absorbed at a given wavelength. Tai and Rathbun (1988) plot the absorption spectrum for RWT in their figure 1 – there is a strong peak in light absorption at 558 nm with significant absorption occurring in the $510 - 590$ nm range. There is also weak but significant absorption in the $300 - 400$ nm range. Tai and Rathbun (1988) measured a quantum yield of $\Phi = 1.82 \times 10^{-7}$ mol einstein^{-1} for incident light having a wavelength of 546 nm, but were unable to measure any photolytic decay of RWT after 200 hrs of radiation with 313 nm or 366 nm light, concluding that the action

spectrum of RWT is similar to the absorption spectrum.

Suijlen and Buyse (1994) point out that for light with a constant spectral distribution, equation 3.6 can be written

$$\frac{dM}{dt} = -kE_0(t)M(t) \tag{3.7}$$

where E_0 is the total scalar irradiance (having units of $\mathrm{W\,m^{-2}}$), and k is the photolysis constant of RWT. We may note that since only wavelengths of $510 - 590\,\mathrm{nm}$ contribute to photolysis of RWT, equation 3.6 is valid under the weaker condition that the ratio of irradiance in the $510 - 590\,\mathrm{nm}$ range to total scalar irradiance is constant. While the spectral distribution incident on the earth's surface may vary strongly, especially with water content of the atmosphere, there is not a great deal of variation in the vicinity of $558\,\mathrm{nm}$, and while there may be strong dips in spectral irradiance at particular wavelengths corresponding to absorption by atmospheric constituents, it is fairly reasonable to assume that the ratio of irradiance in the $510 - 590\,\mathrm{nm}$ band to total irradiance is constant. Thus, we adopt equation 3.6. Suijlen and Buyse (1994) measured $k = (3.5 \pm 0.3) \times 10^{-9}\,\mathrm{m^2\,J^{-1}}$ in natural sunlight in the Netherlands. Note that the value of scalar irradiance important to decay of RWT is the value at the site of the RWT in the water, not the value measured at the surface at a meteorological station. We discuss the problem of estimating E_0 in the water column from typical radiation measurements from meteorological stations in Section 3.2.2.

Sorption of RWT is a big problem in groundwater tracer studies, and less so in surface water systems, but significant losses of RWT, likely due to sorption, have been observed in a stream with a highly permeable gravel bed (Bencala et al., 1983), in constructed wetlands (Lin et al., 2003; Keefe et al., 2004), and in wetland mesocosms (Dierberg and DeBusk, 2005).

Tracer grade rhodamine WT contains two fluorescent molecules in a $50/50$ mass ratio, having slightly different excitation and emission spectra and different sorptive behavior (Vasudevan et al., 2001; Sutton et al., 2001). The two fluorescent molecules are structural isomers, differing in the placement of a single carboxylate (-COOH) group (Vasudevan et al., 2001). Because the isomers have slightly different fluorescent properties, separation due to differential sorption can result in concentration measurement errors. Sutton et al. (2001) determined that a Turner Designs 10-AU fluorometer, calibrated with a RWT solution containing the isomers in a 50/50 ratio, will report concentrations that are 7.8% low for a solution that is 100% isomer 1 and concentraitons that are 7.8% high for a solution that is 100% isomer 2.

Vasudevan et al. (2001) hypothesize and confirm that mechanisms of RWT sorption include hydrophobic exclusion from aqueous solution, electrostatic attraction to oppositely charged surfaces or surface sites, and complexation of the -COOH group with surface-bound aluminum and iron, finding that because of the placement of the -COOH group, all of these processes are enhanced for isomer 2, resulting in stronger sorption of this isomer on a wide variety of substrates (cleaned sand, iron oxide coated sand, humic acid coated sand, aluminum oxide, and iron oxide). Because sorption processes are similar for the two isomers, they may compete for sorption sites, possibly resulting in greater sorption of isomer 1 in the absence of isomer 2. Vasudevan et al. (2001) also find that increasing pH between 4 and 8 decreases sorption on all of the substrates investigated.

There are two main types of laboratory sorption studies: batch and column. In a batch study, an initial concentration C_0 of RWT or one of its isomers is shaken in a bottle with a substrate-water solution of density R_S (mass substrate per volume of water). The concentration of RWT in solution (C, mass per unit volume) and the concentration of RWT that is sorbed (q, mass RWT per unit mass substrate) may be monitored in time

or simply reported at equilibrium (C_E and q_E, respectively). The partition coefficient, K_p, is defined as the ratio of sorbed to dissolved RWT mass at equilibrium, i.e., $K_p \equiv q_E/C_E$. K_p has units of volume over mass. The relationship between q_E and C_E is called the sorption isotherm. K_p may be a function of concentration, but is typically constant for RWT concentrations below 100 ppb (parts per billion), i.e., the sorption isotherm is typically linear for RWT concentrations below 100 ppb.

In a column study, a column of soil is loaded with a pulse or step of RWT and the outlet concentration is monitored over time. There are a variety of methods for estimating K_p as well as kinetic parameters from column studies, all employing models of advection and dispersion as well as sorption (e.g., Sutton et al., 2001). Soerens and Sabatini (1996) demonstrate that since RWT is a compound of two isomers having different soprtion behavior, K_p of RWT measured in batch studies is a function of R_S; for a 50/50 solution, as R_S approaches zero, K_p approaches the arithmetic mean of the individual K_p of the constituent isomers, and as R_S approaches infinity, K_p approaches the geometric mean of the individual K_p of the constituent isomers.

From batch studies, for isomer 1, Vasudevan et al. (2001) find K_p in the range of $20 - 56\,\text{mL}\,\text{g}^{-1}$ for iron and aluminum oxide, and they find that isomer 1 is not absorbed by cleaned sand, iron oxide coated sand, or humic acid coated sand; for isomer 2, they find K_p in the range of $130 - 450\,\text{mL}\,\text{g}^{-1}$ for iron and aluminum oxide, $0.18\,\text{mL}\,\text{g}^{-1}$ for cleaned sand, and $0.9\,\text{mL}\,\text{g}^{-1}$ for iron oxide and humic acid coated sand (the isotherm becomes nonlinear for humic acid coated sand, but only at extremely high concentrations, over 1 ppm, parts per million). Sutton et al. (2001) present significantly different results from batch studies, finding $K_p = 0.198\,\text{mL}\,\text{g}^{-1}$ for isomer 1 and cleaned sand and $K_p \approx 1\,\text{mL}\,\text{g}^{-1}$ for isomer 2 and cleaned sand in the 'low' concentration range (below 330 ppb). Column study results from Kasnavia et al. (1999) seem to contradict the find-

ings of both Sutton et al. (2001) and Vasudevan et al. (2001): a two-step breakthrough curve was observed for RWT with alumina (aluminum oxide) but not with silica (sand), suggesting that differential sorption is insignificant in sand. The results may be due to kinetic effects, which are not discussed in the paper. Shiau et al. (1993) find that in a soil that is 72% sand, 22% silt, and 6% clay, $K_p = 5.0\,\text{mL}\,\text{g}^{-1}$ for isomer 1 and $K_p = 107\,\text{mL}\,\text{g}^{-1}$ for isomer 2; and in a soil that is 91% sand and 9% silt, $K_p = 3.3\,\text{mL}\,\text{g}^{-1}$ for isomer 1 and $K_p = 15.5\,\text{mL}\,\text{g}^{-1}$ for isomer 2.

There are no reports of K_p for individual RWT isomers in wetland soils, but Lin et al. (2003) report compound K_p measured in batch studies for RWT sorption onto two soil samples from a constructed wetland and onto plant detritus separated from these soil samples. They report K_p in the range of $6,000 - 15,000\,\text{mL}\,\text{g}^{-1}$, but we suspect from examination of their figure 7 that they have committed a unit conversion error or have perhaps omitted the density of water from a calculation, and that values should be in the vicinity of $K_p = 10\,\text{mL}\,\text{g}^{-1}$ for sorption to sediment (both 1:5 and 1:10 sediment-water ratios) and $K_p = 40\,\text{mL}\,\text{g}^{-1}$ for plant detritus in a 1:100 detritus-water ratio – the details of our analysis of the Lin et al. (2003) data are given in Appendix B. These corrected partition coefficients are comparable to those measured by Sutton et al. (2001), Vasudevan et al. (2001) and others in purified sediments. Keefe et al. (2004) report K_p for RWT sorption on two species of bullrush and sediments from a constructed wetland, but they appear to have obtained these values by fitting a line to a log-log plot and incorrectly reporting the slope as K_p (see their figure 5), and so the reported K_p values are not usable. Using batch studies, Bencala et al. (1983) find composite $K_p = 5.6\,\text{mL}\,\text{g}^{-1}$ for gravel of diameter range $1 - 6.2\,\text{mm}$ with a 1:5 sediment-water ratio, and Sabatini and Austin (1991) find a composite $K_p = 4.5\,\text{mL}\,\text{g}^{-1}$ with a 1:2 sand-water ratio for alluvial aquifer sediment that is 97.3% sand, 2.2% silt and 0.5% clay. Turner et al. (1991) conducted batch studies

of RWT sorption on two species of aquatic plants (Eurasian watermilfoil and hydrilla) and on algae, reporting negligible sorption after four days. The plants were left intact, the initial RWT concentraiton was 10.4 ppb, RWT was applied to the water column (as opposed to the root zone), and the authors do not mention stirring the water.

There have been few studies of RWT sorption kinetics. Sutton et al. (2001) are the only authors to explicitly investigate kinetics in either batch or column studies; they employ both types of study, separately measuring concentrations of isomers 1 and 2 in the batch studies, and using a Turner Designs 10-AU fluorometer to measure total RWT concentration in the column studies. For the substrate, they use sand from a single field site. In the batch studies, they test both untreated sand and sand that has been treated with hydrogen peroxide to remove organic matter; they do not say whether sand in the column studies has been treated. For the batch study, the sampling frequency is too low to resolve the time scale of sorption for isomer 1 and the duration of the experiment is too short to resolve the time scale of sorption for isomer 2 on untreated sand, but Sutton et al. (2001) do observe that 95% sorption is achieved in less than 5 min for isomer 1 on both treated and untreated sand, in $1-2$ hrs for isomer 2 on treated sand, and in greater than 24 hrs for isomer 2 on untreated sand.

Sutton et al. (2001) test kinetic models of increasing complexity on the column data, finding that a model allowing for two sorption sites for each isomer (one in equilibrium and one exhibiting first order kinetics) is the simplest model that provides good fits to all of the data. Fitting parameters include K_p for each isomer, a first-order rate constant k for each isomer, the fraction of each isomer exhibiting equilibrium sorption, the Peclet number, and the fraction in the injected solution that is isomer 1 (note that at the time of this study, the $50/50$ composition of tracer grade RWT had not been definitively established) – there are a total of 8 fitting parameters. For the first two column studies,

of 13 and 20 min duration, respectively, the best fit values of K_p and k were comparable to those found in the batch studies; however, for the final two column studies, of 2.4 and 3.6 hr duration, respectively, the best fit values of K_p and k were quite different from those found in the batch studies. One more glimpse into the kinetics of sorption may be found in figure 5 of Bencala et al. (1983), showing that sorption of RWT onto gravel of diameter range $1 - 6.2$ mm with a 1:5 sediment-water ratio does not quite reach equilibrium within 22 days, and the rate of sorption decreases with decreasing concentration in solution. It is clear that kinetics is on the frontier of RWT sorption research.

Another topic on the frontier is desorption. Smart and Laidlaw (1977) in their seminal review of fluorescent water tracing dyes assert that 'adsorption of dye onto sediment surfaces is mainly irreversible', and this idea has persisted in the literature, but its veracity is far from settled. Trudgill (1987) conducted the first desorption study for RWT: for a soil that is 20% sand, 56% silt, and 24% clay and a 1:2 sediment:water ratio, they first conduct a batch sorption study for RWT, finding a linear isotherm with $K_p = 38\,\mathrm{mL\,g^{-1}}$ (inferred from their table XI). Then they conduct a 'one-step desorption', which we interpret to mean they replace the RWT solution with clean water, and they find that less than 5.3% of the RWT desorbs into solution. They conclude that sorption is almost entirely irreversible, but we interpret this result differently: because RWT in equilibrium partitions strongly to the soil (by a factor 38), we do not expect all of the RWT to be recovered into solution after a single change of water. In Appendix B, we analyze the desorption data of Trudgill (1987), finding that between 35% and 100% of sorption was reversed during the study. Sabatini and Austin (1991) carefully measure total mass recovery of RWT and other fluorescent dyes in a set of column studies, observing that between 85 and 100% of the dye is recovered for every column run, and concluding that dye sorption is reversible. Sutton et al. (2001) use methanol to desorb RWT isomers after batch studies to confirm that there

was no decay, and while they recover all of isomer 1, they note that isomer 2 was difficult to desorb, speculating that multiple methanol treatments might have desorbed isomer 2, but they do not test this. As discussed above, a sorption model including equilibrium and first-order sorption mechanisms (that are completely reversible) provides a satisfactory fit to the column study data of Sutton et al. (2001), but multiple flushes with clean water over the course of 24 days were required to recover all but 10% of the RWT in one column study. Lin et al. (2003) conducted the most recent desorption study. Like Trudgill (1987), they replace the RWT solution from an equilibrated batch with clean water and measure the RWT in solution after re-equilibration. From their calculations, an average of only 10% of the RWT was desorbed, but if we correct for the factor of 1000 in their estimate of K_p, and account for the partitioning expected after a single replacement of RWT solution with clean water, our calculations show that an average of 87% of the RWT that was expected to desorb assuming fully reversible sorption was, in fact, desorbed, suggesting that for these wetland soil and plant detritus samples, sorption of RWT is largely reversible. Details of our analysis of the Lin et al. (2003) data are given in Appendix B.

Many of the studies discussed in this section were conducted in groundwater systems or soil columns designed to simulate groundwater flow. Our concern, however, is the effect of RWT sorption on the measurement of HRT in surface water systems where exposure to sediment is much lower and sorption is less prevalent. Dierberg and DeBusk (2005) assert that dye sorption, even if it is significant in terms of percent dye adsorbed, will not significantly affect measurements of mean HRT in dye release studies provided that the following three criteria are satisfied:

1. There is sufficient dye recovery to see the peak and at least some portion of the tail in $r(t)$, and

2. The sorption process is zero-order (loss is independent of concentration) and irreversible.
3. Mean HRT is estimated by taking the temporal moment of the tracer mass flux and normalizing by the total mass of the tracer recovered (instead of the total mass released).

In light of our literature review above, it is unlikely that the second criterion is satisfied. However, regardless of whether RWT meets this criterion, there is some evidence from both Dierberg and DeBusk (2005) and Lin et al. (2003) that measured mean HRT is, in some cases, insensitive to sorption of RWT in wetland systems.

Lin et al. (2003) conduct a simultaneous RWT and bromide release in a small wetland lasting six days. They estimate mean HRT using each tracer (RWT and bromide) by taking the first temporal moment of the measured tracer flux and normalizing by the recovered mass. They recover 85% of the bromide but only 59% of the RWT, and they find mean HRT's of 55 hrs from the bromide release and 53 hrs from the RWT release, i.e., Lin et al. (2003) find that the difference in the mean HRT estimate introduced by 30% less tracer recovery is less than 4%.

Dierberg and DeBusk (2005) conduct a series of simultaneous RWT and lithium release studies in flow-through mesocosms populated with wetland sediment and submerged aquatic vegetation. Like Lin et al. (2003), they estimate mean HRT using each tracer (RWT and lithium) by taking the first temporal moment of the measured tracer flux and normalizing by the recovered mass. In each of their two 'low' concentration experiments, which are most comparable to our 2003 dye study in SP, 84% of the lithium is recovered, while 43% and 42% of the RWT is recovered in each experiment, respectively. The estimate of mean HRT was 6.9 days in the first experiment and 6.0 days in the second from the

lithium curves and 6.6 days in the first experiment and 4.7 days in the second from the RWT curves. In this case, the difference in the mean HRT estimate introduced by 43% and 42% less mass recovery is 4% and 22%, respectively.

3.2 Materials and Procedures

3.2.1 Dye Flux Measurements

The first dye study was conducted in May of 2002 when SP was characterized by sparse aquatic vegetation, high watershed flow, and little forcing from LO. The second was conducted in September of 2003 when SP was characterized by dense aquatic vegetation, low net flow from the watershed, and strong oscillatory flow between SP and LO (reversing direction on a roughly 10 min time scale). Each dye study began with the release of a plug of 3.79 L (2002) or 7.57 L (2003) of Rhodamine WT (20% by weight solution), diluted in 20 L of SP water, and pumped through a vertical line-source diffuser at site DR (see figure 3.1) over approximately 15 min. In 2002, the dye release commenced at 1:02 P.M. (EDT) on May 15, and in 2003, the dye release commenced at 6:31 P.M. (EDT) on September 18. After the dye release, dye concentration and flow rate were monitored continuously at site FB (see figure 3.1), in the channel connecting SP to LO, in order to quantify the dye flux out of SP and thus estimate the mean HRT.

Dye Concentration

After each dye release, concentration of RWT, $C(t)$, was continuously monitored using a Turner Designs 10-AU flow-through fluorometer with temperature correction package sampling at 1 Hz. The intake of a 1 in-diameter rubber/vinyl hose was positioned at site FB near the middle of the channel at mid-depth. A self-priming centrifugal pump was positioned at the other end of the hose and used to draw water into the 10-AU flow cell. Polyethylene tubing and both brass and acetal couplings were used to connect the pump to the hose, the hose to the 10-AU, and to discharge water from the flow cell. In 2003, all of the polyethylene tubing was covered with opaque tape to shade the flow cell from sunlight, as specified in the 10-AU manual, but in 2002 this step was neglected, and the translucent tubing was left exposed. In 2003, a plastic, cylindrical (10 cm diameter, 15 cm length) 1 mm-mesh filter was screwed onto the intake to prevent plant matter from clogging the pump, but in the short 2002 experiment this step was not necessary. The travel time between the intake and the flow cell of the 10-AU was measured to be 21 s by disconnecting the tubing from the flow cell, measuring the time taken for the pump to fill a 14 L tank to estimate the flow rate, and estimating a delay time equal to the total volume of the tubing divided by the flow rate. The head loss through the flow cell and the short discharge tube were assumed to be small compared to the head loss through the elevation change and the longer lengths of tubing leading to the fluorometer. The delay was subtracted from the recorded times of measurements to synchronize concentration and channel flow rate data. In the following sub-sections, we discuss fluorometer calibration and post-calibration, and considerations of background fluorescence and sunlight bias. In King (2006), we report and discuss estimates of uncertainty in concentration measurements in great detail.

Calibration Calibration was performed using the serial dilution method to obtain accurate concentrations, as follows: the day before each experiment, a calibration solution was mixed in an opaque container (to prevent photolytic decay) from $280\ \mu$L of the 20% RWT source solution (measured with a micropipette) and 200 mL of distilled water. A few hours before each experiment, 14 L of water from the SP channel was placed in a glass tank, and the 10-AU, starting with clean, dry pump and tubing, was primed using this fixed volume of water, and then blanked; next 1.00 mL of the calibration solution (measured with a micropipette) was mixed into the water for a calibration concentration of 20 ppb.

Post-Calibration In the 2002 experiment, the 10-AU reading for the first 2.5 hrs after the dye release drifted between -0.77 ppb and 0.82 ppb with a mean of 0.80 ppb and a few abrupt 0.1 ppb spikes. This strongly suggests that some RWT contaminated the fish tank or the tubing during the blank. To correct for this error, we added 0.80 ppb to the final concentration measurements.

For the short 2002 experiment, we were not worried about drift in accuracy of the concentration measurements, as the 10-AU can hold its calibration accurately for months, but after the 2003 experiment, we observed that the intake hose, tubing, and the glass flow cell within the 10-AU had collected some sediment and algae, and we suspected that contamination of the flow cell may have biased the measurements toward the end of the experiment. To address this problem, we performed a post-calibration, shaking out as much water as possible from the fluorometer tubing, running a blank using water obtained from LO, about 200 m north and 500 m east of site FB, and then running 3.0 ppb, 6.0 ppb, and 9.0 ppb solutions mixed from a new RWT solution. The 10-AU reported concentrations of 0.46 ppb, 3.16 ppb, 5.84 ppb, and 8.41 ppb, respectively. Flushing the

10-AU with a weak chlorine bleach solution in the laboratory returned blank readings to 0.00 ppb.

We hypothesize that in 2003, while the zero-concentration reading was positively biased by contamination of the flow cell, the amount of light that was able to pass through the flow cell was attenuated by that same contamination, and so we corrected the raw 2003 concentration measurements $C_{raw}(t)$ using the equation $C(t) = A(t)(C_{raw}(t) - C_0(t))$, modeling the drift and the inverse attenuation coefficient with the exponential functions $C_0(t) = C_{0,p}e^{K_0(t-t_p)}$ and $A(t) = A_p e^{K_A(t-t_p)}$, respectively, where t_p represents the time of the postcalibration relative to variable time t, $C_{0,p} = 0.459$ ppb is the blank concentration measured during the postcalibration, and $A_p = 1.11$ is the inverse attenuation measured during the postcalibration using the 3.0 ppb solution (note that the value of A_p obtained from the 6 ppb and 9 ppb solutions is within 2%). The rate constant $K_A = 0.0063\,\text{day}^{-1}$ was obtained from $A(t_0) = 1$ where t_0 is the time of the dye release, and the rate constant $K_0 = 0.21\,\text{day}^{-1}$ was obtained from the strong dip in $C_{raw}(t)$ down to 0.087 ppb at time $t_1 = 8.930$ days after the dye release, following a 30 min inrush of LO water after a 5 hr period of flows mostly from LO into SP – we take this dip to represent a blank, setting $C_0(t_1) = 0.087$ ppb.

In Appendix C we make recommendations for calibrating and maintaining a flow-through fluorometer in long dye studies. These recommendations obviate the need for the elaborate post-calibration we performed in the 2003 SP study.

Background Fluorescence It is good practice to monitor a dye release site for background fluorescence prior to a dye study – for discussion, see Smart and Karunaratne (2002). Because background flourescence measurements were not carried out prior to either of our

experiments, we collected water samples at site FB at weekly intervals during the summer of 2004, beginning around 9 months after the 2003 dye study. These grab samples were analyzed in an SLM 8000c cuvette-based spectrofluorimeter, calibrated with a 3.0 ppb solution of RWT. No fluorescence was detected in the RWT band from any of the samples. Hence, we concluded that background fluorescence was unlikely to be an issue during the dye studies.

Sunlight Bias To assess the impact of leaving the intake tubing uncovered during the 2002 dye study, we conducted a day-long experiment on a day with similar weather to that of the May 15, 2002 dye release: May 24, 2006, a sunny day with very few clouds. The 10-AU was set up on the roof of Hollister Hall at Cornell University in Ithaca, New York, a location clear from shade, with uncovered polyethylene tubing facing to the east (same orientation as for the 2002 dye experiment). The instrument was blanked with distilled water and run from 9:30AM until dusk. We observed a maximum 0.16 ppb bias in the reading with changing light conditions (the concentration reading dropped with lower light). We conclude that sunlight bias was negligible.

Outflow

At site FB, the channel connecting SP to LO is 17 m wide and $2-3$ m deep depending on the water level. It is impossible to directly measure outflow through such a large cross-section. Our approach was to continuously monitor the vertical profile of velocity in the center of the channel using an RDI 1200 kHz Workhorse Monitor acoustic Doppler current profiler (ADCP), characterize the horizontal velocity profile in the upper half of the channel in a one-time experiment using an RDI 600kHz Workhorse Monitor ADCP,

measure the bathymetry of the channel under the footbridge, and continuously monitor water level in SP to adjust the cross-sectional area of the channel. From these three measurements, we estimate the total outflow through the cross-section. Extensive discussion of uncertainty analysis for these outflow measurements is found in King (2006).

Channel Bathymetry The channel cross-section at site FB was profiled using a weighted measuring tape to obtain an estimate of channel width as a function of elevation above the bed, $W(z)$. During portions of the experiments, it was possible to estimate the water depth at site FB, $H(t)$, from the location of the water surface indicated by the peak echo intensity measured by the 1200 kHzADCP. However, for significant portions of both exepriments, the water surface rose slightly above the range of the ADCP, and it was necessary to fill in the gaps in $H(t)$ with water surface elevation time series obtained at site DR, $H_{DR}(t)$. A constant shift ΔH was identified to match the water surface elevation measured at site FB using echo intensity with $H(t) = H_{DR}(t) + \Delta H$.

$H_{DR}(t)$ was measured as follows. Absolute pressure and temperature were continuously monitored using a Sea Bird Electronics SBE39 temperature/pressure recorder moored on the bed at site DR and sampling at 1 min intervals. Atmospheric pressure was measured every 15 min with a CS105 barometer using Vaisala's BarocapTM silicon capacitive pressure sensor – the barometer was located at a meteorological station on the shore of Little Sodus Bay, 150 m to the west of SP. Absolute pressure measured by the SBE39 was converted to gage pressure by subtracting atmospheric pressure, and gage pressure was converted to a water surface elevation time series using the formula $H_{DR} = p_g/(\rho g)$ where p_g is gage pressure, $g = 9.8\,\mathrm{m\,s^{-2}}$ is the acceleration of gravity, and ρ is the water density, found using the 1981 UNESCO formula for density of fresh water (Gill, 1982) and the SBE39 measurements.

Experiment	2002	2003
Mode	1	11
Vertical Bin Size	25 cm	1.0 cm
Blanking Distance	75 cm	5.0 cm
Ensemble Length	6.00 s	5.56 s
Pings per ensemble	20	1

Table 3.1: 1200kHz ADCP deployment configurations for vertical profiles.

Vertical Velocity Profile A vertical velocity profile was measured in the center of the channel (site FB) with an RDI 1200 KHz Workhorse Monitor ADCP looking upward from the bed. Details of the ADCP configuration for each study are given in table 3.1. Error velocity histograms were plotted, and an error velocity cutoff was chosen to filter out obvious outliers.

Power spectra of the along-channel centerline velocity near mid-depth (1.5 m above the bed) are plotted in figure 3.2. Lohrman et al. (1990) recommend taking ensemble averages over a time scale longer than the longest turbulent time scale but shorter than the time scales of variation in the average current, noting that ideally there is a spectral gap between these scales. The turbulent time scales are identified in figure 3.2 by the $-5/3$ slope. For the 2002 experiment, it is easy to identify a spectral gap, and we chose an ensemble averaging time of 2 min, equal to one-half the 4 min period at the low-frequency end of the spectral gap. The resulting velocity profiles followed the log-wake law (Coles, 1956). In 2003, the time scales of the average current were not clearly distinguishable from the turbulent time-scales, and so we chose an ensemble averaging time equal to 4 min, one-half of the 8 min period at the very top of the turbulent range. The resulting velocity profiles deviated strongly from the log-wake law (a few example velocity profiles

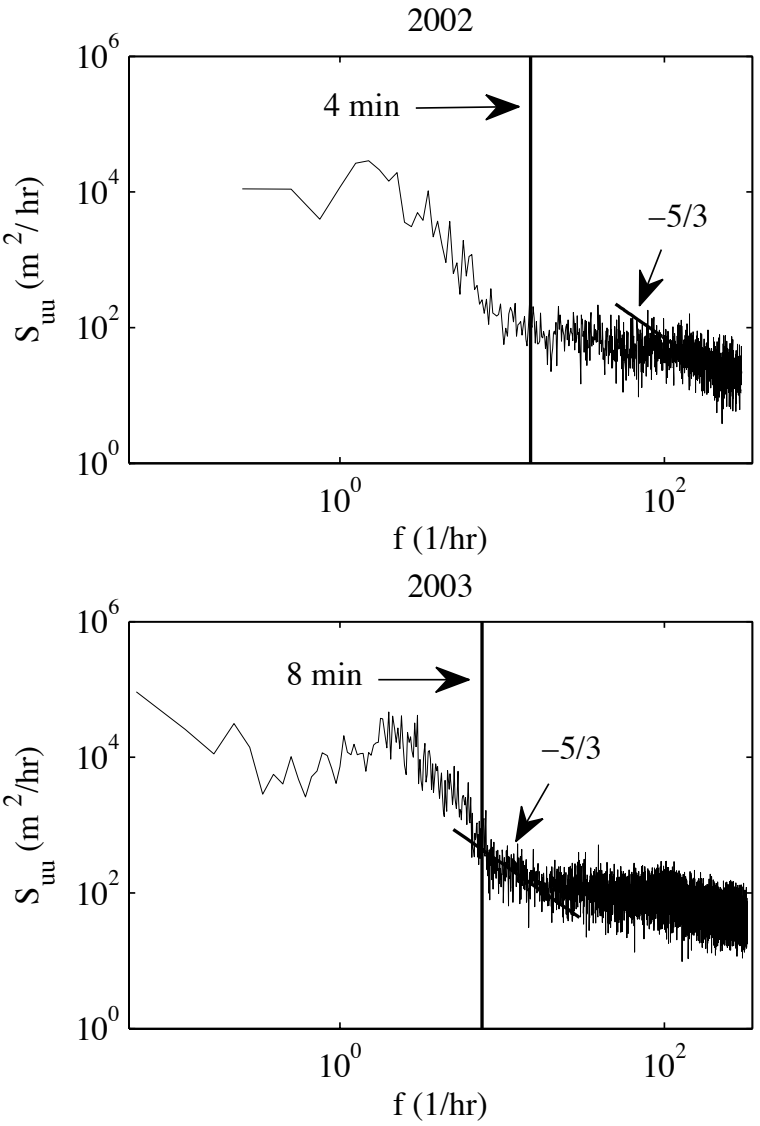

Figure 3.2: Power spectrum of channel velocity.

are shown in figure 3.3), instead exhibiting features of the accelerating boundary layer described in Soulsby and Dyer (1981).

In both 2002 and 2003, it was necessary to extrapolate the ensemble-averaged center-line velocities to the free surface and to the bed. Soulsby and Dyer (1981) derived the form of a second-order accelerating boundary layer based on an acceleration length scale

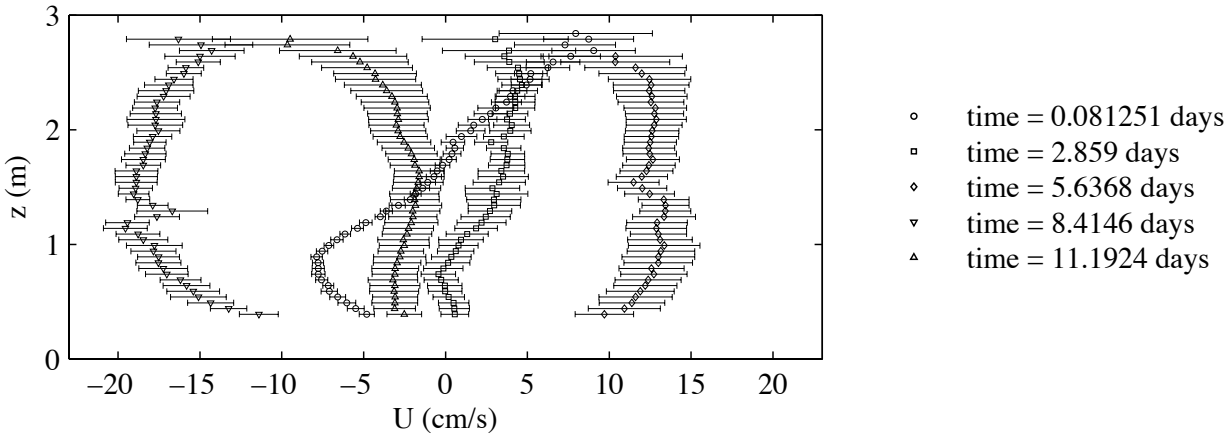

Figure 3.3: Example velocity profiles from 2003. Positive velocity is from SP to LO.

defined by $\Lambda \equiv |u_*|u_*/\dot{u}_*$ where u_* is the friction velocity and $\dot{u}_*$ is its time derivative. Adding the Coles wake parameter (Coles, 1956) to Soulsby and Dyer's profile, we may describe the accelerating boundary layer in the channel by

$$U_c = \frac{u_*}{\kappa}\left[\ln\left(\frac{z}{z_0}\right) - \frac{z-z_0}{\gamma\Lambda} + \frac{(z-z_0)^2}{\beta\Lambda^2} + 2\Pi\sin^2\left(\frac{\pi}{2}\frac{z-z_0}{H-z_0}\right)\right] \tag{3.8}$$

where U_c is the centerline ensemble-averaged along-stream velocity, z is elevation above the bed, $\kappa = 0.41$ is the Kármǹ constant and γ and β should also be universal constants. If u_*, γ, β, and Π are treated as free variables, equation 3.8 provides an excellent fit (defined by a χ^2 test) to 94% of the profiles measured in 2003. Although we did not find universal values of γ or β, we used the best fits to extrapolate the 2003 ensemble-averaged centerline velocity profiles to the bed and to the free surface (King, 2006).

The 2002 ensemble-averaged centerline velocity profiles, which were much coarser than the 2003 profiles, were extrapolated to the bed using the log law $U_c = u_*/\kappa\, ln(z/z_0)$, the roughness height $z_0 = 0.13$ m, and the drag coefficient $C_d \equiv (u_*/U(z_1))^2 = 0.020$, where $z_1 = 0.80$ m was the elevation of the lowest ADCP bin in 2002, and z_0 and C_d were

obtained from a best fit to the bottom four points in the higher-resolution 2003 velocity profiles; 2002 velocities were nearest-neighbor extrapolated to the surface.

Horizontal Velocity Profile To characterize the horizontal variation in velocity across the channel at site FB, we conducted a short experiment after the dye studies using a 600kHz RDI Workhorse Monitor ADCP, positioned at site FB on the right wall of the channel (looking from SP to LO), 1 m below the water surface, with its transducers looking towards the left wall of the channel. The ADCP was oriented so that beams 3 and 4 were in the horizontal plane with their bisector pointing straight across the channel. Beams 1 and 2 were blocked with acoustic foam (left unblocked, these beams reflected off of the water surface and the bed, and the reflected signal was picked up by transducers 3 and 4). The ADCP was configured in mode 1 to sample at 3.125 Hz with one ping per ensemble in 38 bins of 50 cm width for 4.7 hrs. Taking 8 min ensemble averages, we obtained 21 horizontal velocity profiles. Figure 3.4 shows the relationship between the measured centerline velocity U_c and the horizontally-averaged bulk velocity U. A least square linear fit yields the relationship $U = \phi U_c$ with $\phi = 0.86$.

Estimating Outflow Outflow (channel flow rate from SP to LO), $Q(t)$, was estimated from the centerline velocity profiles $U_c(t, z)$, the bulk-to-centerline velocity ratio ϕ, the channel widths $W(z)$, and the water depth $H(t)$ using the equation

$$Q(t) = \int_0^{H(t)} \phi U_c(z, t) W(z) dz. \tag{3.9}$$

We expect ϕ to vary with depth, but since we only measured the horizontal boundary layer structure at a single depth, we estimate ϕ to be constant with depth. Since the highest velocities are in the top portion of the channel where ϕ was measured, constant ϕ is a reasonable first-order approximation.

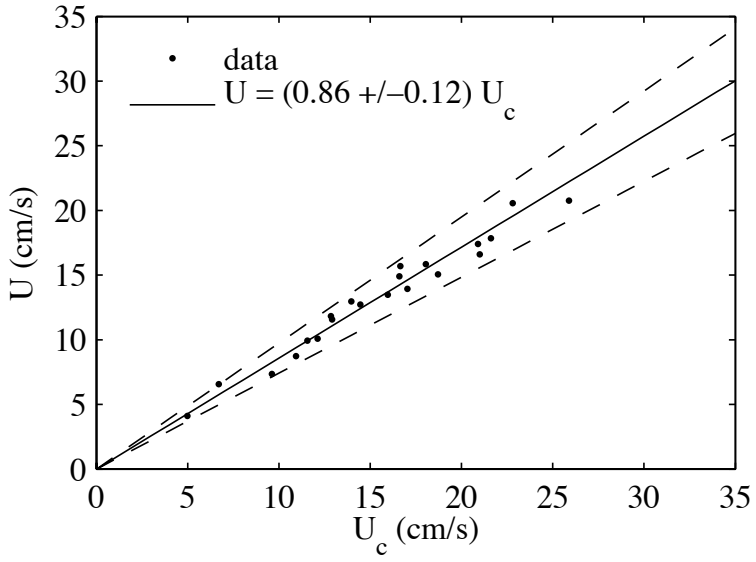

Figure 3.4: Measured U vs. U_c.

3.2.2 Correcting for Photolytic Decay

The meteorological station, located on the shore of Little Sodus Bay (150 m to the west of SP), logged total radiation (direct solar plus sky radiation) every 15 min measured by a LI-COR LI-200SZ pyranometer. Scalar irradiance (E_0 in equation 3.7) is the light energy per unit area incident on the surface of a sphere. However, the type of irradiance measured at our meterological station was plane downwelling irradiance, the light energy per unit area incident on the upper surface of a horizontal plane (it is scalar downwelling irradiance that determines the heat budget of a lake, which was of interest to us). Furthermore, irradiance of any type measured at a meteorological station represents light incident on the water surface whereas the rate of photolytic decay of RWT is determined by irradiance within the water column. Since SP is shallow and vertical stratification in SP was observed only occasionally in the northeast lobe (see figure 3.1) for a few hours during the night, and for several minutes during an upwelling event in LO, it is reasonable to

assume that in the course of a day particles of RWT traverse the depth several times, and thus the depth-average value of scalar irradiance will predict the rate of decay with sufficient accuracy. In summary, to correct for photolytic decay of RWT, it was necessary to convert plane downwelling irradiance measured at the water surface (which we denote E_{dS}) to the depth-average scalar irradiance in the water column (which we donote E_0).

Suijlen and Buyse (1994) found that upwelling irradiance in the water column accounts for under 5% of total scalar irradiance, so $E_0 \approx E_{0d}$ where E_{0d} is scalar downwelling irradiance. The Lambert-Beer law predicts exponential attenuation of light within the water column, resulting in the depth-average relationship

$$E_0 \approx E_{0d} = \gamma \frac{1 - \exp(-hK_d)}{hK_d} E_{0dS} \tag{3.10}$$

where E_{0dS} is the scalar downwelling irradiance incident on the water surface, h is the water depth, K_d is the wavelength-averaged attenuation coefficient, and γ is the time-averaged light transmission factor at the air-water interface. In a review of the literature, Suijlen and Buyse (1994) found light transmission factors ranging from 0.75 to 0.85, and we use $\gamma = 0.8 \pm 0.05$ in our analysis.

Equation 3.10 applies to a column of water of constant depth and attenuation coefficient while ideally our photolysis calculations would be a function of space, but since we made only visual observations of the location of the RWT during our study, this is impossible, and we model SP as a well-stirred tank of constant depth and attenuation coefficient for the purpose of photolysis corrections, applying equation 3.10 to the pond as a whole. We reason that since photolysis is more significant at higher concentrations, and initially after the dye release, when concentrations were highest, much of the RWT washed upstream into Sterling Creek, an appropriate representative depth is $h = 3\,\text{m} \pm 2\,\text{m}$ (the average depth of SC is about 3 m, and depths in SP and SC range from about 1 m to 5 m).

Attenuation coefficients vary widely in space, time, and also with light wavelength. Some attempts have been made to relate attenuation coefficients to Secchi disk measurements. For a given aquatic system, it is often the case that

$$K_d \cdot SD = \text{constant} \tag{3.11}$$

where SD is the Secchi depth. Effler (1985) demonstrate that this relationship should hold only when the relative contribution of light scattering and absorption remains constant. Examining $K_d \cdot SD$ in four different lake and reservoir systems, Effler (1985) find that constants between 1.11 and 1.98 provide best fits to the data, with standard error up to 0.11 in an individual system. Noting that it is common practice to employ the relationship $K_d \cdot SD = 1.9$, Effler (1985) recommend, 'In the absence of K_d measurements, adopting the $K_d \cdot SD$ value of 1.9 should be accompanied by broad sensitivity limits (e.g., ± 0.7).' By 'sensitivity limits', Effler (1985) means the 90% confidence interval, corresponding to a 95% confidence interval of 0.85 for a Gaussian error distribution.

Secchi depths measured during and one day prior to the 2003 dye experiment at three different sites are reported in table 3.2. The Stream Site is located near the dye release site (see figure 3.1). Since photolytic decay is exponential, initial decay is greater than subsequent decay, and since most of the RWT initially washed into SC, we take the values of SD measured at this location near the dye release site to be most representative of the SD relevant to RWT photolysis. The median value of SD at the Stream Site is 1.5 m. We adopt a value of $SD = 1.5\,\text{m} \pm 1.0\,\text{m}$ to account for variability of Secchi depth throughout SP and the relationship $K_d \cdot SD = 1.9 \pm 0.85$ as suggested by Effler (1985) to allow for generous uncertainty in the attenuation coefficient. Ideally, we would consider the spectral distribution of the attenuation coefficient, as attenuation could be greater or less in the $510 - 590$ nm band at which photolytic decay of RWT occurs.

	Stream Site		Center Site		LO Site	
Date	h (m)	SD (m)	h (m)	SD (m)	h (m)	SD (m)
Sept. 17	3.9	1.3	1.1	macro.	2.0	bottom
Sept. 20	2.6	1.5	0.75	macro.	1.7	bottom
Sept. 21	4	1.5	0.75	bottom	1.65	bottom
Sept. 24	3.75	1.9	0.9	0.7	1.3	bottom
Sept. 30	2.5	1.75	0.9	bottom	1.25	bottom

Table 3.2: Measurements of Secchi depth (SD) and water depth (h) from SP during the 2003 dye study (R. Doyle-Morin, personal communication). Recall that the dye study commenced on September 18. Measurements are taken at three different sites. The UTM Zone 18 coordinates (m) are 362588 (easting), 4799644 (northing) for the Stream Site, 362510 (easting), 4799924 (northing) for the Center Site, and 362400 (easting), 4800204 (northing) for the LO Site. Secchi depth at the center site was often not measureable due to the presence of macrophytes, indicated by 'macro.', and 'bottom' indicates that the Secchi disk was visible when resting on the bed.

Finally, we estimate the scalar downwelling irradiance incident on the water surface, E_{0dS} from the plane downwelling irradiance measured at the meteorological station, E_{dS}. According to Mobley (1994), E_{dS} is related to E_{0dS} by

$$E_{0dS} = \frac{E_{dS}}{\overline{\mu}_d} \tag{3.12}$$

at sea level where $\overline{\mu}_d = 0.75$. Li-Cor (personal communication) claims that E_{dS} is higher on a sunny day and lower on a cloudy day so that a good estimate of the uncertainty in $\overline{\mu}_d$ is 0.2. In the future, we hope to employ the software HydroLight-EcoLight, based on Mobley (1994), to estimate E_0 and K_d more precisely in the $510 - 590$ nm band from total E_{dS} measured at the meteorological station and from plankton and chemistry data measured during the dye study.

When calculating the flux $r(t)$ of dye out of SP as described in Section 3.1.3, we must consider that RWT may leave SP either via the channel connecting SP to LO or by photolysis. It is convenient, when considering photolysis, to define $S(t) \equiv 1 - R(t)$ to be the fraction of RWT remaining in SP at time t. The photolysis model outlined above is applied to SP as if the pond were a uniform depth, well-stirred tank. In this simplified model, $r(t)$ is given by

$$r(t) = \frac{Q(t)C(t)}{M_0} + kE_0(t)S(t). \tag{3.13}$$

The first term on the right hand side of equation 3.13 corresponds to the flux of RWT out of SP via the channel as described in Section 3.1.3, and the second term corresponds to the loss of RWT via photolysis.

Noting that $r(t) = -dS/dt$, we see that equation 3.13 is implicit, and so starting with $S(t_0) = 1$ at the time of the dye release, t_0, we solve for $r(t)$ and $S(t)$ by employing equation 3.13 and the simple forward difference scheme,

$$S(t + \Delta t) = S(t) - \Delta t r(t) \tag{3.14}$$

with a time step of $\Delta t = 4$ min, corresponding to the time step used to discretize the data.

Now $r(t)$ corresponds to the photolytic RWT we released into SP. If we wish to make estimates of *water* residence time and not the residence time of photolytic RWT, we must estimate what $r(t)$ and $R(t)$ would have been if the dye had not decayed via photolysis. Imagine that we released a conservative (non-photolytic) tracer in SP along with the RWT, and let $r_\infty(t)$ denote the fraction of that tracer that would have been leaving SP per unit time at time t, and let $S_\infty(t)$ denote the fraction of that tracer that would have remained in SP at time t. We may estimate these hypothetical quantities if we simply assume that the proportionality constant relating the concentration of tracer in the channel connecting SP to Lake Ontario to the concentration of RWT in the entire pond is the same for RWT as

for our hypothetical conservative tracer. This assumption is written explicitly as

$$\frac{C_\infty(t)}{C(t)} = \frac{S_\infty(t)}{S(t)}, \tag{3.15}$$

where $C_\infty(t)$ is the concentration of the hypothetical conservative tracer that we would have measured in the channel. Now for a conservative tracer, the fraction of dye leaving SP per unit time is given simply by

$$r_\infty(t) = \frac{Q(t)C_\infty(t)}{M_0} \tag{3.16}$$

Combining equations 3.15 and 3.16, we arrive at

$$r_\infty(t) = \frac{S_\infty(t)}{S(t)}\frac{Q(t)C(t)}{M_0}, \tag{3.17}$$

and we may numerically solve for $r_\infty(t)$ using

$$S_\infty(t + \Delta t) = S_\infty(t) - \Delta t r_\infty(t), \tag{3.18}$$

starting with $S_\infty(t_0) = 1$, along with equation 3.17 and the results of equations 3.13 and 3.14. In this way, we corrected the 2003 data for photolytic decay for RWT. In the following sections, we drop the ∞ notation, and $r(t)$, $R(t)$ and $\Theta(t)$ represent statistics for a hypothetical conservative tracer.

3.2.3 Estimating Mean Residence Time

When a tracer study does not account for 100% of the tracer mass, the flux curve must be extrapolated in time to obtain an estimate of the mean HRT. In order to extrapolate, it is necessary to have a model of the system. It is typically assumed that after some time the system becomes well-mixed and can be modeled as a continuously stirred tank reactor (CSTR), resulting in an exponential tail of the form

$$r(t) = r_0 e^{-k_0 t} \tag{3.19}$$

The rate $k_0 = Q/V$ where Q is the flow rate and V is the volume of the system. Conservation of mass requires that as $t \to \infty$, all of the mass leaves the system (see equation 3.3), which results in the constraint

$$r_0 = k_0 e^{k_0 t_0} \left(1 - R(t_0)\right), \tag{3.20}$$

where t_0 is the time of the initial point used to fit the tail for extrapolation, and $R(t_0)$ is the value of R measured at time t_0.

It is common for natural systems to contain transient storage zones, e.g., the wakes of rocks in rivers, side lobes in lakes, e.g., Valentine and Wood (1977), Kadlec (1994), Andradóttir and Nepf (2000). Transient storage in SP can be expected in the northeast lobe (see figure 3.1) and in the water inside the dense patches of aquatic vegetation. The simplest model for transient storage is a single CSTR adjacent to the main channel that exchanges tracer mass with the main channel at a rate directly proportional to the difference in concentration between the channel and the storage zone. Assuming that the main channel is also a CSTR, the following governing equations result:

$$\frac{\partial C_c}{\partial t} = -\alpha(C_c - C_s) - \frac{Q}{V_c} C_c \tag{3.21}$$

$$\frac{\partial C_s}{\partial t} = \alpha \frac{q}{1-q}(C_c - C_s) \tag{3.22}$$

where the subscript c indicates the channel zone, the subscript s indicates the storage zones, α is the rate of transfer between the storage zones and the channel, Q is the flow rate, V_c is the channel volume, and $q \equiv A_c/(A_c + A_s)$ is the fraction of the cross-sectional area occupied by the channel. Equations (3.21) and (3.22) represent our transient storage model (TSM). Solving equations (3.21) and (3.22) for C_c and noting that $r(t) = QC_c/M_0$, we find that

$$r(t) = r_1 e^{-k_1 t} + r_2 e^{-k_2 t} \tag{3.23}$$

where

$$k_{1,2} = \frac{1}{2}\left(\frac{\alpha}{1-q} + \frac{Q}{V_c}\right) \pm \frac{1}{2}\sqrt{\left(\frac{\alpha}{1-q}\right)^2 + \left(\frac{Q}{V_c}\right)^2 + 2\frac{\alpha}{1-q}\frac{Q}{V_c}(1-2q)} \tag{3.24}$$

Examination of Equation (3.24) reveals that $k_{1,2} \geq 0$ for all physical values of q, α, and Q/V_c. The conservation of mass condition (equation 3.3) results in the constraint

$$r_2 = k_2 e^{k_2 t_0}\left[(1 - R(t_0)) - \frac{r_1}{k_1}e^{-k_1 t_0}\right]. \tag{3.25}$$

In the special case where $k_1 = k_2$, the solution collapses to Equations (3.19) and (3.20). Note that the solution given by equation 3.23 is mathematically equivalent to the solution for two CSTR's in series (Levenspiel, 1999).

Because the mean residence time is equal to $\Theta(t)$ in the limit of $t \to \infty$, we take the unique approach of finding the best fit tail for $\Theta(t)$. The more common approach is to fit the log of $r(t)$ to find an exponential tail based on the CSTR model, but this approach is not appropriate when there is return flow, i.e., when $r(t)$ is negative for portions of the dye study, as the log will be imaginary. Our approach is robust to return flow. The wide success of tidal prism models demonstrates that averaging over the time scales of flow reversal (as in the computation of R and Θ) is reasonable for predicting transport time scales (e.g., Sandford et al., 1992; Luketina, 1998; Wells and Sealock, 2009), but this approach has not, to our knowledge, been applied to extrapolation of dye flux curves before now.

The fitting procedure is performed as follows. For the CSTR model, we find the best fit, in a least square sense, by varying the one free parameter, k_0, in the analytical equation

for $\Theta(t)$ based on the CSTR model:

$$\Theta(t) = \Theta(t_0) + \frac{r_0}{k_0^2}\left[e^{-k_0 t_0}\left(k_0 t_0 + 1\right) - e^{-k_0 t}\left(k_0 t + 1\right)\right]. \tag{3.26}$$

The parameter r_0 is not another free parameter, but is specified by equation 3.20 to satisfy the conservation of mass condition. For the TSM, we find the best fit, in a least square sense, by varying the three free parameters k_1, k_2, and r_1, in the analytical equation for $\Theta(t)$ based on the TSM:

$$\begin{aligned}\Theta(t) = \Theta(t_0) &+ \frac{r_1}{k_1^2}\left[e^{-k_1 t_0}\left(k_1 t_0 + 1\right) - e^{-k_1 t}\left(k_1 t + 1\right)\right] \\ &+ \frac{r_2}{k_2^2}\left[e^{-k_2 t_0}\left(k_2 t_0 + 1\right) - e^{-k_2 t}\left(k_2 t + 1\right)\right].\end{aligned} \tag{3.27}$$

The parameter r_2 is specified by equation 3.25 to satisfy the conservation of mass condition. In both equations 3.26 and 3.27, $\Theta(t_0)$ is the measured value of Θ at time t_0. We discuss the choice of the initial time for the least square fit in Section 3.3, choosing $t_0 = 0.5t_N$ for 2002 and $t_0 = 0.25t_N$ for 2003 where t_N is the final time for which we have measurements.

The CSTR and TSM best fits for 2002 and 2003 are plotted in figure 3.5. The TSM is necessary for a good fit to the 2002 data, while the CSTR and TSM models yield nearly identical results for 2003. Mean residence time was obtained from the extrapolated value of $\Theta(t)$ at $t = (10^{11})t_N$. Convergence was tested by confirming that $\Theta(t)$ at $t = (10^{11})t_N$ is close to $\Theta(t)$ at $t = (10^{10})t_N$ – the values were equal within machine precision. Mean residence times, based on the TSM for 2002 and the CSTR model/TSM for 2003, are reported in table 3.3.

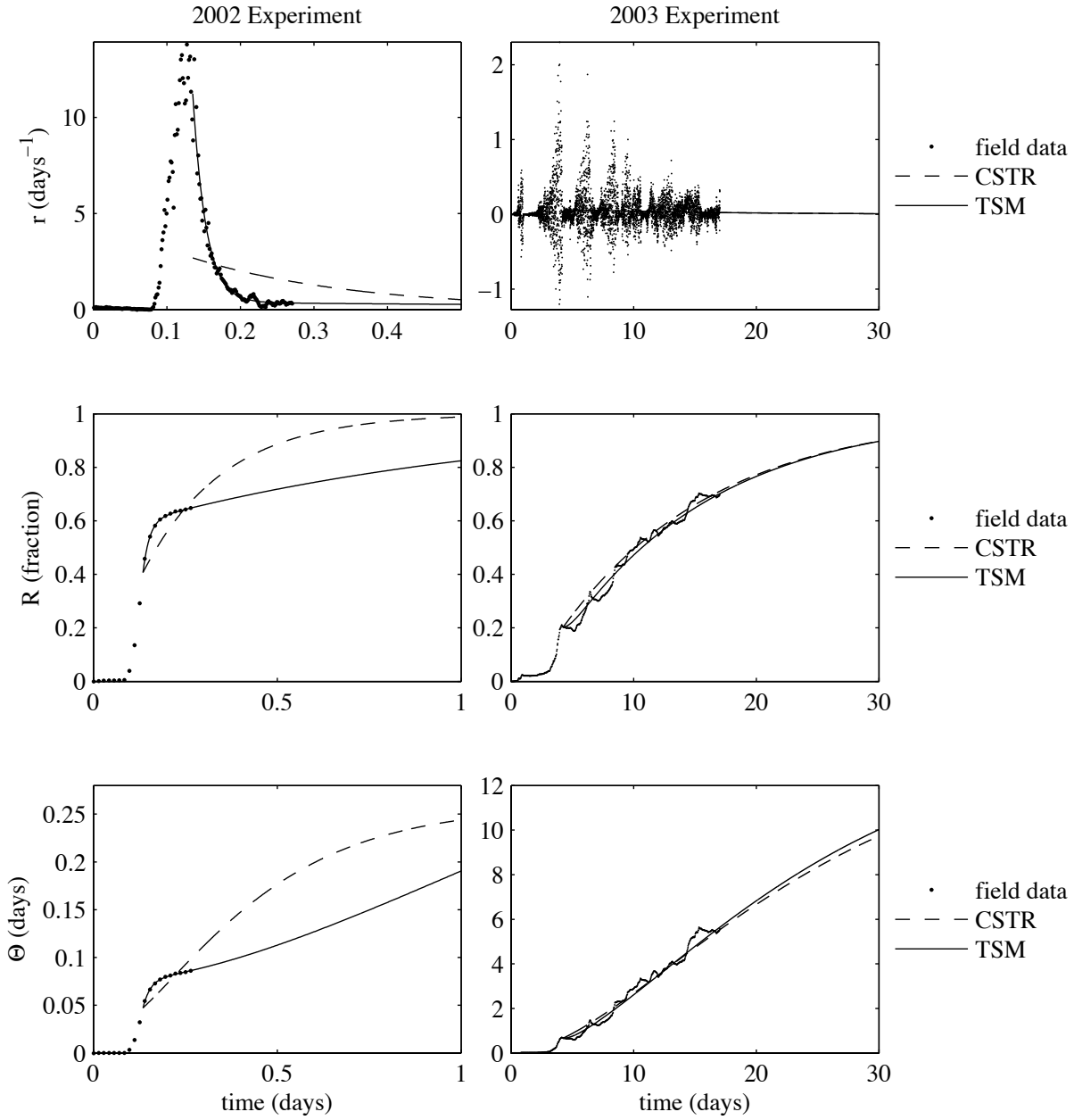

Figure 3.5: Best fits for $t_0/t_N = 0.5$ in 2002 and $t_0/t_N = 0.25$ in 2003. Note that every 10 data points are plotted for $R(t)$ and $\Theta(t)$ for visibility, but all points are plotted in $r(t)$. The CSTR and TSM yield visually indistinguishable results for 2003.

Experiment	T_R (days)
2002	0.55
2003	14.2

Table 3.3: Mean residence times estimated by extrapolating the measured dye flux curves for 2002 and 2003. For 2002, the mean residence time estimate is based on the TSM.

3.2.4 Uncertainty Analysis

For an arbitrary quantity ξ, let us define the error, $\Delta\xi$ to be the difference between the measured or calculated value ξ and its true value. Let us then define $\delta\xi$ to be the 95% uncertainty interval for ξ. That is, we expect $\Delta\xi$ to fall within $\pm\delta\xi$ with 95% confidence. Note that the expected value of $\Delta\xi$ is always zero if we have made our best estimate of the true value of ξ. Now let us discuss the various ways in which errors may be correlated in time t. The autocorrelation function, $\rho_{\Delta\xi}(\tau)$, for error $\Delta\xi$ is defined by

$$\rho_{\Delta\xi}(\tau) \equiv \frac{E\{\Delta\xi(t)\Delta\xi(t+\tau)\}}{\sigma_\xi^2} \tag{3.28}$$

where $E\{\ \}$ is the expected value operator and σ_ξ is the standard deviation of the error $\Delta\xi$.

Following standard terminology – e.g., Kline and McClintock (1953), a bias error is an error for which $\rho_{\Delta\xi}(\tau) = 1$ for all values of τ. On the other extreme, a precision error is an error for which $\rho_{\Delta\xi}(\tau) = 1$ for $\tau = 0$ but $\rho_{\Delta\xi}(\tau) = 0$ for all other values of τ. In many experiments, all errors may be classified as either bias or precision errors, but in the case of our dye studies, there are a few errors that are correlated over some finite but nonzero time scale. For example, a portion of the error in the conversion factor for centerline to bulk velocity, ϕ, is correlated over the time scale of oscillation in channel flow rate.

It is not straightforward to propagate uncertainties in measured quantities such as $Q(t)$ or $C(t)$ into an estimate of uncertainty in mean HRT. We took a Monte Carlo approach: for each dye study, N numerical experiments were performed in which errors were generated for each source of uncertainty. Each error was generated to be bias error (correlated perfectly over the entire experiment), a precision error (uncorrelated in time), or an error having an exponential autocorrelation function with a specified time scale. All errors except the error introduced by dye adsorption were assumed to be Gaussian. A thorough discussion of the other errors and estimated uncertainties in the SP dye studies is found in King (2006), and the methods for generating the errors are outlined in Appendix D. For each of the N experiments in the Monte Carlo simulation, $\Theta(t)$ was calculated and extrapolated using a best fit TSM for 2002 (with $t_0 = 0.5t_N$) and a best fit CSTR model (with $t_0 = 0.25t_N$) for 2003, to estimate mean HRT, resulting in a probability distribution for mean HRT.

3.3 Assessment

3.3.1 Outflow Measurement

Vertical Velocity Profiles

For the 2003 experiment, in which velocity deviated strongly from the log-wake law, we here assess the advantage of measuring the vertical velocity profile in high resolution. We compare the flow rate estimate obtained using the full vertical ADCP profile (Q) with flow rates estimated by two standard methods used by the United States Geological Survey for fixed-depth current meter measurement (Buchanan and Somers, 1969):

$(\overline{Q}-\overline{Q}_6)/\sigma_Q$	$(\overline{Q}-\overline{Q}_{28})/\sigma_Q$	$\overline{(Q-Q_6)^2}^{1/2}/\sigma_Q$	$\overline{(Q-Q_{28})^2}^{1/2}/\sigma_Q$
-0.011	-0.0064	0.10	0.11

Table 3.4: Statistics comparing estimates of flow rate for the 2003 experiment based on fixed-elevation velocity measurements and the full vertical velocity profile.

- The Sixth-Tenths Depth Method: The velocity measured at elevation $z = 0.6\overline{H}$ where $\overline{H}$ is the time-averaged water depth, is taken to be the cross-sectionally averaged velocity, resulting in flow rate estimate Q_6
- The Two-Point Method: The average of velocities measured at elevations $z = 0.2\overline{H}$ and $z = 0.8\overline{H}$ is taken to be the cross-sectionally averaged velocity, resulting in flow rate estimate Q_{28}

To obtain estimates of Q_6 and Q_{28}, we took into account the effect of fluctuations in water surface elevation on channel cross-sectional area and we corrected for the horizontal boundary layer, as described in Section 3.2.1.

In figure 3.6, we plot the probability density function for the difference between Q and both Q_6 and Q_{28}, based on all of the time series data. We have normalized by the standard deviation of Q because it is the fluctuation in Q that sets the HRT during this period of weak mean flow. Some statistics from this PDF are given in table 3.4 where the over-bar denotes a time average.

Using the flow rates Q_6 and Q_{28}, we may follow the methods described in Section 3.2.3 to estimate mean HRT for the 2003 experiment. We compare these estimates with the estimate based on Q in table 3.5. It is surprising how well the crude estimates of flow rate based on velocity at one or two elevations work, even in this scenario where vertical velocity profiles are highly atypical. The resulting error in mean HRT is on the order of

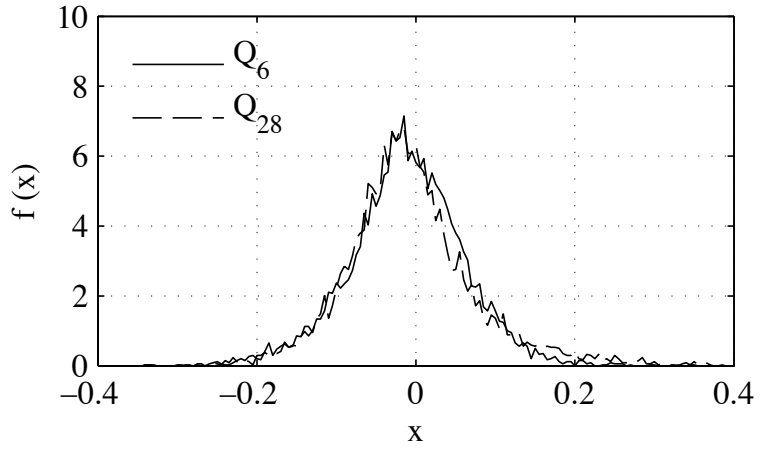

Figure 3.6: Probability density function f of $x \equiv (Q' - Q)/\sigma_Q$ where Q is the flow rate found from the ADCP profile, σ_Q is the standard deviation of Q, and Q' is either Q_6 or Q_{28}.

Outflow estimate	T_R (days)
Q	14.2
Q_6	15.8 (+11%)
Q_{28}	16.4 (+15%)

Table 3.5: Residence times for the 2003 experimnet from outflow rates based on the full vertical velocity profile (Q), the velocity at $z = 0.6\overline{H}$ (Q_6) and the average of the velocities at $z = 0.2\overline{H}$ and $z = 0.8\overline{H}$ (Q_{28}).

the uncertainty of the HRT estimate.

Horizontal Boundary Layer

Correcting for the horizontal boundary layer had a much greater impact on the final estimate of mean HRT than measuring the full vertical velocity profile. In table 3.6 we report the mean HRT estimates resulting from flow rate based on the bulk velocity (Q) and flow

Outflow estimate	2002 T_R (days)	2003 T_R (days)
Q	0.55	14.2
Q/ϕ	0.32 (-42%)	11.2 (-23%)

Table 3.6: Residence time (in days) with and without correction for lateral velocity variation across the channel.

Experiment	2002	2003
$\overline{(Q-\overline{Q})^2}^{1/2}/\overline{Q}$	0.29	8.9

Table 3.7: Ratio of the root mean square fluctuation in the flow rate to the mean flow rate for the 2002 and 2003 dye studies. The over-bar denotes a time average.

rate based on the centerline velocity (Q/ϕ). For the 2002 experiment, neglecting the horizontal boundary layer resulted in an estimate of mean HRT that was 42% too low. For the 2003 experiment, the error resulting from neglecting the horizontal boundary layer was 23%, also high, but not as significant as for the 2002 study.

It is possible that the impact of over-estimating flow rate on the final residence time estimate depends on the relative importance of reversing flow (driven by barotropic forcing) and steady flow from the watershed. In order to quantify the relative importance of these flow rate components, we computed the ratio of the root mean square of outflow (representing oscillatory flow) to the mean outflow (representing watershed flow) – this ratio is reported in table 3.7. We can see that flow from the watershed dominated in 2002 while oscillatory flow dominated in 2003.

Photolysis Correction	T_R (days)
corrected	14.2
uncorrected	16.4 $(+15\%)$

Table 3.8: Residence time (in days) for the 2003 experiment with and without correction for photolytic decay of RWT.

3.3.2 Photolysis

For the 2003 experiment, we can evaluate the impact of correcting for photolytic decay of RWT on the estimate of mean HRT. In table 3.8 we report mean HRT estimates based on photo-corrected and uncorrected dye flux curves. Correcting for photolytic decay of RWT in this 17-day experiment in upstate New York in the fall makes a 15% difference in our estimate of mean HRT. We conclude that during dye studies lasting more than a week, and in bright conditions, photolytic decay of RWT should not be ignored in residence time studies.

3.3.3 Residence Time

It is, in general, difficult to assess the validity of extrapolation, but if our extrapolation method is based on an appropriate physical model, we can expect that for some range of initial fitting times t_0, the results will be independent of t_0. Thus, to evaluate our extrapolation methods, we examined the sensitivity of T_R, the fitting parameters (k_0, k_1, k_2, and r_2) and the resulting minimum root mean square errors to the initial time t_0 for both the CSTR model and the TSM for the 2002 and 2003 experiments. For each value of t_0, the fitting parameters were varied systematically to obtain the best fit in a least square sense to $\Theta(t)$ between t_0 and t_N, where t_N is the final time of measurements. The results

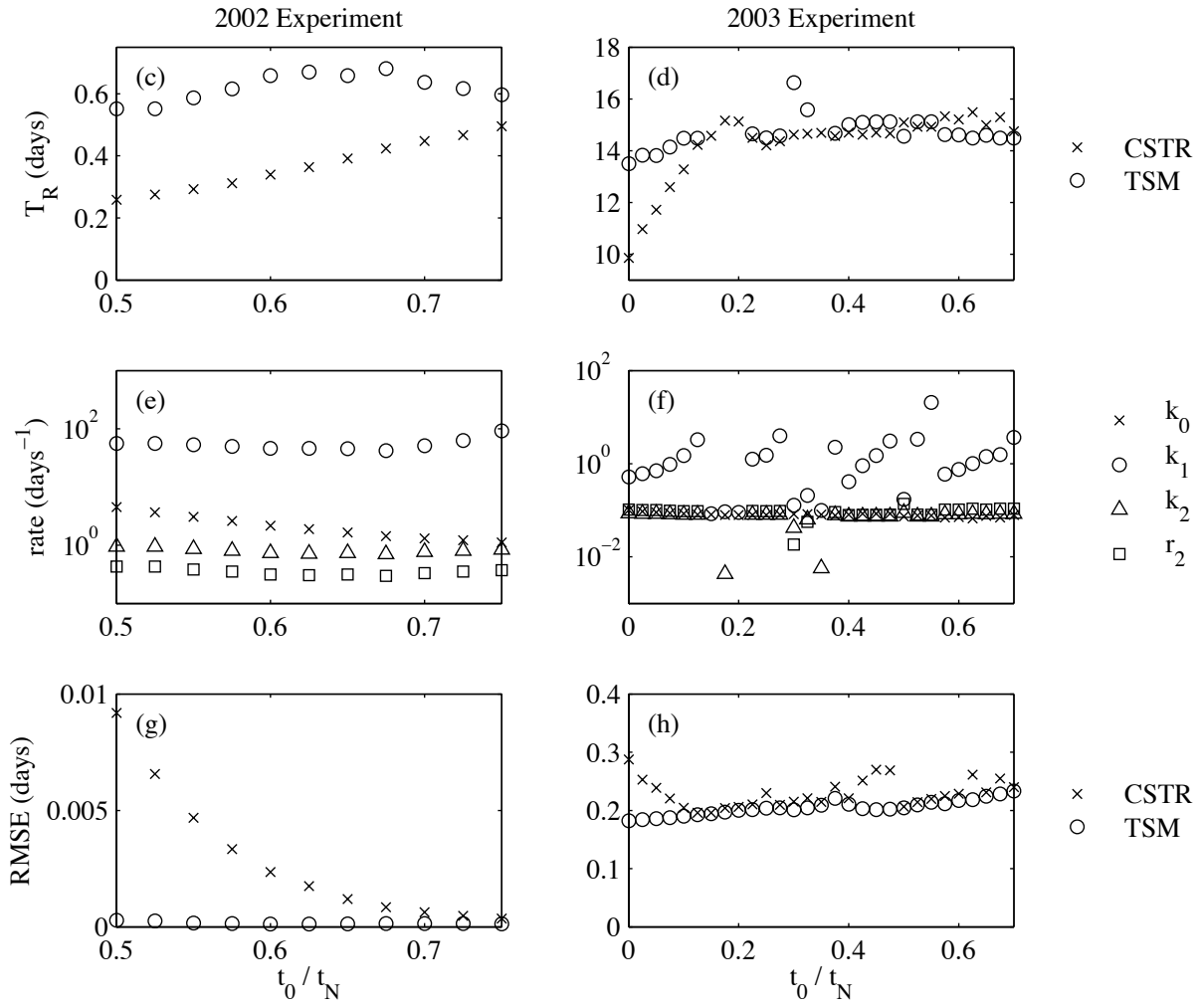

Figure 3.7: Dependence on initial time of fit (t_0) of residence time (T_R) and corresponding best fit parameters (k_0, k_1, k_2, and r_2) for CSTR model and TSM. t_0 is the initial time of the data used for fitting where the experiment starts at time 0 and the final piece of data is collected at time t_N.

are plotted in figure 3.7

For the 2002 experiment, the TSM yields much better fits to the data than the CSTR except at large t_0, for which the models yield similar results, but there is not really adequate data to justify the fit. The TSM yields slightly more stable estimates of residence

time. For values of $t_0 < 0.5t_N$ (not shown), neither model yields reasonable fits because there is a delay before the first traces of RWT exit SP, and until this occurs, neither model is valid because both assume well-mixed conditions. Based on this analysis, we chose to extrapolate the 2002 data using the TSM with $t_0 = 0.5t_N$ so as to base the extrapolation on as much data as possible using the model yielding consistently better fits.

For the 2003 experiment, the CSTR model results in a stable estimate of $T_R = 14$ days for $t_0 > 0.225t_N$ while the TSM does not become stable. Both the CSTR model and TSM break down when t_0 is too high (not shown). The CSTR model fits badly and yields T_R up to 40% lower for small values of t_0 while the TSM is more robust for small t_0, suggesting that the transient storage effects are most significant in this system for small times. Based on this analysis, we chose to extrapolate the 2003 data using the CSTR model with $t_0 = 0.25t_N$ so as to base the extrapolation on as much data as possible without dealing with transient storage effects.

3.3.4 Uncertainty Analysis

Statistics of the mean HRT for 2002 and 2003 resulting from the Monte Carlo uncertainty analysis described in Section 3.2.4 are given in table 3.9, and the full histograms of mean HRT are shown in figure 3.8[1].

We mentioned above that not all of the 2002 Monte Carlo results were included in the histograms and statistics presented so far. For 2002, while over 97.5% of the mean residence times were between 0.1 and 30 days, a small percentage were order $10^{11} - 10^{13}$ days. These numbers represent the case in which the smaller rate constant, k_2 is zero to machine

[1]Note that for the 2002 histogram and statistics, we have excluded a small fraction of the data because it is physically implausible – we discuss this below.

Experiment	N	mean T_R (days)	median T_R (days)	2.5th perc. T_R (days)	97.5th perc. T_R (days)
2002	19147	0.82	0.55	0.21	3.49
2003	19800	13.9	13.8	10.4	17.7

Table 3.9: Statistics of mean HRTs estimated from Monte Carlo method of modeling the experimental errors. We emphasize that these are statistics of a mean quantity, e.g., mean T_R is the mean of the mean HRT. For 2002, only the mean HRTs below 10^{10} days were used to calculate these statistics – there were 19596 (sorption not considered) and 28653 (sorption considered) total experiments for 2002.

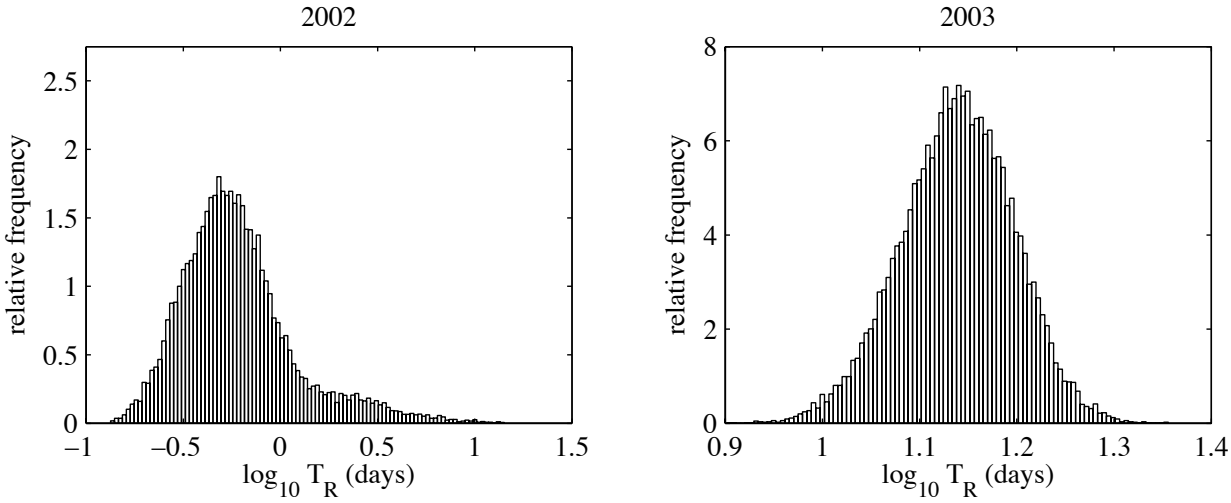

Figure 3.8: Results of Monte Carlo uncertainty analysis: histograms of mean HRT for 2002 and 2003. These are the results of extrapolating using a TSM model with $t_0/t_N = 0.5$ in 2002 and a CSTR model with $t_0/t_N = 0.25$ in 2003.

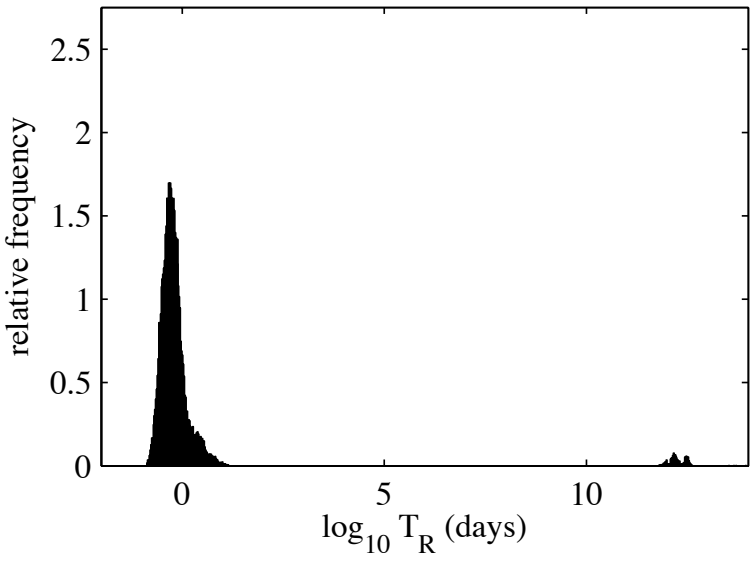

Figure 3.9: Results of Monte Carlo uncertainty analysis for 2002: histogram of mean hydraulic residence. These are the results of extrapolating using a TSM model with $t_0/t_N = 0.5$.

precision, such that the second term in $r(t)$ is a constant. This occurs when the k_2 component of the tail of $r(t)$ generated by our model of the errors has a flat slope or slopes upward, and the large mean residence times represent the infinite residence times that would result. We know that this scenario is not physically valid – it is an artifact of our model for the errors. Thus to compute the mean, median, and 95% confidence interval for the 2002 case, we filter out these infinite residence times. The full histogram for 2002 is plotted in figure 3.9. 2.29% of the mean HRT estimates exceed 10^{11} days. This is a very small percentage, and we ignore this data to calculate the statistics presented in table 3.9.

3.3.5 Sorption of RWT

There is one source of uncertainty we have not accounted for: possible sorption of RWT to the bed, to macrophytes, or to suspended sediment in SP. The degree to which sorp-

tion alters the dye flux curve and estimates of mean HRT depends on whether sorption is reversible and on the relative time scales of the sorption processes and the dye study duration, and whether sorption to suspended sediment is significant. If sorption is reversible, mainly to stationary substrates (e.g., the bed, macrophytes), and very quick compared to the duration of the dye study, then RWT will be adsorbed and released essentially instantaneously as it passes through the system, having negligible effect on the measured dye fluxes. However, if quick sorption takes place on suspended sediment, it would not be reversed quickly (because the sediment travels with the plume, allowing sorption to reach equilibrium), and could alter the dye flux curve. Total suspended sediment (TSS) in SP was measured to be between 0.2 to $10\,\mathrm{mg\,L^{-1}}$ in the summers of 2002 and 2003 (Xiaoxia Chen and Charles Driscoll, personal communication). In equilibrium, the fraction of RWT mass in solution is equal to $K_p R_s$. The maximum value of K_p measured in the literature is $450\,\mathrm{mL\,g^{-1}}$ (for isomer 2, Vasudevan et al., 2001). For this high value of K_p and the high value of $R_s = 10\,\mathrm{mg\,L^{-1}}$, only 0.45% of the RWT is adsorbed in equilibrium, so we may safely conclude that sorption to suspended sediment is negligible in SP.

If the time scale of sorption is very slow compared to the dye study duration, whether sorption is to suspended sediment or to fixed substrate, little sorption will take place during the dye study. If sorption takes place over time scales comparable to the dye study duration, whether it is reversible or not, and no matter the substrate, it could significantly alter the shape of the measured dye flux curve and the resulting estimates of mean HRT. From the few studies of sorption kinetics published to date, reviewed in Section 3.1.4, it appears that sorption of isomer 1 is likely reversible and takes place very quickly (in minutes) compared to the duration of both the 2002 and 2003 dye studies, while sorption of isomer 2 may take place over a time scale comparable or much longer to that of our dye studies (over hours or days). Without further study of sorption kinetics, we have no way

of estimating the effects of isomer 2 sorption on the dye flux curves. Furthermore, even with measurements of kinetic parameters, it is not straightforward to estimate R_s for a field dye study, as R_s depends on the amount of substrate exposed to the dye, which could vary with flow conditions. Ideally, sorption kinetics would be measured for sediment samples taken from the system, and sorption of RWT would be modeled along the lines of Sutton et al. (2001) or Keefe et al. (2004), and R_s would be a fitting parameter for the model.

3.4 Comments and Recommendations

We have presented a number of techniques that are appropriate in surface water dye studies aimed at measuring mean HRT. We have proposed that extrapolating measured tracer flux curves in order to estimate mean HRT is best accomplished using the running first moment $\Theta(t)$, which approaches the quantity of interest (the mean HRT) at infinite time. Not only is this method intuitively appealing when the aim is to estimate $\Theta(t)$ at long times, but it is robust in the case of significant return flow, which is ubiquitous in coastal systems such as freshwater embayments and estuaries. We have demonstrated that a simple TSM can offer good fits to tracer flux curves and estimates of mean HTR when a CSTR model breaks down. We have demonstrated that a Monte Carlo approach to uncertainty analysis, coupled with a simple model for extrapolation, can yield estimates of uncertainty in mean HRT when error propagation is not straightforward.

If resources are limited, our experience in SP suggests that it may be more important to capture horizontal variation in velocity than vertical variation in a channel of similar dimensions to the SP channel (17 m $\times$ 3 m cross section). The USGS method of estimating

mean vertical velocity from the velocity at elevation $0.6H$ is more robust than we might have thought in the case the accelerating boundary layer in SP. While the vertical variation in velocity significantly affected estimates of flow rate, the mean HRT estimate was affected less.

Photolytic decay can be important in dye studies, including RWT studies that last more than one week, and we have proposed a method to correct for photolytic decay. Uncertainty in the photolysis model can be minimized by directly measuring scalar irradiance in the water column from time-to-time during the dye study. The biggest unknown in RWT dye studies remains sorption.

We make the following recommendations for an optimal passive tracer release study in a natural surface water system with one or more outlets:

- Before the release, sufficiently dilute the tracer in water taken from the system to match the density of the tracer plug with the water in the system. The degree of dilution that is sufficient depends on the relative time scales of buoyant forces, which will sink the tracer (if it is heavier than the water) and turbulent diffusion, which will re-suspend the tracer.
- Accurate measurement of flow rate and concentration at the exits is paramount:
  - Characterize the background concentration signal before conducting the tracer release, ideally monitoring for months, using grab samples if continuous monitoring is prohibitive. In choosing the mass of the release, aim for tracer concentrations well above background throughout the study.
  - If using a flow-through fluorometer in a system with significant sediments or algae, it is important to clean the flow cell periodically. A method for cleaning

is outlined in Appendix C.

  - Take a zero concentration reading both in distilled water and in system water as this may be useful in post-calibration.
  - Characterize time-scales of flow unsteadiness and boundary layer structure at the exits before deciding on a method for monitoring flow rate. Single vertical point measurement of velocity may be sufficient depending on the flow structure at the exit, even in a highly unsteady channel.

- If using a fluorescent dye, consider correcting for photolytic decay (for RWT this should be considerd if the duration of the tracer study lasts more than a few days). If correction for photolytic decay may be necessary, monitor plane downwelling irradiance continuously at an above-water meteorological station and take multiple measurements of scalar irradiance in the water in the relevant wave band (for RWT, $510 - 590$ nm) for correlation with the surface plane irradiance measurements. If underwater irradiance measurements are not feasible, Secchi depth measurements can provide some information on photolysis rates, although uncertainty will be high and should be accounted for.
- If extrapolation of tracer flux curves is necessary, it is important to ensure that the extrapolation method does not violate conservation of mass – $R(t)$ must approach 1 as $t \to \infty$. We advocate the use of $\Theta(t)$ for fitting and extrapolation because it approaches the quantity of interest, mean HRT, as $t \to \infty$.
- Collect water, sediment, and plant samples from the study site to characterize the kinetics, equilibrium conditions, and reversibility of sorption. If the sorption time scales are much longer than the tracer study duration, then negligible sorption will take place during the study. Likewise, if the sorption time scales are quick compared to the tracer study duration, and if sorption is completely reversible, then sorption

will have negligible effects on the measured tracer flux. If sorption is quick and irreversible, the method proposed by Dierberg and DeBusk (2005) can be employed to estimate mean HRT. However, if sorption time scales are on the order of the tracer release study duration, sorption cannot be ignored, whether it is reversible or not, and it is best to find a tracer that does not exhibit large sorption effects in the system of interest. Modeling techniques, such as those employed by Sutton et al. (2001) and Lin et al. (2003), may be used to account for sorption effects, but they involve many tuning parameters that are difficult (or impossible) to measure directly.

CHAPTER 4

CONCLUSIONS

We have presented new tools for modeling and measuring mixing and transport in surface water systems, both at the relatively small scale of vertical mixing in aquatic plant canopies and at the larger scale of bulk transport. Both of these tools can be used to characterize residence time scales of SP, the system that inspired this work – the turbulence model can be incorporated into a larger hydrodynamic solver that can model dye release studies under a variety of physical forcing conditions, and the new techniques for measuring mean HRT have provided a direct measurement of this time scale as well as a benchmark for a hydrodynamic model.

Our k–ε model for flow through aquatic vegetation is unique in its treatment of dissipation of TKE in the wakes of plant stems. We find that in the case of rigid cylinders, commonly used to model vegetation in laboratory settings, correctly modeling dissipation of TKE at the stem scale is critical for predicting TKE in the emergent case and also improves predictions of TKE, mean velocity, and Reynolds stress in the submerged case. We anticipate that the new model will perform well when applied to flow through real aquatic vegetation, where we have observed that dissipation scales both with the stem scale and with the scales of vertical shear. Real plants are often characterized by a frontal area profile, $a(z)$, that varies strongly in z. Furthermore, as flow velocity increases, real plants may bend such that $a(z)$ and C_D become smaller. R. O. Tinoco and E. A. Cowen are currently conducting measurements of $a(z)$, mean velocity, TKE, Reynolds stress, and bulk drag as a function of Reynolds number in a laboratory flume populated with live Eurasian watermilfoil, and we will use the data from this study to develop relationships between $a(z)$, C_D, and Reynolds number and to test the model in real vegetation.

Preliminary results suggest that in Eurasian watermilfoil, it is simple to identify a single characteristic length scale that predicts scaling of dissipation, defined as the effective diameter of the plant stems, $d = a/n$ (for cylinders, $a = nd$). In more heterogeneous canopies with multiple stem scales, application of the new model may be more difficult, and this is an area for future study. Other future projects include extending the model for use in unsteady flows (e.g., under surface waves) and verifying if the model works with typical parameterizations of mixing in stratified flows.

We have further developed the classic pulse tracer release method for measuring mean HRT in natural systems that exhibit highly variable flow rates, presenting a new method for extrapolation of measured dye flux curves (used to estimate mean HRT) that does not violate conservation of mass, a method for correcting dye flux curves for photolytic decay of fluorescent water tracing dyes, and a method for estimating uncertainty in measured mean HRT. We also explore techniques for measuring outflow, an important component of dye flux, in an unsteady channel and recommend methods for measuring dye concentration over long durations in particle-laden waters. We applied these new techniques in dye studies conducted in SP, finding that our new extrapolation method is robust to highly unsteady flow rates, that correcting for photolytic decay improves our estimate of mean HRT by 15% in our three-week dye study, that fully characterizing the vertical boundary layer when measuring outflow improves estimates of mean HRT by up to 15% in SP, and that fully characterizing the horizontal boundary layer improves estimates by up to 42%.

The missing piece in our analysis of the dye studies conducted in SP is sorption. The existing literature on sorption of RWT focuses on equilibrium conditions and does not adequately address sorption kinetics or reversibility, which are critical in determining whether sorption significantly alters measurements of tracer flux. In future work, we

hope to further characterize sorption properties of RWT in wetland sediments and plants, focusing on kinetics and reversibility. If the time scales and reversibility of sorption were more fully characterized for different sediment types and water tracers, the effects of sorption on the results of tracer release studies could be better anticipated and either avoided or modeled.

APPENDIX A

PRE-EXISTING K–ε MODELS FOR VEGETATED FLOW

A.1 López–García Model

The López–García model is described in detail in López and García (2001). The momentum equation is identical to (2.35). The TKE equation is given by

$$0 = \frac{\partial}{\partial z}\left(\frac{\nu_T}{\sigma_k}\frac{\partial k}{\partial z}\right) + P_s + P_w - \varepsilon \tag{A.1}$$

where P_s and P_w are modeled as in (2.40) and (2.41), respectively. Note that in López and García (2001), β_p is called C_{fk}, and $C_{fk} = 1.0$. Note that if we sum the two TKE equations in the new model, (2.38) and (2.39), we arrive at (A.1), so the López–García equation for TKE is identical to ours; the differences are in the dissipation equation and the turbulent eddy viscosity. López–García model the dissipation using a single equation:

$$0 = \frac{\partial}{\partial z}\left(\frac{\nu_T}{\sigma_\varepsilon}\frac{\partial \varepsilon}{\partial z}\right) + \frac{\varepsilon}{k}\left(C_{\varepsilon 1}P_s - C_{\varepsilon 2}\varepsilon + C_{f\varepsilon}P_w\right) \tag{A.2}$$

where $C_{f\varepsilon}$ is a model constant. As in the standard k–ε model, the turbulent eddy viscosity is modeled as $\nu_T = C_\mu k^2/\varepsilon$. Arguing that in the absence of mean shear (i.e., in dense, emergent vegetation), wake production must balance dissipation, López and García (2001) conclude that $C_{f\varepsilon} = (C_{\varepsilon 2}/C_{\varepsilon 1})C_{fk} = 1.33$. While we agree that in the absence of mean shear, wake production must balance dissipation, we disagree that (A.2) is the proper way to model dissipation in emergent vegetation, where dissipation scales with stem diameter, which is not included anywhere in (A.2).

A.2 Katul Model

The Katul model is described in detail in Katul et al. (2004). The momentum equation is identical to (2.35). The TKE equation is given by

$$0 = \frac{\partial}{\partial z}\left(\frac{\nu_T}{\sigma_k}\frac{\partial k}{\partial z}\right) + P_s + P_w - W - \varepsilon \tag{A.3}$$

where P_s, P_w, and W are modeled as in (2.40), (2.41), and (2.42). The Katul model for TKE differs from the new model and from the López and García (2001) model by the inclusion of W, the rate of conversion of SKE to WKE. The argument for including W as a sink for total TKE is that small-scale WKE is dissipated very quickly. We find it puzzling that under this assumption, the WKE production term, P_w, is also included in in the TKE equation. The dissipation rate, ε, is modeled using

$$0 = \frac{\partial}{\partial z}\left(\frac{\nu_T}{\sigma_\varepsilon}\frac{\partial \varepsilon}{\partial z}\right) + \frac{\varepsilon}{k}\left(C_{\varepsilon 1}P_s - C_{\varepsilon 2}\varepsilon + C_{\varepsilon 4}P_w - C_{\varepsilon 5}W\right) \tag{A.4}$$

where $C_{\varepsilon 4}$ and $C_{\varepsilon 5}$ are model constants. As in the standard k-ε model, the turbulent eddy viscosity is modeled as $\nu_T = C_\mu k^2/\varepsilon$. Katul et al. (2004) use different model constants for terrestrial and aquatic vegetation. For aquatic vegetation, they use $\beta_p = 1.0$, $\beta_d = 4.0$, $C_{\varepsilon 4} = 1.5$, and $C_{\varepsilon 5} = 1.5$.

APPENDIX B

EQUILIBRIUM CONCENTRATION IN BATCH SORPTION STUDIES

In the text, we critique the analysis and conclusions of several papers regarding partition coefficients and reversibility in sorption batch studies. Here we present the calculations that lead us to disagree with these papers.

In a RWT sorption batch study, a known mass of solid substrate is added to a bottle containing a known concentration of RWT in water. As the bottle is shaken, the concentration of RWT in solution is monitored until equilibrium is reached. It is more difficult, though possible, to monitor concentrations of RWT in the substrate.

Let us define the following variables (units in parenthesis) for a batch study:

$V =$ volume of water in the batch container (volume)

$\rho_W =$ density of water (mass per unit volume)

$\theta_S =$ substrate-to-water ratio (mass substrate per unit mass water)

$R_S =$ bulk density (mass substrate per unit volume water)

$C =$ concentration of RWT in solution (mass RWT per unit volume water)

$C_0 =$ initial concentration of RWT in solution (mass RWT per unit volume water)

$C_E =$ equilibrium concentration of RWT in solution (mass RWT per unit volume water)

$q =$ concentration of RWT in substrate (mass RWT per unit mass substrate)

$q_0 =$ initial concentration of RWT in substrate (mass RWT per unit mass substrate)

$q_E =$ equilibrium concentration of RWT in substrate (mass RWT per unit mass substrate)

$K_p \equiv q_E/C_E$ is the equilibrium partition coefficient (volume per unit mass)

Note that $R_S = \rho_W \theta_S$.

At any given time, the mass of RWT in the liquid phase (in solution) is equal to CV, and the mass of RWT in the solid phase (sorbed) is equal to qR_SV. In the standard sorption batch study, the sediment is initially free of RWT, i.e. $q_0 = 0$, thus mass conservation requires $C_0V = q_E R_S V + C_E V$. Solving for K_p in terms of C_0 and C_E, we find

$$K_p = \frac{1}{R_S}\left(\frac{C_0}{C_E} - 1\right). \tag{B.1}$$

Alternatively, we may solve for K_p in terms of C_0 and q_E, finding

$$K_p = \frac{q_E}{C_0 - q_E R_S}. \tag{B.2}$$

Once K_p is known, we may predict C_E and q_E from C_0 as follows

$$C_E = C_0 \frac{1}{1 + R_S K_p}, \tag{B.3}$$

$$q_E = C_0 \frac{K_p}{1 + R_S K_p}. \tag{B.4}$$

From their batch studies, Lin et al. (2003) obtain estimates of equilibrium partition that we believe are around 1000 times too high – such an error might have resulted from neglecting to include ρ_W in their calculation of $R_S = \rho_W \theta_S$ which is used in equation B.1. Here we assume that $\rho_W = 1000\,\mathrm{g\,L^{-1}}$ (accurate within 1% for temperatures between 0 and 45^oC at atmospheric pressures typical on earth), and we examine the equilibrium batch results plotted in Lin et al. (2003) figure 7, making our own estimates of K_p from these results. The dependent axis in figure 7 is the percentage of RWT remaining in aqueous solution – this is equal to $C/C_0 \times 100\%$. For each experiment, figure 7 demonstrates that equilibrium is reached within the experimental time window, hence we read C_E/C_0

Table B.1: Quantities read and calculated from figure 7 of Lin et al. (2003).

label in figure	θ_S (g/g)	C_E/C_0	$R_S = \rho_W \theta_S$ (g/L)	K_p (L/g)
20ppb, 1/5	0.20	0.21	200	0.019
20ppb, 1/10	0.10	0.44	100	0.013
7ppb, 1/5	0.20	0.26	200	0.014
7ppb, 1/10	0.10	0.42	100	0.014
7ppb, cattail, 1/5	0.20	0.38	200	0.008
20ppb, abiotic, 1/5	0.20	0.32	200	0.010
20ppb, plant detritus, 1/100	0.01	0.21	10	0.38

from the final data point in each experiment. The data read from figure 7, namely θ_S and C_E/C_0, are given in our table B.1 along with our calculations of R_S and our estimates of K_p calculated from equation B.1 using these data. Our estimates of K_p are smaller than the values reported by Lin et al. (2003) in their figure 8 and in the text by a factor of about 1000.

To test reversibility of sorption after a standard sorption batch study, the equilibrium RWT solution is removed from the bottle and replaced with clean water, the bottle is shaken, and the concentration of RWT in solution is monitored until a new equilibrium is reached. Letting primed symbols denote the concentrations in the reversibility study and letting non-primed symbols denote the concentrations from the preceding sorption study, $C_0' = 0$ and $q_0' = q_E$, thus conservation of mass requires $q_E R_S V = q_E' R_S V + C_E' V$. If sorption is completely reversible, then $q_E'/C_E' = K_p$. Assuming that sorption is completely reversible, and solving for C_E' yields

$$C_E' = q_E \frac{R_S}{1 + K_p R_S}, \tag{B.5}$$

and employing equation B.4, we find

$$C'_E = C_0 \frac{K_p R_S}{(1 + K_p R_S)^2}, \tag{B.6}$$

and

$$q'_E = C_0 R_S \left(\frac{K_p}{1 + K_p R_S} \right)^2. \tag{B.7}$$

Lin et al. (2003) conduct a sorption reversibility study, concluding that less than 10% of the sorption was reversible because less than 10% of the dye is returned to solution by desorption. However, even if sorption is 100% reversible, we predict from equation B.6 that less than 10% of the original RWT would be recovered during these reversibility studies. In their figure 9, Lin et al. (2003) plot RWT concentrations during their desorption studies. In table B.2, we report the data given in Lin et al. (2003) figure 9, including θ_S, C_0 (assuming that the specific gravity of RWT is equal to 1, so that 1 ppb $= 10^{-6}$ g L^{-1}), and the measured equilibrium RWT concentration (which we denote C'^m_E). In table B.2, we also report the values of K_p found from the sorption studies (as shown in table B.1, the equilibrium RWT concentration C'_E that we predict from equation B.6 for the case of completely reversible sorption, and the percentage of C'_E recovered in the study, i.e., $C'^m_E / C'_E \times 100\%$.

We see that while less than 10% of the original RWT mass was recovered in solution during the desorption studies, between 73% and 103%[1] of the RWT we expected to desorb in the case of completely reversible sorption was desorbed in each of the studies. We thus conclude from this study by Lin et al. (2003) that sorption of RWT is largely reversible; this is contrary to the conclusion reached by Lin et al. (2003) that sorption of RWT is largely irreversible.

[1]Note that it is not possible to recover greater than 100% of the dye – the 103% figure must result from experimental error.

Table B.2: Quantities read and calculated from figure 9 of Lin et al. (2003), and from our table B.1.

label in figure	θ_S (g g^{-1})	C_0 (μg L^{-1})	$C_E'^m$ (μg L^{-1})	K_p (L g^{-1})	C_E' (μg L^{-1})	$C_E'^m/C_E'$ $\times 100\%$
20ppb, 1/5	0.20	20	2.8	0.019	3.3	85%
20ppb, 1/10	0.10	20	3.6	0.013	4.9	73%
7ppb, 1/5	0.20	7	1.4	0.014	1.4	103%
7ppb, cattail, 1/5	0.20	7	1.3	0.008	1.7	78%
20ppb, plant detritus, 1/100	0.01	20	2.9	0.38	3.3	88%

Trudgill (1987) also conduct a reversibility study, using much higher concentrations of RWT and a sample of brown calcareous earth (their 'soil 1'). Trudgill (1987) does not clearly state the soil-to-water ratio used for the desorption study, but does mention a soil-to-water ratio of $\theta_S = 0.5$ g g^{-1} for soil 1 in their figure 3. We assume that this ratio was used in the sorption study as it is the only mention of a soil-to-water ratio in regard to soil 1 that is found in the article. Again assuming $\rho_W = 1000$ g L^{-1}, we obtain $R_S = 500$ g L^{-1}. The values of the initial RWT concentration (C_0), the initial equilibrium sediment RWT concentration (q_E), and the equilibrium sediment concentration measured after desorption (which we denote $q_E'^m$) are given in Trudgill (1987) table XI, and we have included these date in our table B.3. Trudgill (1987) do not give units for C_0, but units of μg L^{-1} seem likely in context, and so we assume these are the units for C_0. In table B.3, we also show the value of K_p we calculate from the Trudgill (1987) data using equation B.2, the value of q_E' we predict from equation B.7 under the assumption that sorption is completely reversible, and the percentage of RWT recovered in solution compared to the amount of RWT that would have been recovered had sorption been completely re-

Table B.3: Quantities read and calculated from table XI of Trudgill (1987).

C_0 (μg L^{-1})	q_E (μg g^{-1})	$q_E^{'m}$ (μg g^{-1})	K_p (L g^{-1})	q'_E (μg L^{-1})	$(q_E - q_E^{'m})/(q_E - q'_E)$ $\times 100\%$
2000	3.8	3.6	0.038	3.61	105%
1500	2.85	2.8	0.038	2.71	35%
1000	1.9	1.84	0.038	1.81	63%
500	0.95	0.93	0.038	0.90	42%

versible – equal to $(q_E - q_E^{'m})/(q_E - q'_E) \times 100\%$. Note that $(q_E - q_E^{'m})/(q_E - q'_E) = C_E^{'m}/C'_E$. We see that between 35% and 100% of the RWT that would have been recovered were sorption completely reversible was recovered in the desorption experiments of Trudgill (1987). However, because much of the RWT remains in the substrate, this RWT recovered into solution represents only 3.0% to 5.3% of the original RWT in solution at the beginning of the batch sorption study that precedes a desorption experiment. From these low numbers, Trudgill (1987) concluded that RWT sorption is almost completely irreversible. However, we conclude from our calculations that the Trudgill (1987) experiments suggest RWT sorption is at least 35% reversible for this particular soil sample.

In both the Lin et al. (2003) and Trudgill (1987) desorption studies, confusion arose because not all of the original RWT used in the batch study was recovered after a single change of the water in the reactor. However, this was to be expected because in equilibrium, some of the mass remains in the substrate to satisfy the sorption isotherm. To better test reversibility of sorption, multiple flushes with clean water should be performed until no more RWT can be recovered into solution.

APPENDIX C

FLUOROMETER CALIBRATION AND MAINTENANCE

From the 2003 dye experiment, we gained a great deal of knowledge about operating a flow-through fluorometer in the field for weeks at a time. We recommend the following to anyone conducting a long-term dye release experiment and monitoring with a flow-through fluorometer, especially in water where plant matter or sediment is present. Assuming that the fluorometer is calibrated using water from the system under study, blank and standard measurements should also be taken in distilled water at the beginning of the study (after the calibration) for future reference. Perform this procedure every few days, or more often if large amounts of plant matter or sediment are present in the water:

- Stop the fluorometer, and pull it out of the water.
- Perform a post-calibration. That is, observe the concentration reading for a known blank and standard (prepared with distilled water), but do not alter the fluorometer settings.
- After the post-calibration, run a soultion of diluted bleach through the fluorometer until the concentration reading is zero (or the equivalent of zero measured in distilled water at the beginning of the study). In our experience, this will clean out the flow cell; if the fluorometer reading does not reach zero, manual cleaning may be necessary.
- Thoroughly wash away the bleach solution (which reacts with RWT) by flushing the fluorometer with plain water several times. Make sure to dispose of the bleach solution far from the field site.
- After the post-calibration(s) and cleaning, return the fluorometer to its regular operations.

APPENDIX D

GENERATING RANDOM TIME SERIES FOR ERROR ANALYSIS

For each run $n = 1...N$ of the Monte Carlo simulations, errors of different types were generated using MATLAB ® 7.7.0.471 (R2008b) as follows. A pseudo-random number stream, randstr, was generated using the Ziggurat algorithm with the following command:

$$\text{randstr} = \text{RandStream.create}(\text{'mrg32k3a'}, \text{'seed'}, \text{s}); \tag{D.1}$$

where s is the seed, which may be set to any real number to generate a unique pseudo-random number stream.

The uniform random variable R_{inf} was modeled using the rand.m script, which generates a uniform random variable between zero and one, as follows:

$$\text{Rinf} = \text{RN} + \text{rand}(\text{randstr}, 1). * (1 - \text{RN}) \tag{D.2}$$

where Rinf represents R_∞ and RN represents R_N.

All other errors were assumed to have normal distributions and were built upon the randn.m script, which generates a pseudo-random number (or a vector of pseudo-random numbers) taken from the standard normal distribution (having mean zero and standard deviation 1). For each bias error Zb having 95% uncertainty $\pm$DeltaZb, a single random number Zb $= 1/2 *$ DeltaZb $*$ randn(randstr, 1) was generated, and for each precision error Zp having 95% uncertainty $\pm$Delta Zp, a vector of random numbers Zp $= 1/2 *$ DeltaZp $*$ randn(Nt, 1) was generated where Nt is the number of points in the time series and randn(Nt, 1) generates a Nt $\times$ 1 vector of uncorrelated random numbers. For each error Zc having 95% uncertainty $\pm$DeltaZc that is correlated over time scale T,

we generate an autoregressive process of order one, having exponential autocorrelation function $\rho(\tau) = \exp(-|\tau|/\mathrm{T})$. An autoregressive process of order one has a Gaussian distribution and exponential autocorrelation function (Shumway and Stoffer, 2011). Defining $\mathrm{f} \equiv \exp(\Delta t/\mathrm{T})$ where Δt is the time between consecutive data points in the time series, we generate the error Zc as follows:

$$
\begin{aligned}
&\mathrm{Z0} = \mathrm{randn}(\mathrm{Nt}, 1);\\
&\mathrm{Zc}(1) = \mathrm{Z0}(1);\\
&\text{for j} = 1 \text{ to } (\mathrm{Nt} - 1)\\
&\quad \mathrm{Zc}(\mathrm{j}+1) = \mathrm{f} * \mathrm{Z0}(\mathrm{j}) + \mathrm{sqrt}(1 - \mathrm{f.\hat{}}\ 2)\mathrm{Z0}(\mathrm{j});\\
&\text{end}\\
&\mathrm{Zc} = 1/2 * \mathrm{DeltaZc} * \mathrm{Zc};
\end{aligned}
$$

The measured autocorrelation functions for flow rate in 2002 and 2003 are plotted in Figure D.1. It is clear that these autocorrelation functions are not exponential, but we fit exponential autocorrelation functions for the purpose of our error analysis because of the convenience of generating a pseudo-random time series having this type of autocorrelation function. The best fit exponential functions are plotted along with the measured autocorrelation in Figure D.1.

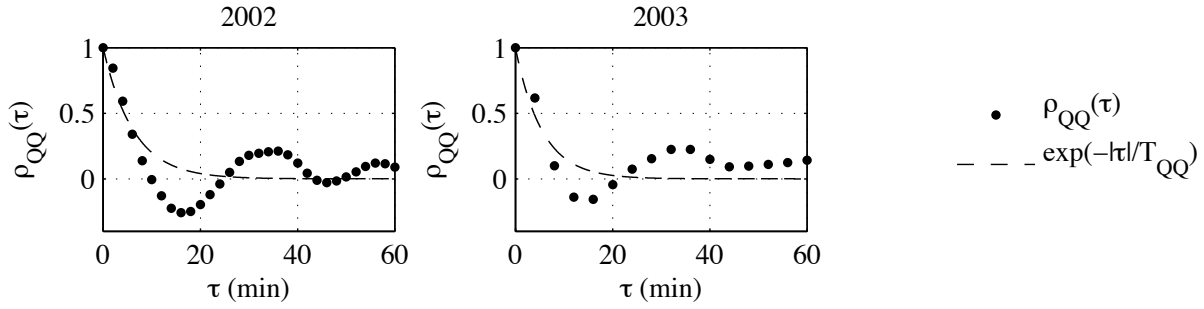

Figure D.1: Measured and best fit (in a least square sense) exponential autocorrelation functions for the outflow time series in 2002 and 2003. The fitted data includes points up to (but not beyond) the second zero crossing, resulting in best fit $T_{QQ} = 6.25$ min in 2002 and $T_{QQ} = 5.50$ min in 2003.

WORKS CITED

Andradóttir, H. O. and Nepf, H. M. (2000). Thermal mediation in a natural littoral wetland: measurements and modeling. *Limnol. Oceanogr.*, 36:2937–2946.

Bencala, K. E., Rathburn, R. E., Jackman, A. P., Kennedy, V. C., Zellweger, G. W., and Avanzino, R. J. (1983). Rhodamine wt dye losses in a mountain stream environment. *Water Resour. Bulletin*, 19:943–950.

Blumberg, A. F. and Mellor, G. L. (1987). A description of a three-dimensional coastal ocean circulation model. In Heaps, N., editor, *Three-dimensional coastal ocean models*. American Geophysical Union.

Bohm, M., Finnigan, J. J., and Raupach, M. R. (2000). Dispersive fluxes and canopy flows: Just how important are they? In *American Meteorological Society, 24th Conference on Agricultural and Forest Meteorology, 14-18 August 2000, University of California, Davis, CA*, pages 106–107.

Buchanan, T. and Somers, W. (1969). *Discharge measurements at gaging stations: U.S. Geological Survey techniques of water-resources investigations, Book 3*. United States Geological Survey.

Burchard, H. and Peterson, O. (1999). Models of turbulence in the marine environment – a comparative study of two-equation turbulence models. *J. Marine Systems*, 21:29–53.

Coles, D. (1956). The law of the wake in the turbulent boundary layer. *J. Fluid Mech.*, 1:191–226.

Danckwertz, P. V. (1953). Continuous flow systems: distribution of residence times. *Chem. Eng. Sci.*, 2:1–13.

Dierberg, F. E. and DeBusk, T. A. (2005). An evaluation of two tracers in surface-flow wetlands: rhodamine WT and lithium. *Wetlands*, 25:8–25.

Dunn, C., López, F., and García, M. (1996). Mean flow and turbulence in a laboratory channel with simulated vegetation. *Hydraul. Eng. Ser.*, 51. *UILU-ENG-96-2009*, Dep. of Civ. Eng. Univ. of Ill. at Urbana-Champaign, Urbana, Ill.

Effler, S. W. (1985). Attenuation versus transparency. *J. Environ. Eng.*, 111:448–459.

Efron, B. R. and Tibshirani, R. (1993). *An Introduction to the Bootstrap*. Chapman & Hall.

Finnemore, E. J. and Franzini, J. B. (2002). *Fluid Mechanics with Engineering Applications*. McGraw-Hill Higher Education, 10th edition.

Finnigan, J. (2000). Turbulence in plant canopies. *Annu. Rev. Fluid Mech.*, 32:519–571.

Finnigan, J. J. (1985). Turbulent transport in flexible plant canopies. In Hutchison, B. A. and Hicks, B. B., editors, *The Forest-Atmosphere Interaction*, pages 443–480.

Folger, H. S. (1992). *Elements of chemical reaction engineering*. Prentice-Hall, 2nd edition.

Gates, D. M. (1980). *Biophysical Ecology*. Springer-Verlag.

Ghisalberti, M. and Nepf, H. M. (2004). The limited growth of vegetated shear layers. *Water Resour. Res.*, 40. doi:10.1029/2003WR002776.

Gill, A. E. (1982). *Atmosphere-Ocean Dynamics*. Academic.

Hamblin, P. (1982). On the free surface oscillations of Lake Ontario. *Limnol. Oceanogr.*, 27:1039–1049.

Hilton, A. B. C., McGillivary, D. L., and Adams, E. E. (1998). Residence time of freshwater in Boston's inner harbor. *J. Waterw. Port Coast. Ocean Engng*, 124:82–89.

Kadlec, R. H. (1994). Detention and mixing in free water wetlands. *Ecological Engineering*, 3:345–380.

Kasnavia, T., De Vu, and Sabatini, D. A. (1999). Fluorescent dye and media properties affecting sorption and tracer selection. *Ground Water*, 37:376–381.

Katul, G. G., Mahrt, L., Poggi, D., and Sanz, C. (2004). One- and two-equation models for canopy turbulence. *Boundary Layer Met.*, 113:81–109.

Keefe, S. H., Barber, L. B., Runkel, R. L., Ryan, J. N., McKnight, D. M., and Wass, R. D. (2004). Conservative and reactive solute transport in constructed wetlands. *Water Resour. Res.*, 40. doi:10.1029/2003WR002130.

King, A. T. (2006). Field measurements of bulk flow and transport through a small coastal embayment having variable distributions of aquatic vegetation. Master's thesis, Cornell University.

King, A. T., Rueda, F. J., Tinoco, R. O., and Cowen, E. A. (2009). Modeling flow and transport through aquatic vegetation in natural water bodies. In *Proceedings of the 33rd IAHR Congress*, Vancouver BC, Canada. August 9-14, 2009.

Kline, S. J. and McClintock, F. A. (1953). Describing uncertainties in single-sample experiments. *Mech. Engrg*, 1:3–8.

Launder, B. E. and Spalding, D. B. (1974). The numerical computation of turbulent flows. *Comput. Method. Appl. M.*, 3:269–289.

Levenspiel, O. (1999). *Chemical Reaction Engineering*. John Wiley & Sons, 3rd edition.

Lightbody, A. F. and Nepf, H. M. (2006). Prediction of velocity profiles and longitudinal dispersion in emergent salt march vegetation. *Limnol. Oceanogr.*, 51:218–228.

Lin, A. Y.-C., Debroux, J.-F., Cunningham, J. A., and Reinhard, M. (2003). Comparison of rhodamine wt and bromide in the determination of hydraulic characteristics of constructed wetlands. *Ecological Engineering*, 20:75–88.

Lin, P. and Liu, P. L.-F. (1998). Turbulence transport, vorticity dynamics, and solute mixing under plunging breaking waves in surf zone. *J. Geophys. Res.*, 103:15677–15694.

Lohrman, A., Hackett, B., and Rø ed, L. P. (1990). High resolution measurements of turbulence, velocity and stress using a pulse-to-pulse coherent sonar. *J. Atmos. Ocean. Technol.*, 7:19–37.

López, F. and García, M. H. (2001). Mean flow and turbulence structure of open-channel flow through non-emergent vegetation. *J. Hydraul. Engng*, 127:392–402.

Luhar, M., Rominger, J., and Nepf, H. (2008). Interaction between flow, transport and vegetation spatial structure. *Environ. Fluid Mech.*, 8:423–439.

Luketina, D. (1998). Simple tidal prism models revisited. *Estuarine, Coastal and Shelf Science*, 46:77–84.

Mellor, G. L. (1996). Users guide for a three-dimensional, primitive equation, numerical ocean model. *Ocean Model.*, 13:379–403.

Mobley, C. D. (1994). *Light and Water: Radiative Transfer in Natural Waters*. Academic Press.

Monsen, N. E., Cloern, J. E., Lucas, L. V., and Monismith, S. G. (2002). A comment on the use of flushing time, residence time, and age as transport time scales. *Limnol. Oceanogr.*, 47:1545–1553.

Poggi, D., Katul, G. G., and Albertson, J. D. (2004a). A note on the contribution of dispersive fluxes to momentum transfer within canopies. *Boundary Layer Met.*, 111:615–621.

Poggi, D., Porporato, A., Ridolfi, L., Albertson, J. D., and Katul, G. G. (2004b). The effect of vegetation density on canopy sub-layer turbulence. *Boundary Layer Met.*, 111:567–587.

Pope, S. B. (2000). *Turbulent Flows*. Cambridge University Press.

Raupach, M. R., Coppin, P. A., and Legg, B. J. (1986). Experiments on scalar dispersion within a model plant canopy: Part i: The turbulence structure. *Boundary Layer Met.*, 35:21–52.

Raupach, M. R. and Shaw, R. H. (1982). Averaging procedures for flow within vegetation canopies. *Boundary Layer Met.*, 22:79–90.

Rueda, F. J. and Cowen, E. A. (2005a). Exchange between a freshwater embayment and a large lake through a long, shallow channel. *Limnol. Oceanogr.*, 50:169–183.

Rueda, F. J. and Cowen, E. A. (2005b). Residence time of a freshwater embayment connected to a large lake. *Limnol. Oceanogr.*, 50:1638–1653.

Rueda, F. J. and Schladow, S. G. (2002). Quantitative comparison of models for the barotropic response of homogeneous basins. *J. Hydraul. Engng*, 128:201–213.

Sabatini, D. A. and Austin, T. A. (1991). Characteristics of rhodamine WT and fluorescein as adsorbing ground-water tracers. *Ground Water*, 29(3):341–349.

Sandford, L. P., Boicourt, W. C., and Rivers, S. R. (1992). Model for estimating tidal flushing of small embayments. *J. Waterw. Port Coast. Ocean Engng*, 118(6):635–655.

Shaw, R. H. and Seginer, I. (1985). The dissipation of turbulence in plant canopies. In *Proceedings of the 7th Symposium of the American Meteorological Society on Turbulence and Diffusion*, pages 200–203. Am. Meteorol. Soc.

Shiau, B.-J., Sabatini, D. A., and Harwell, J. H. (1993). Influence of rhodamine WT properties on sorption and transport in subsurface media. *Ground Water*, 31(6):913–920.

Shumway, R. H. and Stoffer, D. S. (2011). *Time Series Analysis and its Applications: With R Examples*. Springer. doi: 10.1007/978-1-4419-7865-3.

Smart, C. and Karunaratne, K. (2002). Characterisation of fluorescence background in dye tracing. *Environmental Geology*, 42:492–498.

Smart, P. L. and Laidlaw, I. M. S. (1977). An evaluation of some fluorescent dyes for water tracing. *Water Resour. Res.*, 13:15–33.

Smith, P. E. (2006). A semi-implicit, three-dimensional model of estuarine circulation. Technical Report Open file report 2006-1004, USGS, Sacramento, CA.

Soerens, T. S. and Sabatini, D. A. (1996). Interpretation of sorption studies for compound isomers or mixtures. *Ground Water*, 34(4):605–609.

Song, Y. and Haidvogel, D. (1994). A semi-implicit ocean circulation model using a generalized topography-following coordinate system. *J. Comput. Phys.*, 115:228–244.

Soulsby, R. L. and Dyer, K. R. (1981). The form of the near-bed velocity profile in a tidally accelerating flow. *J. Geophys. Res.*, 86:8067–8074.

Suijlen, J. M. and Buyse, J. J. (1994). Potentials of photolytic rhodamine WT as a large-scale water tracer assessed in a long-term experiment in the Loosdrecht lakes. *Limnol. Oceanogr.*, 39(6):1411–1423.

Sutton, D. J., Kabala, Z. J., Francisco, A., and Vasudevan, D. (2001). Limitations and potential of commercially available rhodamine WT as a groundwater tracer. *Water Resour. Res.*, 37(6):1641–1656.

Tai, D. Y. and Rathbun, R. E. (1988). Photolysis of Rhodamine WT. *Chemosphere*, 17:559–573.

Tanino, Y. and Nepf, H. M. (2008a). Laboratory investigation of mean drag in a random array of rigid, emergent cylinders. *J. Hydraul. Engng*, 134:34–41.

Tanino, Y. and Nepf, H. M. (2008b). Lateral dispersion in random cylinder arrays at high Reynolds number. *J. Fluid Mech.*, 600:339–371.

Tinoco, R. O. (2008). An experimental investigation of the turbulent flow structure in one-dimensional emergent macrophyte patches. Master's thesis, Cornell University.

Trudgill, S. T. (1987). Soil water dye tracing, with special reference to the use of rhodamine WT, lissamie FF and amino acid G. *Hydrological Processes*, 1:149–170.

Turner, E. G., Netherland, M. D., and Getsinger, K. D. (1991). Submersed plants and algae as factors in the loss of rhodamine WT dye. *J. Aquat. Plant Manage.*, 29:113–115.

Valentine, E. M. and Wood, I. R. (1977). Longitudinal dispersion with dead zones. *J. Hydraul. Div. Am. Soc. Civ. Eng.*, 103:975–990.

Vasudevan, D., Fimmen, R. L., and Francisco, A. B. (2001). Tracer-grade rhodamine WT: Structure of constituent isomers and their sorption behavior. *Environ. Sci. Tech.*, 35:4089–4096.

Warner, J. C., Sherwood, C. R., Arango, H. G., and Signell, R. P. (2005). Performance of four turbulence closure models implemented using a generic length scale method. *Ocean Model.*, 8:81–113.

Wells, M. G. and Sealock, L. (2009). Summer water circulation in Frenchman's Bay, a shallow coastal embayment connected to Lake Ontario. *J. of Great Lakes Research*, 35:548–559.

Werner, T. M. and Kadlec, R. H. (1996). Application of residence time distributions to stormwater treatment systems. *Ecological Engineering*, 7:213–234.

Wilson, J. D. (1988). A second-order closure model for flow through vegetation. *Boundary Layer Met.*, 42:371–392.

Wilson, N. R. and Shaw, R. H. (1977). A higher order closure model for canopy flow. *J. Appl. Meteorol.*, 16:1197–1205.

Wüest, A. and Lorke, A. (2003). Small-scale hydrodynamics in lakes. *Annu. Rev. Fluid Mech.*, 35:373–412.